
UNIVERSITY OF LIVERPOOL

# Compression of Full-field Data for Operational Modal Analysis based on Shape Descriptors and Compressed Sensing

Thesis submitted in accordance with the requirements of the University of Liverpool for the degree of Doctor in Philosophy

By

Yen-Hao Chang

December 2019

# Abstract

The extraction of useful information and removal of redundant noise from data has become a major research topic in recent years. Data compression is necessary for all kinds of analysis, and the demand for efficient compression techniques has gained much attention. Digital image correlation (DIC) is a camera-based, optical measuring system, which has been widely applied in strain analysis because of the convenience of measuring displacement fields by simply selecting a region of interest. Currently, there is interest in applying such methods to engineering structures in dynamics. However, one of the major issues related to the integration of camera-based systems with dynamic measurement is the generation of huge amounts of data, typically extending to many thousands of data points, because of the requirements of high sampling rate, spatial resolution, and long duration of recording. In this study, the problem of data compression of displacement maps from 3D-DIC measurement is addressed. As a non-contact optical full-field measurement technique, 3D-DIC displacement measurement is becoming more widely applied to various kinds of dynamic issues. The research presented in this thesis attempts to apply the algorithms of sparse representation to deal with the huge amount of data acquired from 3D-DIC measurement. It aims to develop methods that have the capability of preserving nuances of displacement measurement and retaining the compactness of shape descriptor (SD) decomposition. Accordingly, two useful compression methods based upon the well-known K-SVD algorithm and compressed sensing (CS) method are developed for the purpose of a succinct and representative decomposition of displacement maps from 3D-DIC measurement.

Firstly, a new algorithm is presented that addresses the need for efficiency in full-field

data processing. By making use of the data itself and combining the concept of SD representation with Gram-Schmidt orthonormalisation (GSO), the number of basis functions used to represent the data can be reduced and a concise decomposition established. In both simulated and experimental cases, the compression ratios for data size and number of signals used in operational modal analysis are substantially diminished, thereby demonstrating the effectiveness of the proposed algorithm. A reduced number of new basis functions is determined for the representation of data under the condition that the reconstructed displacement map reproduces the raw measured data to within a chosen threshold of correlation coefficient.

Secondly, the monitoring of an operating structure usually dealing with multiple set of data, which could pose an issue for transmission or storage and is particularly important when data acquisition is implemented with cameras, such as 3D-DIC system. Single images regularly extend to tens or even hundreds of thousands of data points and many thousands of images may be required for a single set of vibration tests. Such data must be handled efficiently for later remote reconstruction and analysis, typically OMA. It is this requirement that is addressed and solved by the integrated SD-CS method because CS alone is found to be prohibitively expensive for the processing of many thousands of camera images. Data reduction by a combination of SD decomposition and CS is applied to an industrial printed circuit board and reconstructed for OMA by $\ell_1$ optimisation. This procedure is demonstrated on industrial DIC data from a partially observed printed circuit board and further significant compression, which is beyond the reduction effect provided by SD method alone, is achieved and OMA is carried out successfully on CS-recovered data.

In summary, the basis-updating algorithm is a powerful tool for the adaptation of kernel functions to the data set collected by 3D-DIC displacement measurement system. The algorithm is capable of finding a representative set of shape descriptors for

displacement maps from an initial basis. On the other hand, the integration of CS theory and SD method offers a new way to extract the core information from the measured data. This post-processing technique not only improves the compression ratio but also provides the possibility of structural health monitoring.

Keywords: Digital Image Correlation, Shape Descriptor, Compressed Sensing, Operational Modal Analysis, Structural Health Monitoring

# 摘要

近年來，如何提取有效的資料以及移除冗餘的雜訊逐漸成為研究焦點。對於各種的工程分析而言，資料壓縮是不可或缺的，有效率的壓縮方式將對各種工程研究有助益。數位影像相依性(Digital Image Correlation)演算法系統是一種基於雙數位相機的立體視覺量測系統，該系統已經被廣泛的應用在力學的應變分析上，因為其可以直接量測選取區域之位移場的簡便性。目前，這項量測系統已經逐漸被應用於動態的工程量測上，但正是由於測量儀器是數位像相機而又產生了新的問題。其中最主要的問題就是資料量變成非常龐大，通常會有幾千個資料點的時序資料肇因於高取樣頻率、高空間解析度以及長取樣時間的要求。在本研究中，主要探討如何有效的壓縮立體視覺數位影像相依性系統所量取的位移場圖序列。作為一種非接觸的光學全域量測技術，立體視覺數位影像相依性系統的應用越來越廣泛。本論文中提出應用稀疏表示來處理由立體視覺數位影像相依性系統量測所產生的龐大資料。目標是發展能夠保留位移場圖中的細部資訊以及維持形狀描述子(Shape Descriptor)表示的簡潔性。此研究中提出了兩個有效的資料壓縮方法基於知名的 K-SVD 演算法以及壓縮感知(Compressed Sensing)技術來算出具有代表性又簡潔的資料表示。

首先，本研究提出一種新的演算法來有效的處理全域的資料，藉由資料本身的特性以及結合形狀描述子與格拉姆-施密特單範正交化(Gram-Schmidt Orthonormalisation)，使表示資料的基底函數數量減少，但仍可建立更簡潔的分解。在模擬與實際量測的案例中，資料大小與訊號數量的壓縮比都有明顯提升，顯示了本演算法的有效性。新基底函數的資料表示所重建的位移場圖，符合了指定的相依性係數的閾值條件。

另外，通常在工作結構的監測中，會量測很多組的資料，可能會造成資料傳輸以及儲存的問題，這個問題尤其明顯當量測儀器是數位相機時，也就是立體視覺數

位影像相依性系統。一張位移圖有數千個量測點，一組有意義的量測通常包含數千張位移場圖，而通常為了降低雜訊的影響，振動量測又會測量數組的數據，如此大量的資料必須要以有效率的方式處理，以方便之後的遠端重建與分析，尤其是操作模態分析(Operational Modal Analysis)。本研究正是因為此需求而提出結合形狀描述子與壓縮感知的資料壓縮方法，因為只使用壓縮感知技術並不能更有效的壓縮資料。本整合的方法被示範應用於部分可觀測的工業電路板之分析上，用操作模態分析藉由$\ell_1$最佳化壓縮與重建位移場圖。壓縮與重建的流程可於該例子中瞭解，而其壓縮效果更勝單獨使用形狀描述子方法，且從操作模態分析結果中，可以驗證壓縮感知重建的資料保留了原始資料的核心資訊。

總結，基底函數更新演算法是一個有效降低用於表示之基底函數數量的工具，並且其產生的基底函數更適合應用於壓縮立體視覺數位影像相依性系統量測的資料上，該演算法能夠由初始基底函數更新，進而找到一組有代表性的形狀基底函數去代表位移場圖。另一方面，整合壓縮感知與形狀描述子的方法提供了一種新的方式去提取量測資料中的核心資訊，這種後處理的技術不只提升了壓縮比，也提供了結構健康監測(Structural Health Monitoring)新的可行性。

關鍵字：數位影像相依性(Digital Image Correlation)、形狀描述子(Shape Descriptor)、壓縮感知(Compressed Sensing)、操作模態分析(Operational Modal Analysis)、結構健康監測(Structural Health Monitoring)

# Acknowledgement

First, I would like to express my sincere appreciation to my primary supervisors Prof. John Mottershead and Prof. Jen-Yuan Chang who offered me invaluable guidance, support and encouragement throughout my PhD duration, which has greatly inspired me to face the challenges in my research. Also, I would like to greatly thank my secondary supervisors Prof. Eann Patterson for his helpful advice and experimental support. I am very grateful for all their help. Without Dr. Weizhuo Wang's invaluable and helpful technical assistance and insightful suggestions, I could not carry out my PhD research smoothly. I gratefully acknowledge the opportunity provided by the dual PhD programme between University of Liverpool and National Tsing Hua University. It would not have been possible for me to have the international experience without the programme. Last, I would like to express the special thanks to my family for their support.

# Contents

# Nomenclature

| | |
|---|---|
| $c_{\mathrm{X0}},\ c_{\mathrm{Y0}}$ | The Components of Center Coordinate |
| $f_i$ | Natural Frequency |
| $f_X,\ f_Y$ | Focal Length in X- and Y- direction |
| $m_{pq}(\mu_{pq})$ | Geometric Moment (central) |
| $p_i(t)$ | Modal Force |
| $p(\cdot)$ | Posterior Probability Density Function |
| $\mathbf{p}$ | The Subset Coordinate |
| $\mathbf{q}(t)$ | Nodal Displacement Vector |
| $r_{ij}$ | The Component of Rotational Matrix |
| $s$ | Skew Factor |
| $t_i$ | The Component of Translational Matrix |
| $tr(\cdot)$ | The Trace of Matrix |
| $u_0,\ u_x,\ u_y,\ u_{xx},\ u_{yy},\ u_{xy}$ | X-direction Gradient Coefficients in Shape Function (2nd-order) |
| $\mathbf{u}(t)$ | Input Vector |
| $v_0,\ v_x,\ v_y,\ v_{xx},\ v_{yy},\ v_{xy}$ | Y-direction Gradient Coefficients in Shape Function (2nd-order) |
| $\mathbf{v}_k$ | Measurement Noise of Sensor Inaccuracy |
| $\mathbf{w}_k$ | Noise of Disturbances and Modelling Inaccuracies |
| $\mathbf{x}_{\mathrm{k}}$ | Discrete-time State Vector |
| $\mathbf{x}(t)$ | Continuous-time State Vector |
| $\hat{\ddot{\mathbf{x}}}_j$ | Acceleration Data |
| $\mathbf{y}_k$ | Discrete-time Output Vector |

| | |
|---|---|
| $\mathbf{y}(t)$ | Output State Vector. |
| $\mathbf{A}$ | Discrete-time System Matrix, |
| $\mathbf{A}_\mathbf{c}$ | Continuous-time System Matrix |
| $\mathbf{A}_r, \mathbf{B}_r$ | Matrices with Model Parameters from Right Matrix-Fraction Model |
| $\mathbf{B}_\mathbf{c}$ | Continuous-time Input Matrix |
| $\mathbf{C}$ | Discrete-time Output Matrix |
| $\mathbf{C}_\mathbf{c}$ | Continuous-time Output Matrix |
| $\mathbf{C}_k$ | Covariance Matrix |
| $\mathbb{C}$ | Set of All Complex Numbers |
| $D$ | Measured Data |
| $\mathbf{D}_\mathbf{c}$ | Continuous-time Direct Transmission Matrix |
| $E[\cdot]$ | Expectation |
| $\mathbf{E}_z$ | Representation Error Matrix |
| $F(\cdot)$ | The Grey Value of Reference Image |
| $\mathbf{F}$ | Input Force Matrix |
| $\boldsymbol{\mathcal{F}}_k$ | Fast Fourier Transform Coefficient |
| $G(\cdot)$ | The Grey Value of Image After Deformation |
| $\mathbf{G}$ | The Next State-Output Covariance Matrix |
| $\mathbf{H}$ | Viscous Damping Matrix |
| $\mathbf{K}$ | Stiffness Matrix |
| $L(\cdot)$ | Negative Log-likelihood Function |
| $M$ | The Modeling Assumptions |
| $MAC$ | Modal Assurance Criterion |
| $\mathbf{M}$ | Mass Matrix |
| $\mathbf{M}_\mathbf{I}$, $\mathbf{M}_\mathbf{E}$ | Intrinsic and Extrinsic Matrices |
| $\mathbf{N}$ | Basis Matrix |

| | |
|---|---|
| $\mathbf{O}$ | Observability Matrix |
| $R_n^m$ | Radial Polynomial |
| $\mathbb{R}$ | Set of All Real Numbers |
| $\mathbf{R}_j$ | The Output Covariance Matrix |
| $Re(\cdot)$ | The Real Part of Complex Number |
| $S$ | Spectral Density |
| $\mathbf{S}$ | Coefficient Matrix |
| $S_e$ | The Spectral Density of Prediction Error |
| $\mathbf{S}_i$ | Basis Function |
| $\mathbf{S}_{yy}^{+}$ | Half-spectrum Matrix |
| $\hat{\mathbf{S}}_{yy}(\omega_j)$ | The Output Spectrum Matrix |
| $SD_i$ | Shape Descriptor |
| $T_{pq}$ | 2D Tchebichef Polynomial |
| $\mathbf{T}_{1\|\mathrm{i}}$ | Toeplitz Matrix |
| $\mathrm{TV}(\cdot)$ | Total Variation |
| $\mathbf{X}$ | Representation Matrix |
| $\mathbf{Y}_{0\|2i-1}$ | Hankel Matrix |
| $\mathbf{Y}_b(\omega_j)$ | Discrete Fourier Transform of Signal Block |
| $\mathbf{Y}_{im}$ | Image Matrix |
| $\mathbf{Y}_{imb}$ | Image Block Matrix |
| $\mathbf{Y}_k$ | Complement Matrix |
| $Z_n^m$ | Zernike Polynomial |
| $\varepsilon$ | The Least-square Cost Function |
| $\boldsymbol{\varepsilon}_\mathrm{j}$ | Predition Error |
| $\eta_i(t)$ | Modal Response |
| $\theta$ | Set of Parameters |

| | |
|---|---|
| $\boldsymbol{\kappa}$ | Sparcifying Coefficient |
| $\widehat{\boldsymbol{\kappa}}$ | Estimated Sparcifying Coefficient |
| $\lambda_k$ | The Eigenvalues of Continuous-time State-space Model |
| $\mu_k$ | The Eigenvalues of Discrete State-space Model |
| $\mu(\cdot)$ | Coherence |
| $\boldsymbol{\xi}_k$ | Eigenvector of $\mathbf{A}$ |
| $\rho$ | The Correlation Coefficient |
| $\sigma^2$ | Spectral Density of Prediction Error |
| $\zeta_k$ | Damping Ratio |
| $\boldsymbol{\phi}_k$ | Mode Shape Vector |
| $\boldsymbol{\psi}_j$ | Sparcifying Basis Function |
| $\tau_i$ | Hu's Seven Moment Invariants |
| $\omega_k$ | Natural Frequency in Radius |
| $\Gamma$ | Sum of Square Differences of a Continuous Domain |
| $\Gamma_{\text{discrete}}$ | Sum of Square Differences of a Continuous Domain |
| $\boldsymbol{\Gamma}$ | Controllability Matrix. |
| $\boldsymbol{\Lambda}$ | Original Image |
| $\widehat{\boldsymbol{\Lambda}}$ | Reconstructed Image |
| $\boldsymbol{\Xi}$ | Measurement Basis |
| $\boldsymbol{\Pi}$ | Basis of Centroids |
| $\boldsymbol{\Phi}$ | Mode Shape Matrix |
| $\boldsymbol{\Psi}$ | Sparcifying Basis |
| $\Delta t$ | Sampling Time. |
| $\boldsymbol{\mathcal{H}}$ | Basis |
| $\mathrm{ך}_{\mathrm{i}}$ | Tchebichef Polynomial |

# Acronyms

| | |
|---|---|
| AGMD | Adaptive Geometric Moment Descriptor |
| BSS | Blind Source Separation |
| CCD | Charge-Coupled Device |
| CPU | Central Processing Unit |
| CS | Compressed Sensing |
| CT | Computed Tomography |
| DFT | Discrete Fourier Transform |
| DIC | Digital Image Correlation |
| DoF | Degrees of Freedom |
| DVC | Digital Volume Correlation |
| EoM | Equation of Motion |
| FDD | Frequency-Domain Decomposition |
| FE | Finite Element |
| FFT | Fast Fourier Transform |
| FRF | Frequency Response Function |
| GSO | Gram-Schmidt Orthonormalisation |
| K-SVD | K-Singular Value Decomposition |
| MAC | Modal Assurance Criterion |
| MPV | Most Probable Value |
| MRI | Magnetic Resonance Imaging |
| NLLF | Negative Log-Likelihood Function |
| OMA | Operational Modal Analysis |
| PDF | Probability Density Function |

| | |
|---|---|
| P-LSCF | Poly-reference Least Square Complex Frequency-domain method |
| PP | Peak Picking |
| RAM | Random Access Memory |
| RD-ITD | Random Decrement Ibrahim Time-Domain method |
| RoI | Region of Interest |
| SCA | Sparse Component Analysis |
| SCPs | Single Source Points |
| SD | Shape Descriptor |
| SHM | Structural Health Monitoring |
| SSD | Sum of Square Differences |
| SSI | Stochastic Subspace Identification |
| SSI-COV | COVariance-driven Stochastic Subspace Identification |
| SSI-Data | Data-driven Stochastic Subspace Identification |
| SVD | Singular Value Decomposition |
| TV | Total Variation |

# List of Figures

# List of Tables

# 1 Introduction

## 1.1 Problem overview

The detection of damage at the earliest possible time in an operating structure gives the decision-maker an advantage in selecting the best solution for the prevention of further hazard or maintenance cost. As one of the examples regarding cost of millions of dollars, the semiconductor manufacturing industry is adopting structural health monitoring (SHM) to help minimise the need for redundant machinery necessary to prevent inadvertent downtime in their fabrication plants. Airlines along with government agencies are investigating SHM technologies for identification of damage to the aircrafts by aerodynamic phenomena for the safety of crews and passengers. Also, many buildings and infrastructure are exceeding their initial design life, any seismic events might bring about huge loss to the citizens and put their lives in danger. In the past few decades, there is an increasing need for the technology to achieve the identification of such damage, and therefore a user-friendly vision-based operational modal analysis, which provides full-field information, serves as an alternative to existing methods for damage detection.

## 1.2 Objective of the study

The objective of the study is to develop a method that can serve as an alternative method to traditional modal analysis or be used for structural health monitoring under the condition that only output responses are available. To achieve this final goal, there are several aspects that should be considered, and they are the following three elements: the measurement system, efficient data processing and the analysis. Firstly, for the

measurement system, the promising DIC system is chosen because of its convenience when compared to other traditional point-based systems in terms of the displacement field. The DIC system as well as the estimation algorithm for displacements are briefly introduced in Chapter 3. Secondly, to effectively process the huge amount of data generated from camera-based DIC systems, the data compression method is of great necessity, and this part is the major contribution of the thesis. Two developed compression methods based on SD and CS techniques are presented as the solution for the effective processing of data in Chapters 6 and 7. Lastly, about the analysis method, only the existing OMA methods that do not require additional fitting procedure are adopted for the identification of modal properties as introduced in Chapter 4. Each key component of the thesis is further introduced in the following sections, and for a more detailed outline of the thesis, please refer to section 1.7.

### 1.3 DIC method

Recently, there have been increasing interests in testing tools that can provide global information about the dynamics of structures. This information is used for understanding fundamental dynamic behaviors of structures as well as validating and updating analytical models. The numerical simulation approaches such as the finite element (FE) method can provide full-field results over an entire structure. Notwithstanding, the traditional point-based measurement techniques, such as accelerometers or strain gages, can only provide measurements at a few discrete locations. Thereby, there is a mismatch between the few measurement degrees of freedoms for the empirical data compared to the potential millions of degrees of freedom in the FE model that complicates the meaningful and effective correlation. In addition, the conventional sensors and wiring needed for data transmission or power supply may cause mass-loading effects. Therefore, there has been a significant need for

a non-contact measurement approach that has full-field sensing capability while avoiding adding mass or stiffness to the structure or changing the dynamic behaviour through mounting of sensor.

In recent years, the application of digital cameras in engineering has widely increased thanks to the improvement of integrated circuits. One of such examples is the measurement of surface deformation of structures, which could be as small as a micrometer in both in-plane and out-of-plane directions. Nevertheless, there are also disadvantages in the utilisation of camera-generated data, possibly the most important of which is its large volume. In order to visualise subtle deformation from a video, both the sampling frequency and image resolution should be raised, and this results in a huge amount of data. Not only is the processing of data time-consuming, but the requirement of acquisition hardware is demanding. The predominant algorithm used for the calculation of full-field displacement is called digital image correlation (DIC), which matches image patches and computes the displacement maps from a series of frames. The displacement maps are then used for further analysis of the strain field. In order to deal with large amounts of data generated from the measurement, an efficient data processing method for the post-processing, transmission and storage is desired.

### 1.4 Operational modal analysis (OMA)

One of the most important means to understand mechanical properties of engineering structures is achieved through modal analysis, by which modal parameters, such as natural frequencies, mode shapes, and damping ratios can be identified. Traditionally, the excitation of a structure under test is generated by artificial forces, such as impact by an instrumented hammer or sinusoidal or random excitation using shakers. With the carefully tuned input, structural properties can be conveniently calculated from the frequency response function (FRF), which is derived from both the

input and output spectra. Nonetheless, meaningful modal analysis results are only available when all necessary conditions are satisfied, i.e. the signal to noise ratio must be large enough so that useful information are preserved, which means the tested structure is mainly excited by the specified forces and sensors are well isolated from environmental disturbance, and the real boundary condition should be the same as designated by testing scheme. Under some circumstances, these conditions might not be matched, for example, an offshore oil-platform in the sea, where the influence from wind and wave is much stronger than that from artificial source in general, and it is not possible to know what is the real boundary condition of such a gigantic structure. Hence, a more practical idea of merely utilising output response from the environmental excitation comes into existence, which is referred by the terminology operational modal analysis (OMA). The assumption of OMA is that ambient force, which is deemed as input, has white-noise behavior, i.e. the spectral density is approximately constant across the testing frequency range. Fortunately, most of natural excitations exist in the environment have such characteristic.

### 1.5 Full-field shape-descriptor method

The extraction of useful information and removal of redundant noise from data has become a major research topic in recent years. Data compression is necessary for all kinds of analysis, and the demand for efficient compression techniques has gained much attention. As mentioned before, digital image correlation is a camera-based measuring system, which has been widely applied in strain analysis because of the convenience of measuring displacement fields by simply selecting a region of interest. Currently, there is interest in applying such methods to engineering structures in dynamics. However, one of the major issues related to the integration of camera-based systems with dynamic measurement is the generation of huge amounts of data, typically extending to many

thousands of data points, because of the requirements of high sampling rate, spatial resolution, and long duration of recording. A demand for efficient data compression comes into mind, and there are two methods discussed and applied in this research. The first one is shape descriptor, and the second one is compressed sensing.

The shape descriptor technique was originally developed in computer science discipline for pattern recognition. It is based on the fact that normal patterns have spatial redundancy, which means there are certain preferential 'shapes' or 'features'. By extracting these main features and giving them corresponding weightings, a pattern could easily be decomposed or reconstructed. Notwithstanding, there is no general idea what a feature is, i.e. a pattern could have multiple representations. In the past, numerous shape descriptors have been proposed and they are applied in different situations.

### 1.6 Compressed sensing

Conventional approaches to sampling signals or images follow Nyquist-Shannon's theorem: the sampling rate must be uniformly at least twice the maximum frequency present in the signal. In fact, this principle underlies the signal acquisition protocols used in consumer audio and visual electronics, medical imaging devices, radio receivers, and so on. Thanks to the development of compressed sensing technique, the requirement of uniform sampling rate could be overturned, and signal can be reconstructed from only part of the samples instead of all of them. This provides a great advantage in data processing, transmission and storage.

### 1.7 Outline of the thesis

In the scope of applying the SD method to the displacement maps measured with

DIC system for OMA, two promising methods were carried out, they are, (1) a basis-updating algorithm for SD-based OMA is proposed and the compression ratio and reconstruction result are superior to previous pre-determined SD methods; (2) a compression technique based upon compressed sensing is used for a more compact representation of the existing SD data set reducing the cost for data transmission and storage.

**Chapter 2:** This chapter gives a comprehensive literature review of the related topics including DIC, OMA, SD and CS. The latest references of application are also introduced in the review.

**Chapter 3:** The 2D and 3D DIC systems are introduced at the beginning of the chapter as well as the geometric optics behind 3D-DIC system. Later, a brief comparison of local and global DIC algorithms is presented and the details of local DIC algorithm used in the commercial software is explained at the end of chapter.

**Chapter 4:** The chapter starts with the introduction of well-known linear equation of motion, and the continuous-time deterministic state-space model and discrete-time stochastic state-space model are included in the discussion for the OMA methods explained afterwards. There are in total four OMA methods explained in detail in this chapter; one of them is a time-domain method and the others are frequency-domain methods. The time-domain method is called stochastic subspace identification (SSI), and the frequency-domain method includes frequency-domain decomposition (FDD), poly-reference least square complex frequency-domain method (P-LSCF) and the Bayesian method.

**Chapter 5:** The most important mathematical SD theory is explained in full details in this chapter. The explanation starts with image decomposition and reconstruction and the earliest proposed descriptor, geometric moment descriptor. Later on, the Tchebichef, Zernike and the latest adaptive geometric moment descriptors are explained with both

mathematical theory and examples.

**Chapter 6:** The proposed basis-updating algorithm is explained in this chapter as well as the background of the study. The inspiration of the method is acquired from basis learning in computer science, where image blocks are represented by the sparse linear combination of kernels from a pre-determined or adaptive basis. One of the most prominent algorithms is K-SVD, which is developed based upon famous clustering method, K-means. The steps of the basis-updating algorithm as well as the analysis procedure for processing of data from DIC measurement are illustrated. Both numerical and experimental case studies are provided in the chapter for the validation of the proposed method.

**Chapter 7:** Compressed sensing theory is explained at the beginning of the chapter together with the $\boldsymbol{\ell_1}$ norm and TV minimisation. The experimental case study used in the previous chapter serves as the example for the demonstration of the proposed SD-CS method, and the procedure as well as discussion and result are given at the end of the chapter.

**Chapter 8:** A review of key components of the research and main conclusions of this thesis are presented. The important contributions of this study are highlighted with suggestions for the future research which could be further developed to extend current the investigations.

### 1.8 Contribution by the author

This thesis addresses the efficiency of data compression of displacement maps from the measurement of 3D-DIC system, which is crucial for the application of DIC in dynamic measurements and remains unsolved. The principal contribution of this thesis is introducing the SD and CS methods to 3D-DIC-acquired data for OMA. A new algorithm for the updating of basis functions is developed to accurately represent the

full-field displacement maps from DIC. Moreover, a second compression technique based upon the compressed sensing method for both SD signals and kernels is also proposed to further reduce cost for data transmission and storage.

The author has summarised the above research findings into one conference and two journal papers. Paper C1 offers the first attempt of integration of SD representation method and OMA. Paper J1 proposes a basis-updating algorithm for SD-based method to achieve a more succinct and representative decomposition, and paper J2 serves as an extension of J1 provides an integration of CS and SD methods for a compact compression of full-field displacement data from DIC measurement.

C1: Y.-H. Chang, W. Wang, E.A. Patterson, J.-Y. Chang, J.E. Mottershead. "Output-only full-field modal testing," X International Conference on Structural Dynamics. EURODYN. Procedia Engineering 199, pp. 423-428, 2017.

J1: Y.-H. Chang, W. Wang, T. Siebert, J.-Y. Chang, J. E. Mottershead. "Basis-updating for data compression of displacement maps from dynamic DIC measurements," Mechanical Systems and Signal Processing 115, pp. 405–417, 2019.

J2: Y.-H. Chang, W. Wang, J.-Y. Chang, J. E. Mottershead. "Compressed sensing for OMA using full-field vibration images," Mechanical Systems and Signal Processing 129, pp. 394-406, 2019.

# 2 Literature Review

In recent years the demand for online monitoring and remote inspection has brought about a huge surge of research activity in structural health monitoring (SHM). Applications range from the preservation of historical buildings [1] to the monitoring and maintenance of offshore wind turbines [2] with the purpose of minimising the costs of restoration, deterioration, machine down-time etc. Wireless sensor networks are increasingly prevalent. Hierarchical decentralized SHM as presented by Hackmann et al. [3] was said to be capable of only activating sensors in damaged regions and keeping others idle. Other than conventional accelerometer or strain gauge measurement, non-destructive acoustic [4] and non-contact vision-based [5, 6] measuring methods are also being adopted. Yang et al. [7] proposed a high-fidelity simulation and visualisation method for full-field dynamic structural responses based on phase-based motion magnification (Wadhwa et al. [8]) as an alternative to finite element analysis. Along with the expanding application of video-based monitoring, image transmission or storage plays an important role in realising the implementation of state-of-art techniques in industry. Yang and Nagarajaiah [9] suggested that images gathered from measurement can be first compressed for transmission and afterwards recovered by using the compressed sensing (CS) technique developed by Donoho [10]. As explained in [9], the main factor in industrial adoption of SHM research is the efficient and reliable transfer and processing of data. A discussion on closing the gap between academic research and industrial deployment was presented by Cawley [11] and a review of signal processing, as applied to SHM, was provided by Amezquita-Sanchez and Adeli [12]. From the demand of SHM, it is obvious that vision-based systems have become more widely applied and the size of data gathered from measurement has greatly

increased in the last decade. In this chapter, a literature review of the most relevant research topics is provided, which includes DIC, OMA, SD and CS. They correspond to measurement system and algorithm, identification method and compression methods, etc.

## 2.1 Digital image correlation (DIC)

Early development of DIC originated from the experimental stress analysis done by Peters and Ranson [13] using the concept of subset matching. The DIC algorithm was improved by Sutton et al. [14], Peters et al. [15] and Bruck et al. [16]. Two of the most detailed research texts on DIC are provided by Sutton et al. [17] and Sharpe et al. [18]. The DIC algorithm is presently the most widely applied computer vision method for strain analysis, and its application in dynamic measurement is becoming regular with promising new techniques breaking or circumventing the limitations related to stereo vision, high sampling rate and restricted line-of-sight. In a review of 3D high-speed DIC for vibration measurement, Beberniss and Ehrhardt [19] pointed to a difficulty at high frequency because of low out-of-plane sensitivity. Under a broadband white-noise excitation, high-frequency modes have relative low amplitudes compared to low-frequency modes, and the measurement of corresponding displacement images by DIC then becomes quite challenging. This was overcome separately by Poozesh et al. [20] and Molina-Viedma et al. [21] using phase-based motion magnification and results are reported in [22] for 3D operational deflection shapes in the range from 1500 Hz to 6710 Hz without the need for high levels of excitation. One of the disadvantages of applying DIC systems is that the accuracy of displacement estimates is limited by the surface curvature of the specimen - most demonstrations are carried out on plate-like structures. However, Poozesh et al.[23] and Patil et al. [24] developed methods for the stitching of DIC images of sub-areas of very large structures to obtain complete

images of vibration modes, which based on common reference points for the merging of mode shapes of sub-areas of large or curved structures, such as on motor-vehicle tyres or large turbine blades, to acquire the full mode shape of the test article. Javh et al. [25] developed an efficient gradient-based optical flow method and reported displacement resolutions of less than a thousandth of a pixel. They demonstrated the application of their method on the vibration modes of a cymbal up to 2373 Hz. Yu and Pan [26] presented a colour stereo-digital image correlation method using just one 3CCD colour camera without trade-off of spatial resolution and inaccessibility by the arrangement of mirrors and colour filters for the separation of light beams into its individual colour components. Yu and Pan [27] considered the combination of a four-mirror adapter with a single high-speed camera and validated the proposed system by comparison with finite element analysis. Later, the concepts introduced in [26] and [27] were integrated, i.e. single high-speed camera with mirror adapter and colour filters [28], and two experiments (shape measurement of a curved surface and vibration measurement of a Chinese double-side drum) were carried out for validation purposes. Instead of two industrial cameras, Chi et al. [29] used a consumer-grade Single Lens Reflex camera with a four-mirror adapter for the acquisition of images, and the low-cost and portable system was demonstrated on thermal deformation measurement of an alumina ceramic plate and a stainless-steel plate subjected to radiation heating. A comprehensive review of the development, methodologies, strengths and weaknesses of different single-camera DIC techniques for full-field 3D shape and deformation measurement is presented by Zhang et al. [30]. The numerous applications include the displacement measurement of the blade of a toy helicopter using DIC by Sousa et al. [31], model updating of hypersonic aircraft panels by Perez et al. [32] and low-velocity impact on composite plates by Flores et al. [33]. A comparison of local and global approaches to DIC is provided by Hild and Roux [34] with a result suggesting that a

global approach might out-perform a local one. Kriging regression is also applied to DIC by Wang et al. [35] for the estimation of displacement maps and further used in uncertainty quantification of DIC result by Wang et al. [36]. The quality of the speckle pattern affects the accuracy of displacement estimation, therefore Don and Pan [37] organised a review of typical fabrication and assessment procedures for DIC measurements. Due to the limitation of DIC measurement, which only measures surface displacement, digital volume correlation (DVC) has been proposed as a further extension of static strain analysis based on similar correlation algorithm for the inspection of interior deformation of an object with the assistance of transmissive measurement equipment. DVC system involves the algorithm for volumetric pixel matching and the equipment for the measurement of internal structures, such as X-ray tomography or magnetic resonance imaging (MRI) systems. For the measurement of the whole volume of specimen, usually some shifting of the platform, such as rotation or translation, is necessary, and this very demand greatly increases the duration of measurement. As a result of the long acquisition time of volumetric images, DVC system is currently limited to static measurement and not suitable for dynamic analysis requiring high sampling rate. Owing to the lack of efficient and accurate algorithms that can be implemented in personal computers with limited RAM, Pan and Wang [38] proposed a flexible and accurate DVC method that is applicable to high-resolution volumetric images. Another issue of DVC is using a fixed reference volume image generally fails when serious decorrelation occurs in deformed volume images due to large deformation, therefore a new incremental DVC approach was developed by Wang and Pan [39] as a solution. DVC measurement relies on the X-ray scanner to acquire digital images of sections, but the measurement itself may incur unavoidable slight and continual geometrical changes due to self-heating effects. Pan [40] suggests some solutions to address and quantify the issue of thermal error. A comprehensive review of

progress and challenges of DVC in the last two decades is organised by Buljac et al. [41]. After review of the references related to the measurement system, the papers related to analysis method are provided in the next section.

## 2.2 Operational modal analysis (OMA)

Due to the generally high physical dimensions and comparatively low frequency range of civil structures, the identification of modal properties by conventional modal analysis techniques is a relatively troublesome task. The excitation of such structures cannot be easily implemented and usually demands specially designed costly devices for the generation of programmable and measurable artificial forces. In response to this problem, researchers in civil engineering have turned to OMA. Relative to the traditional input-output techniques, OMA makes good use of the obtainable ambient excitations as input and determines modal properties (natural frequencies, mode shapes, modal damping etc.) from measured responses with the assumption that the excitation has constant spectral density in the form of white noise, which is often approximately true for natural excitations. Hence, OMA has become an established procedure for modal testing in civil engineering. For mechanical engineers, OMA can also serve as an alternative method for modal identification. There are two classes of OMA methods, i.e. the frequency-domain and time-domain techniques.

### 2.2.1 Time-domain methods

Temporal signals are directly processed when using time-domain OMA methods, which may be separated into three main approaches as: stochastic subspace identification (SSI) [42], random decrement Ibrahim time domain (RD-ITD) method [43-45], and blind source separation (BSS) [46].

RD-ITD and BSS are not included in the present discussion, because of the requirement for an additional fitting procedure to identify the modal parameters. Peeters and De Roeck [42] described the first step of the SSI method as the construction of a Hankel matrix composed of measured data. The main difference between covariance-based (SSI-COV) and data-driven (SSI-Data) is in how the data is processed, i.e. the covariance or projection matrix between 'future' and 'past' parts of the Hankel matrix. Both methods apply singular value decomposition (SVD) on the covariance or projection matrix to establish a matrix of observability, from which the system matrix may be determined using conventional control theory.

By altering the dimensions of the observability matrix, the dimensions of the system matrix changes, and a stabilisation diagram can be formed by plotting all the poles for the system matrices of different dimensions. From the stabilisation diagram and with the help of clustering techniques, such as hierarchical clustering as described in [47], stable poles, which corresponds to modes, may be selected. The visualisation of mode shapes in the spatial domain may be obtained by the linear combination of kernel functions and corresponding SDs.

### 2.2.2 Frequency-domain methods

Frequency-domain methods make use of the matrix of output auto- and cross-spectral densities. There are four main types of frequency-domain method: frequency domain decomposition (FDD) [48, 49] the transmissibility function method [50, 51], poly-reference least-squares complex frequency domain (P-LSCF) method [52], and Bayesian modal identification [53-55].

In this section, the details of three different frequency-domain methods are briefly explained, and they are FDD, Bayesian, and P-LSCF methods. The Bayesian approach

is based upon the first singular value spectrum calculated from FDD, which is included for that reason, even though additional single-DoF curve fitting is necessary.

Before the application of frequency-domain methods, an extra discrete Fourier transform (DFT) step is necessary. A 3D matrix of frequency spectra is formed, where each 2D submatrix contains auto- and cross- spectra at a specific frequency and the third dimension corresponds to the discrete frequency points of the DFT. By applying SVD on each 2D submatrix, the envelope of the sum of all first singular value spectra is formed. From this spectrum, the potential modes of the system may be selected by peak-picking (PP).

The identification of modes by the Bayesian method starts with the choice of peaks and frequency ranges of the singular value spectrum. Optimisation is based upon the gradient descent, and the modal parameters are identified by minimising the negative log of an objective function. Other than the selection of initial conditions, a convergence condition is also selected by the user.

In the P-LSCF method, the determination of modes is similar to SSI, which relies on the stabilisation diagram and clustering. However, the main difference is the computation of system poles, which depend upon the system matrices formed by a right matrix fraction. User-chosen parameters are the length of each time segment and the time lag between segments. The longer the time segment and time lag, the more the frequency lines and fewer the segments, and vice versa.

Applications of OMA methods are described by numerous authors, including Oliveira et al. [56] who reported on the continuous monitoring of an onshore wind turbine using the SSI-COV and P-LSCF methods, and Chen at al. [57] who used the SSI-Data and FDD techniques in the OMA of a multi-span concrete bridge. The ESA Vega launcher was investigated using OMA by De Vivo et al [58], and Chomette and Carrou [59] studied the modes of a concert harp. Very recent developments include

uncertainty quantification applied to the SSI-COV approach by Reynders et al. [60], and development of the Bayesian approach to account for asynchronous measurements from multiple set-ups by Zhu et al. [61-63]. A combination of DIC method and OMA was presented in [64]. The first investigation and application of integrated SD and OMA methods on simulated data was provided by Chang et al. [65]. Analysis was carried out in the SD domain, with mode shapes finally converted to the physical (spatial) domain.

### 2.3 Shape descriptors (SD)

One of the difficulties of using data from photogrammetry is its comparison with finite element (FE) predictions, since DIC grids are generally different from FE meshes. Leclerc et al. [66] directly compared the measured displacement field with simulated numerical results and implemented model updating by minimizing the difference between them. Other than the direct comparison, Wang et al. [67-71] and Patki and Patterson [72] developed image processing and pattern recognition techniques capable of extracting important features from displacement fields through predetermined kernel functions, such as geometric polynomials [73], Zernike [74], Tchebichef [75], or Krawtchouk [76] polynomials or wavelets [77]. With the use of such basis functions (or kernels), large amount of full-field data may be represented by just a few shape descriptor (SD) terms (also called moments) with high-fidelity. Each type of kernel functions is suitable for a particular geometric domain. For example, the Zernike polynomials are widely applied on domains with circular geometry, and Tchebichef polynomials on rectangular domains. On top of all previous development, Wang et al. [78] proposed a technique known as the adaptive geometric moment descriptor (AGMD) to deal with the issue of selecting kernels for different domains with three-dimensional irregular geometry and holes. They carried out modal tests on a car bonnet liner entirely in the SD domain and reconstructed the first eleven mode shapes in the physical domain

from the SD contributions. In DIC measurement, the complexity of measured domain of real engineering case is much higher, i.e. there might be irregularity or discontinuity in the displacement map. For the application of SD technique, it is firstly necessary to carry out an isomorphic mapping from the 3D surface to a 2D plane. In [77], this was achieved bijectively by using discrete conformal mapping as described by Desbrun et al. in [79]. This process involves meshing of the surface so that the difference in angle of individual triangular-element vertices on the curved surface and flat plane is minimized as explained by Pinkall and Polthier [80].

Some interesting applications are also reported, including the investigation of delaminations in composite materials and high-speed impact. Wang et al. [81] applied Kriging predictor with particle swarm optimisation to the Krawtchouk moment descriptors extracted from a strain map to inversely identify the unknown delamination parameters, including location and shape. A composite bonnet liner subject to a high-velocity impact by projectile was investigated using high-speed digital image correlation, and the results were compared to those predicted by finite element analysis with the reduction of dimensionality of datasets by using AGMD, which gives a significant advance in procedures for ensuring model fidelity and for creating model credibility in the simulation of dynamic engineering events by Burguete et al. [82].

### 2.4 Compressed sensing (CS)

Although the world seems to be full of diversity, redundancy is ubiquitous in nature, for example sound waves and electromagnetic waves can be represented by only a few frequency components corresponding to particular tones or colours, and the shape or pattern of astronomical objects, creatures, or even bacteria and viruses are of specific geometries, meaning that they are relatively sparse compared to the diversity of possibility that might be artificially created were science sufficiently advanced. Candès

et al. [83] and then Donoho [10] proposed to take advantage of this property of sparsity to recover a signal from a number of samples that was small when compared to the dimension of the original signal. The concept is widely applied today in several disciplines, and numerous examples can be seen in recent publications. Magnetic resonance imaging (MRI) has particularly benefitted from the application of CS [84] resulting in significantly improved scan times [85, 86] and the removal of artifacts and reconstruction errors [87]. Arridge et al. [88] applied CS to photoacoustic tomography imaging of living tissue and showed similar improvements in acquisition speed with good spatial resolution and contrast. Gangopadhyay et al. [89] highlighted the efficacy of CS for ultra-low power wireless and wearable biosensors, and Craven et al. [90] identified a reduction in healthcare costs in ambulatory monitoring of bioelectric signals. CS has been applied in such diverse fields as Solar Flare X-Ray Observation [91] and super resolution imaging in atomic force microscopy [92]. Real-time visualization of tissue by Fiber-bundle based endomicroscopy has two major limitations, namely the limited number of individual fibers in the bundle and blank in inter-fiber regions or gaps in the image, both of which are improved with the application of CS by Dumas et al. [93]. Acoustic imaging can also be improved by CS technique as demonstrated by Ning et al. [94] within low-noise environments. One of the most popular image compression methods is JPEG whereas Yuan et al. [95] proposed an improved scheme based on CS. Potter et al. [96] surveyed the use of CS reconstruction algorithms and randomized measurement strategies in radar processing with potential future directions. In the field of engineering dynamics, and with CS sensors still at the prototype stage, Yang and Nagarajaiah [97] explored the potential of combining output-only blind source separation (BSS) and CS. Qin et al. [98] developed a sparse component analysis (SCA) for the detection of single source points (SSPs) with sparsity in the time-frequency domain for OMA. Park et al. [99] considered the application of CS to modal

testing in the presence of close modes. They showed that the free vibration displacement response could be decomposed in terms of its singular values (SVD) where the left singular vectors are understood to be estimates of the system mode shapes. Uniform- and random-time sampling were considered, as was random matrix selection (Gaussian) from uniform samples. The latter was applied to a physical bridge structure with reconstruction using $\ell 1$ optimisation.

Rani et al. [100] provide a systematic review to bridge the gap between theory and practicality of CS, including different CS acquisition strategies and reconstruction approaches, major application areas and some of the challenges and research directions in the field of CS. A relatively clear and straightforward introduction for the explanation of CS theory is presented by Candes and Wakin [101].

## 2.5 Closure

From the literature review, it is obvious that there are a few knowledge gaps that require further research. First, due to the lack of common knowledge, the availability of full-field data from DIC system for OMA is not addressed in the references. Secondly, efficient storage and portability of full-field dynamic data has not been studied thoroughly. Therefore, a novel approach for the processing of full-field dynamics data acquired from DIC system using SD and CS techniques for OMA is proposed in the thesis and the published papers by the author. In the next chapter, the basic theory and procedures of DIC are addressed.

# 3 Digital Image Correlation

The idea of measuring displacement maps by camera was first proposed by Peters and Ranson [13]. It relies on the matching of patterns on the surface of the test structure. Such patterns typically take the form of spray-painted speckles and, when illuminated, the tracking of patterns on camera images enables structural displacements to be determined. Furthermore, Sutton et al. [14] developed a correlation algorithm with mathematical interpolation which was demonstrated through a bending experiment. A cantilever beam was first covered with black paint and then sprayed with white dots to form a random speckle pattern for image correlation. An analogue camera was used for image acquisition at that time and therefore the image had to be digitized. Peters et al. [15] applied the newly developed correlation method to rigid body motion, two experiments are included in the case study, one is the rotation of a disk and the other is the vibratory motion of a rod. The result demonstrated that the digital image method can be used in the analysis of two-dimensional rigid body motion. Later, the Newton-Raphson Method was used for a more effective calculation of image correlation by Bruck et al. [16]. In the research, both translational and rotational motion were studied, and the CPU-time was reduced by the application of this method. With the development and popularisation of digital cameras, the method has been widely applied to solve different engineering problems, such as warpage characterization [102], fatigue analysis [103], and 3D vibration analysis [104].

### 3.1 2D and 3D DIC system

The 2D DIC measurement system is composed of a camera and lighting, and the specimen must be sprayed with speckle pattern for image registration. The

displacement maps between two consecutive time frames are computed by comparing the coordinates of feature points. The surface of the specimen must be placed perpendicular to the camera view for elimination of the effect of out-of-plane displacement on the measurement. A typical experimental setting of strain analysis using 2D DIC is shown in Figure 3-1.

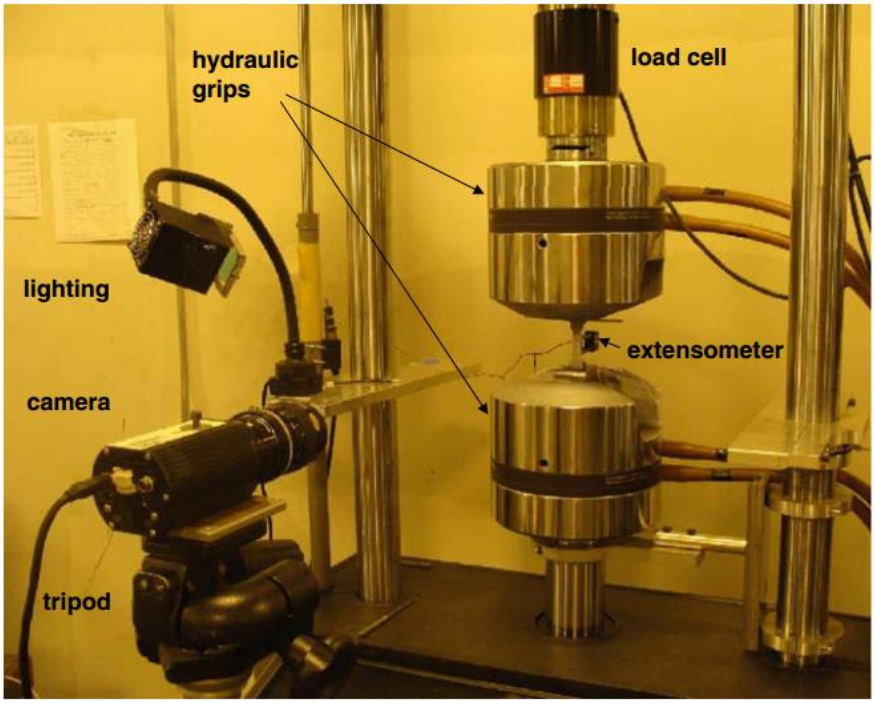


Figure 3-1. The picture of a typical 2D DIC system [9].

Although 2D DIC systems can be utilised to implement displacement measurement, the accuracy is relatively low when there is misalignment between the specimen and the camera. Therefore, for a more accurate measurement, the 3D DIC system was developed, the system is comprised of 2 cameras and lighting as demonstrated in Figure 3-2. There is no necessity to maintain the perpendicularity between the surface of specimen and cameras' views, because a stereo camera system can measure both out-of-plane and in-plane displacements.

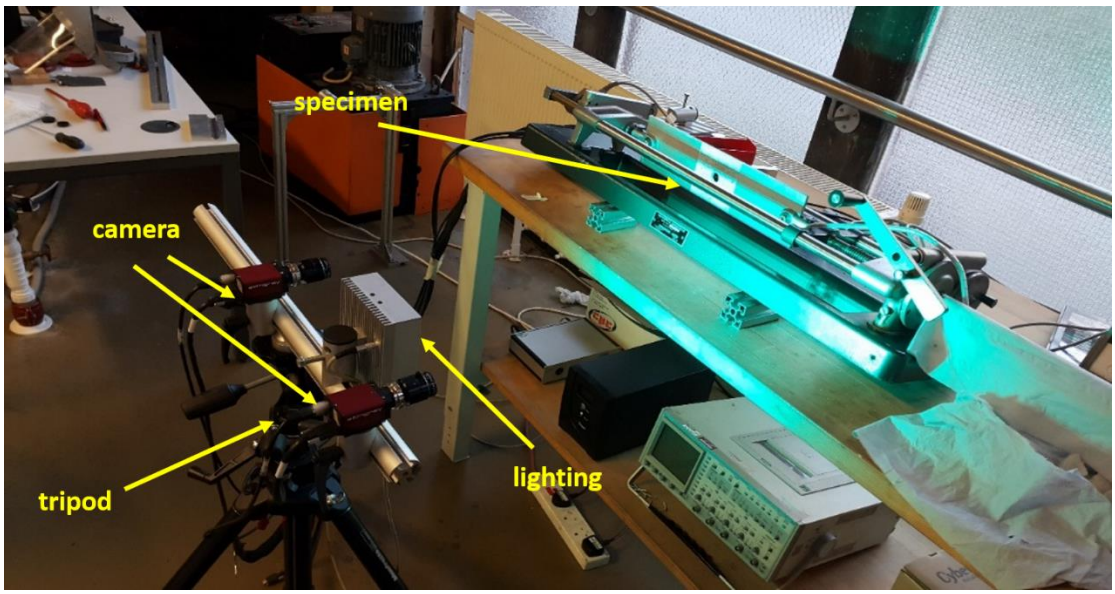


Figure 3-2. The picture of a typical 3D DIC system.

### 3.2 The geometric optics behind 3D DIC system

In this section, the theory of stereo vision is briefly introduced and explained. The explanation starts with the optics of a single camera. In Figure 3-3, a random point in world coordinates is first converted into camera coordinates, and then projected onto the pixel coordinates of the image. In mathematics, a rigid transformation is a geometric transformation of a Euclidean space that preserves the Euclidean distance between every pair of points. The rigid transformations include rotations, translations, reflections, or their combination. On the other hand, projective transformation is defined by mapping of a 3D spatial point onto a 2D surface (i.e. the image plane). The parameters connecting world and camera coordinates are called extrinsic parameters, and those related to the camera and pixel coordinates are named intrinsic parameters. The mathematical relation of coordinate transformation can be clearly seen in Equation 3-1.

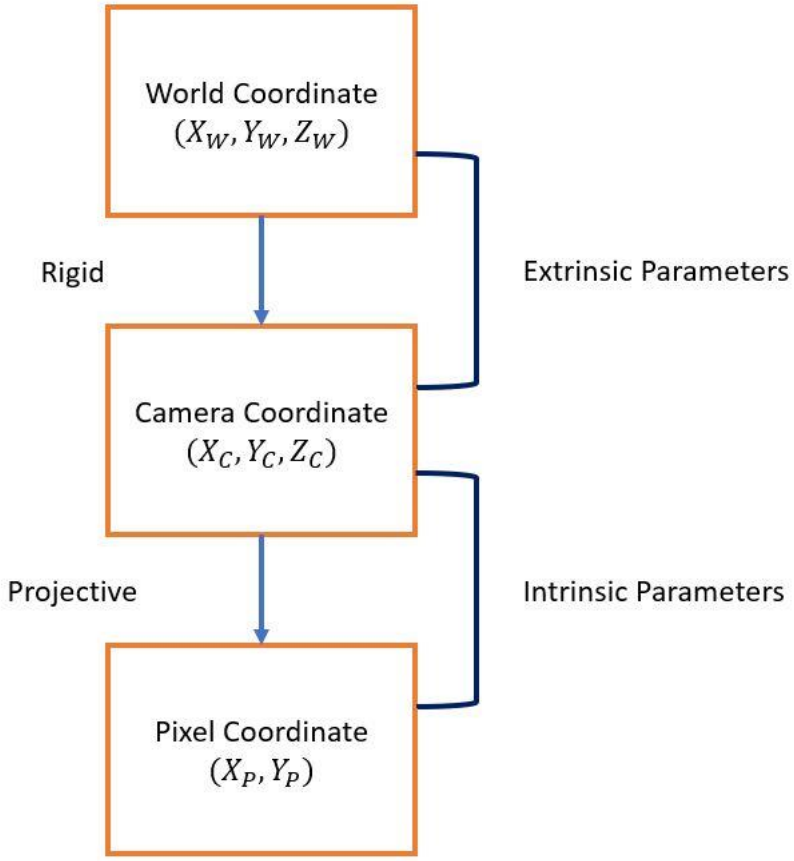


Figure 3-3. The illustration of relation among world, camera and pixel coordinates. The subscripts W, C, and P represent the world, camera and pixel coordinate. X, Y, Z are the coordinate components.

$$\begin{bmatrix} X_P \\ Y_P \\ 1 \end{bmatrix} = \mathbf{M_I M_E} \begin{bmatrix} X_W \\ Y_W \\ Z_W \\ 1 \end{bmatrix} = \begin{bmatrix} f_X & s & c_{\mathrm{X0}} \\ 0 & f_Y & c_{\mathrm{Y0}} \\ 0 & 0 & 1 \end{bmatrix} \begin{bmatrix} r_{11} & r_{12} & r_{13} & t_1 \\ r_{21} & r_{22} & r_{23} & t_2 \\ r_{31} & r_{32} & r_{33} & t_3 \end{bmatrix} \begin{bmatrix} X_W \\ Y_W \\ Z_W \\ 1 \end{bmatrix} \tag{3-1}$$

where $\mathbf{M_I}$, $\mathbf{M_E}$ are the intrinsic and extrinsic matrices, and $f_X$, $f_Y$ are the focal length, $c_{\mathrm{X0}}$, $c_{\mathrm{Y0}}$ are the components of center coordinate, $s$ is the skew factor, $r_{ij}$ is the component of rotational matrix, $t_i$ is the component of translational matrix.

As for a stereo system shown in Figure 3-4, there are two camera coordinate systems, and therefore two sets of intrinsic and extrinsic parameters to be solved. With the help of calibration board as shown in Figure 3-5, both intrinsic and extrinsic parameters can be identified, because the dimension of the specially made calibration board is pre-determined. However, multiple images of the calibration board at different positions must be taken in order to have enough equations to solve all the parameters inside both intrinsic and extrinsic matrices. Once all the unknown parameters are found, the relative coordinates of feature points on the surface of specimen can be computed. Hence, the next step is to match the feature points found in both left and right images. This is achieved by the DIC algorithm explained in section 3.4.

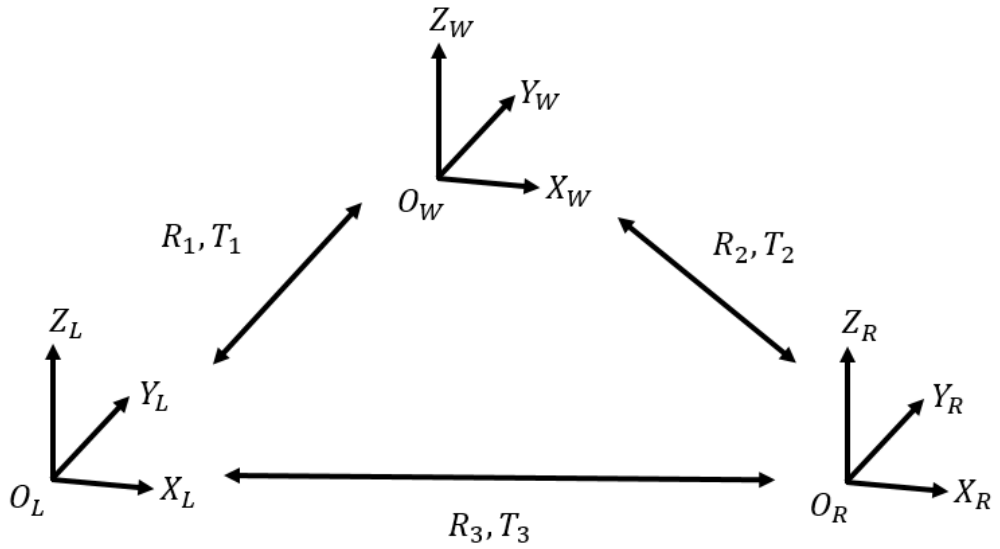


Figure 3-4. The illustration of relations among camera and world coordinates. The subscripts L, R, and W represent the left camera, right camera, and world coordinate. X, Y, Z, and O denote the three axes and origin. R and T are the rotation and translation matrices.

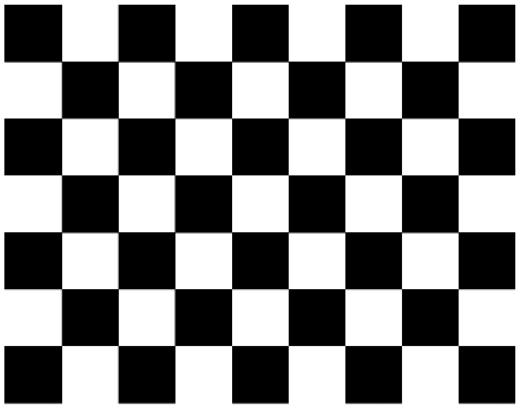

Figure 3-5. A typical pattern of calibration board.

### 3.3 Local and global DIC algorithms

How correlation is formed between images is the key difference behind local and global DIC algorithms. For local DIC algorithm, a selected region of interest (RoI) is first divided into rectangular subsets of relatively small dimension, and then the matching between different subsets of different images is calculated individually. A typical example of subset division can be observed in Figure 3-6.

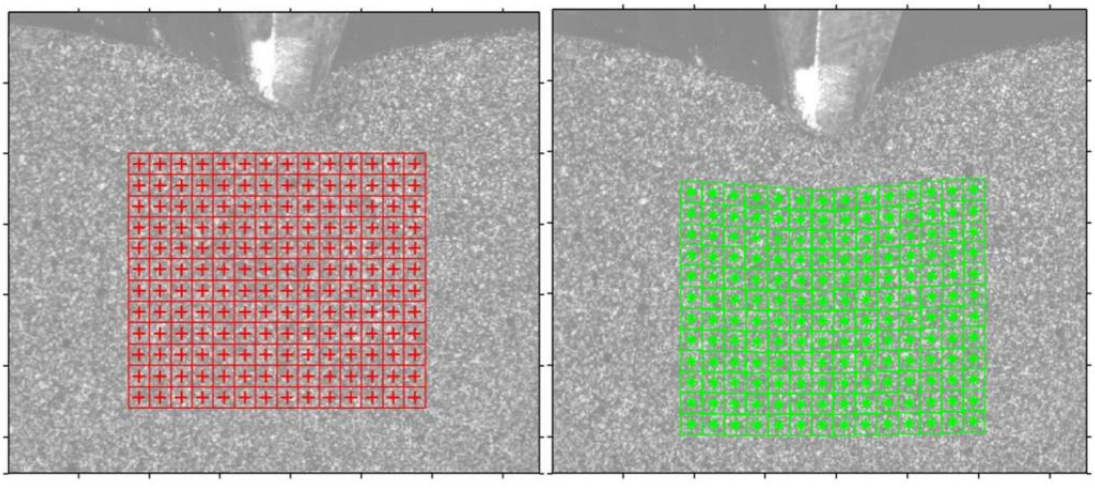

Figure 3-6. The illustration of subset-based DIC method (without overlapping subsets), the uniformly distributed square subsets (center nodes marked in '+') are initialised in the reference image (left) while the matched deformed subsets (center nodes marked in '*') are shown in the deformed image (right).

However, due to the lack of inter-subset continuity as well as the small number of degrees of freedom (DoF) in the subset displacement for the correlation, the local method is relatively sensitive to noise. On the other hand, a global algorithm establishes the correlation once without subdivision of region, which means all the parameters related to deformation and rigid body motion are computed at the same time. B-Splines proposed by Cheng et al. [105] or Finite Element shape functions proposed by Sun et al. [106] are examples of global DIC approach. The measurement uncertainty became smaller than those of subset-based DIC by considering more degrees of freedom. Nevertheless, when the spatial resolution is raised higher and more degrees of freedom are considered, it is computationally prohibitive for a global method. In the following section, only the local correlation algorithm is given a detailed explanation with mathematical formulas, because the commercial software embedded in the DIC system used by the data provider is based on the local correlation technique.

### 3.4 The local correlation algorithm

Displacement-field estimation by subset-based DIC is explained in this section, and the detailed illustration can be found in [17, 18]. Not only the correlation of different time frames, but also the correlation between the left and right images can be established by the algorithm. It is assumed that there is no lighting change between two frames, and the grey value, which represents the amount of light received by single sensor unit and ranges from black at the value of 0 to white at the value of 255, of the same location does not change. The image of the undeformed shape is first divided into several subsets, and the motion of specimen is estimated through the coordinate change of the subsets before and after displacement/deformation. Hence, the most important part of estimation is finding a subset having the minimum grey-value difference with respect to the reference image. The objective function of the minimisation is given by

Equation 3-2, which is known as a sum of square differences (SSD) over a domain $\Omega_{\text{sub}}$, a subregion of RoI.

$$\Gamma = \min \int_{\Omega_{\text{sub}}} \big(G(x^*, y^*) - F(x, y)\big)^2 \text{dxdy} \tag{3-2}$$

And may be cast in discrete form as,

$$\Gamma_{\text{discrete}} = \min \sum_{\Omega_{\text{sub}}} \big(G(x^*, y^*) - F(x, y)\big)^2 \tag{3-3}$$

, where $F(x, y)$ is the grey value of reference image at $(x, y)$, $G(x^*, y^*)$ is the gray value of image after deformation at $(x^*, y^*)$.

Minimisation of the objective function is generally carried out by using the Newton-Raphson algorithm, also known as gradient descent [16]. The subset coordinate at the n+1$^{\text{th}}$ iteration may be expressed as,

$$\mathbf{p}^{n+1} = \mathbf{p}^n + \Delta\mathbf{p} \tag{3-4}$$

and the increment is calculated by,

$$\Delta\mathbf{p} = -\mathbf{H}^{-1}(\mathbf{p}^n) * \boldsymbol{\nabla}(\mathbf{p}^n) \tag{3-5}$$

where $\boldsymbol{\nabla}$ is the gradient matrix, and $\mathbf{H}$ is the Hessian matrix.

The relation between the deformed and original coordinate may be represented by

$$\begin{aligned} x^* &= x + s(x, y) \\ y^* &= y + t(x, y) \end{aligned} \tag{3-6}$$

where $s(x, y)$ and t$(x, y)$ are coordinate transformation functions.

For a second-order shape function around the center node $(x_0, y_0)$ of a subset, the coordinate transformation function can be expressed as,

$$\begin{aligned} s(x,y) &= u_0 + u_x\Delta x + u_y\Delta y + \frac{1}{2}u_{xx}\Delta x^2 + \frac{1}{2}u_{yy}\Delta y^2 + u_{xy}\Delta x\Delta y \\ t(x,y) &= v_0 + v_x\Delta x + v_y\Delta y + \frac{1}{2}v_{xx}\Delta x^2 + \frac{1}{2}v_{yy}\Delta y^2 + v_{xy}\Delta x\Delta y \end{aligned} \quad (3\text{-}7)$$

where $\Delta x = x - x_0$, $\Delta y = y - x_0$, and $u_0$, $v_0$ are the x- and y-directional displacement components of the center node at $(x_0, y_0)$, $u_x$, $u_y$, $v_x$, $v_y$ are the components of the first-order displacement gradient, and $u_{xx}$, $u_{yy}$, $u_{xy}$, $v_{xx}$, $v_{yy}$, $v_{xy}$ are the components of the second-order displacement gradient.

### 3.5 Closure

The basic theory and setting behind 3D stereo camera system are introduced in this chapter, and the algorithm of local DIC method, which is adopted in the commercial DIC software is explained.

# 4 Operational Modal Analysis

Most modal identification methods are based on models of the tested dynamic system that are fitted to the recorded data and from which it is then possible to extract estimates of modal parameters. This chapter starts with the characterisation of the finite element model.

## 4.1 Linear equation of motion (EoM)

The analysis of a complex dynamic system requires its previous discretisation through the construction of a finite element model with a finite number of degrees of freedom. After this first step, the equilibrium of such system is represented by the following differential equation expressed in matrix form:

$$\mathbf{M}\frac{d^2\mathbf{q}(t)}{dt^2} + \mathbf{H}\frac{d\mathbf{q}(t)}{dt} + \mathbf{K}\mathbf{q} = \mathbf{F}\mathbf{u}(t) \tag{4-1}$$

where $\mathbf{M} \in \mathbb{R}^{n\times n}$ is the mass matrix, $\mathbf{H} \in \mathbb{R}^{n\times n}$ is the viscous damping matrix, $\mathbf{K} \in \mathbb{R}^{n\times n}$ is the stiffness matrix, $\mathbf{F} \in \mathbb{R}^{n\times n_i}$ is the input matrix, $\mathbf{q}(t) \in \mathbb{R}^{n\times 1}$ is the displacement vector of nodes, $\mathbf{u}(t) \in \mathbb{R}^{n_i\times 1}$ is the input vector, $n$ is the number of degrees of freedom (DoF), and $n_i$ is the number of inputs.

## 4.2 Continuous-time deterministic state-space model

Continuous-time means that the expressions can be evaluated at each time instant $t \in \mathbb{R}$ and deterministic means that the input-output quantities $\mathbf{u}(t), \mathbf{y}(t)$ can be measured exactly. The previous second-order system of differential equations can be transformed into a first-order one ($\mathbf{M}$ is invertible), the state-space equation

$$\dot{\mathbf{x}}(t) = \mathbf{A_c}\mathbf{x}(t) + \mathbf{B_c}\mathbf{u}(t)$$

$$\mathbf{y}(t) = \mathbf{C_c}\mathbf{x}(t) + \mathbf{D_c}\mathbf{u}(t) \qquad (4\text{-}2)$$

, where $\mathbf{x}(t) = \begin{bmatrix} \mathbf{q}(t) \\ \frac{d\mathbf{q}(t)}{dt} \end{bmatrix}$, $\mathbf{A_c} = \begin{bmatrix} \mathbf{0} & \mathbf{I} \\ -\mathbf{M}^{-1}\mathbf{K} & -\mathbf{M}^{-1}\mathbf{H} \end{bmatrix}$, $\mathbf{B_c} = \begin{bmatrix} \mathbf{0} \\ \mathbf{M}^{-1}\mathbf{F} \end{bmatrix}$, $\mathbf{C_c}$ is the output matrix related to the states measured, $\mathbf{D_c}$ is designated direct transmission matrix, $\mathbf{u}(t)$ is the input state vector, and $\mathbf{y}(t)$ is the output state vector.

### 4.3 Discrete-time stochastic state-space model

In reality, a system is neither continuous nor deterministic: measurements are only available at discrete-time instants $k\Delta t, k \in \mathbb{N}$ with $\Delta t$, the sample time and the only vibration information that is available are the responses of a structure excited by some unmeasurable inputs. Due to the lack of information it is not possible (from a system identification point of view) to distinguish between input and noise. The input is now implicitly modelled by the noise terms (output-only); therefore, the white noise assumptions of these terms cannot be omitted. The consequence of violation of assumption, for instance if the input contains some additional dominant frequency components, these frequency components cannot be separated from the eigenfrequencies of the system and they will appear as (spurious) poles of the state matrix $\mathbf{A}$. The stochastic state-space model is defined as following without the input term and includes the stochastic components (noise)

$$\mathbf{x}_{k+1} = \mathbf{A}\mathbf{x}_k + \mathbf{w}_k$$

$$\mathbf{y}_k = \mathbf{C}\mathbf{x}_k + \mathbf{v}_k \tag{4-3}$$

where $\mathbf{x}_\mathrm{k} = \mathbf{x}(k\Delta t)$ is the discrete-time state vector, $\mathbf{A} = \exp(\mathbf{A}_c\Delta t) \in \mathbb{R}^{n\times n}$ is the discrete-time state matrix, $\mathbf{C} \in \mathbb{R}^{n_o\times n}$ is the discrete-time output matrix, $\mathbf{w}_k \in \mathbb{R}^n$ is the process noise due to disturbances and modelling inaccuracies, and $\mathbf{v}_k \in \mathbb{R}^{n_o}$ is the measurement noise due to sensor inaccuracy. They are both unmeasurable vector signals, but we assume that they are zero mean and white.

The output covariance matrix with time lag $\tau = j\Delta t$ is defined as

$$\mathbf{R}_j \equiv E\left[\mathbf{y}_{k+\mathrm{j}}\mathbf{y}_k^T\right] \in \mathbb{R}^{n_o\times n_o} \tag{4-4}$$

where the next state-output covariance matrix $\mathbf{G}$ is defined as

$$\mathbf{G} \equiv E[\mathbf{x}_{k+1}\mathbf{y}_k^T] \in \mathbb{R}^{n\times n_o} \tag{4-5}$$

and $E$ is the expectation operator.

The symbols introduced in this section will be applied in the introduction of SSI-COV method.

### 4.4 OMA methods

The existing OMA methods can be categorised into time-domain and frequency-domain OMA. For the methods introduced in this chapter, no additional fitting procedure is required. The time-domain method applied in the study is called covariance-based stochastic subspace identification (SSI-COV) [42]. The frequency-domain methods are frequency-domain decomposition (FDD) method [49], poly-reference least-squares complex frequency-domain (P-LSCF) method [52] and

Bayesian method [53-55]. A comparison of different OMA methods including FDD, SSI-COV and P-LSCF with data from an arch bridge is provided by Magalhães and Cunha [107].

### 4.4.1 Time-domain method

The first step of SSI method is to form the Hankel matrix from recorded time-domain responses as

$$\mathbf{Y}_{0|2i-1} = \frac{1}{\sqrt{j}}\begin{bmatrix} \mathbf{y}_0 & \mathbf{y}_1 & \cdots & \mathbf{y}_{j-1} \\ \vdots & \vdots & \vdots & \vdots \\ \mathbf{y}_{i-2} & \mathbf{y}_{i-1} & \cdots & \mathbf{y}_{i+j-3} \\ \mathbf{y}_{i-1} & \mathbf{y}_i & \cdots & \mathbf{y}_{i+j-2} \\ \mathbf{y}_i & \mathbf{y}_{i+1} & \cdots & \mathbf{y}_{i+j-1} \\ \mathbf{y}_{i+1} & \mathbf{y}_{i+2} & \vdots & \mathbf{y}_{i+j} \\ \vdots & \vdots & \cdots & \vdots \\ \mathbf{y}_{2i-1} & \mathbf{y}_{2i} & \cdots & \mathbf{y}_{2i+j-2} \end{bmatrix} = \begin{bmatrix} \mathbf{Y}_{0|i-1} \\ \mathbf{Y}_{i|2i-1} \end{bmatrix} = \begin{bmatrix} \mathbf{Y}_p \\ \mathbf{Y}_f \end{bmatrix} = \begin{bmatrix} ("past")\updownarrow \\ ("future")\updownarrow \end{bmatrix} \in \mathbb{R}^{2n_o i \times j} \quad (4\text{-}6)$$

where the subscripts represent the time lag indices and the subscripts of $\mathbf{Y}_{0|i-1}$ are the subscript of the first and last element in the first column of the block Hankel matrix. The following equation is the Toeplitz matrix of covariance matrices constructed from the future and past data:

$$\mathbf{T}_{1|\mathrm{i}} \equiv \begin{pmatrix} \mathbf{R}_i & \mathbf{R}_{i-1} & \cdots & \mathbf{R}_1 \\ \mathbf{R}_{i+1} & \mathbf{R}_i & \cdots & \mathbf{R}_2 \\ \cdots & \cdots & \cdots & \cdots \\ \mathbf{R}_{2i-1} & \mathbf{R}_{2i-2} & \cdots & \mathbf{R}_i \end{pmatrix} = \mathbf{Y}_f \mathbf{Y}_p^T \in \mathbb{R}^{n_o i \times n_o i} \quad (4\text{-}7)$$

The Toeplitz matrix is composed of the controllability and observability matrices.

$$\mathbf{T}_{1|\mathrm{i}} = \begin{bmatrix} \mathbf{C} \\ \mathbf{CA} \\ \cdots \\ \mathbf{CA}^{j_b-1} \end{bmatrix} [\mathbf{A}^{j_b-1}\mathbf{G} \quad \cdots \quad \mathbf{AG} \quad \mathbf{G}] = \mathbf{O\Gamma} \quad (4\text{-}8)$$

where $\mathbf{O}$ is the observability matrix and $\mathbf{\Gamma}$ is the controllability matrix.

The observability and controllability matrices can be calculated by applying SVD to the Toeplitz matrix

$$\mathbf{T}_{1|\mathrm{i}} = \mathbf{U}\boldsymbol{\Sigma}\mathbf{V}^T = [\mathbf{U}_1 \quad \mathbf{U}_2]\begin{bmatrix}\boldsymbol{\Sigma}_1 & 0\\ 0 & 0\end{bmatrix}\begin{bmatrix}\mathbf{V}_1^T\\ \mathbf{V}_2^T\end{bmatrix} = \mathbf{U}_1\boldsymbol{\Sigma}\mathbf{V}_1^T \tag{4-9}$$

where $\mathbf{U}, \mathbf{V} \in \mathbb{R}^{n_o i \times n_o i}$ are orthonormal matrices and $\boldsymbol{\Sigma} \in \mathbb{R}^{n_o i \times n_o i}$ is a diagonal matrix containing the singular values in descending order.

The relations between the matrices acquired from the SVD and the matrices $\mathbf{O}, \boldsymbol{\Gamma}$ are listed below.

$$\begin{cases}\mathbf{O} = \mathbf{U}_1\boldsymbol{\Sigma}_1^{1/2}\\ \boldsymbol{\Gamma} = \boldsymbol{\Sigma}_1^{1/2}\mathbf{V}_1^T\end{cases} \tag{4-10}$$

The discrete-time state-space system matrices $\mathbf{A}$ and $\mathbf{C}$ can be estimated from the observability and controllability matrices.

In [108] the expressions that relate the discrete-time model matrices with their continuous-time counterparts are derived. There, it is also demonstrated that the eigenvectors of matrix $\mathbf{A}$ coincide with the ones of matrix $\mathbf{A}_c$. The eigenvalues of the discrete model, represented by $\mu_k$, are related with the ones of the continuous model $\lambda_k$ by the following equation:

$$\mu_k = \exp(\lambda_k \Delta t) \Leftrightarrow \lambda_k = \frac{\ln(\mu_k)}{\Delta t} \tag{4-11}$$

The system pole is related to natural frequency and damping ratio by the following

$$\lambda_k = -\zeta_k\omega_k + i\omega_k\sqrt{1-\zeta_k^2} \tag{4-12}$$

where $\zeta_k$ and $\omega_k$ represent damping ratio and natural frequency in radius respectively.

The corresponding mode shape $\boldsymbol{\phi}_k \in \mathbb{R}^{n_o}$ is the multiplication of output matrix $\mathbf{C}$

and eigenvector $\boldsymbol{\xi}_k \in \mathbb{R}^n$ of continuous-time system matrix $\mathbf{A}$

$$\boldsymbol{\phi}_k = \mathbf{C}\boldsymbol{\xi}_k \tag{4-13}$$

The modal assurance criterion of any two given mode shape $\boldsymbol{\phi}_1, \boldsymbol{\phi}_2$ is calculated as

$$MAC_{\boldsymbol{\phi}_1,\boldsymbol{\phi}_2} = \frac{\left(\boldsymbol{\phi}_1^T \boldsymbol{\phi}_2\right)^2}{(\boldsymbol{\phi}_1^T \boldsymbol{\phi}_1)(\boldsymbol{\phi}_2^T \boldsymbol{\phi}_2)} \tag{4-14}$$

which measures the correlation between two mode shapes, varies from 1, when the modes only differ on a scale factor, to zero, when the modes are orthogonal.

After the system matrix is estimated, the stable system modes can be identified by the most popular approach based on drawing a stabilisation diagram as Figure 4-1, which is also performed in P-LSCF method. The system order, whose range is determined by the user, is the number of singular values and vectors included for system modeling. However, the use of high model orders leads to the introduction of numerical modes (also called spurious or noise modes), which have little to none physical relevance but are needed to model the noise and to overcome the modelling inaccuracies. Separation of physical and spurious modes is then a crucial step of the identification algorithm. In Figure 4-2, the poles are clustered into groups of modes according to the similarity of parameters. Modes that appear in most of these models with consistent frequency, mode shape and damping ratio are classified as stable and are likely to be physical, and modes that only appear in some models are considered spurious and later removed as demonstrated in Figure 4-3.

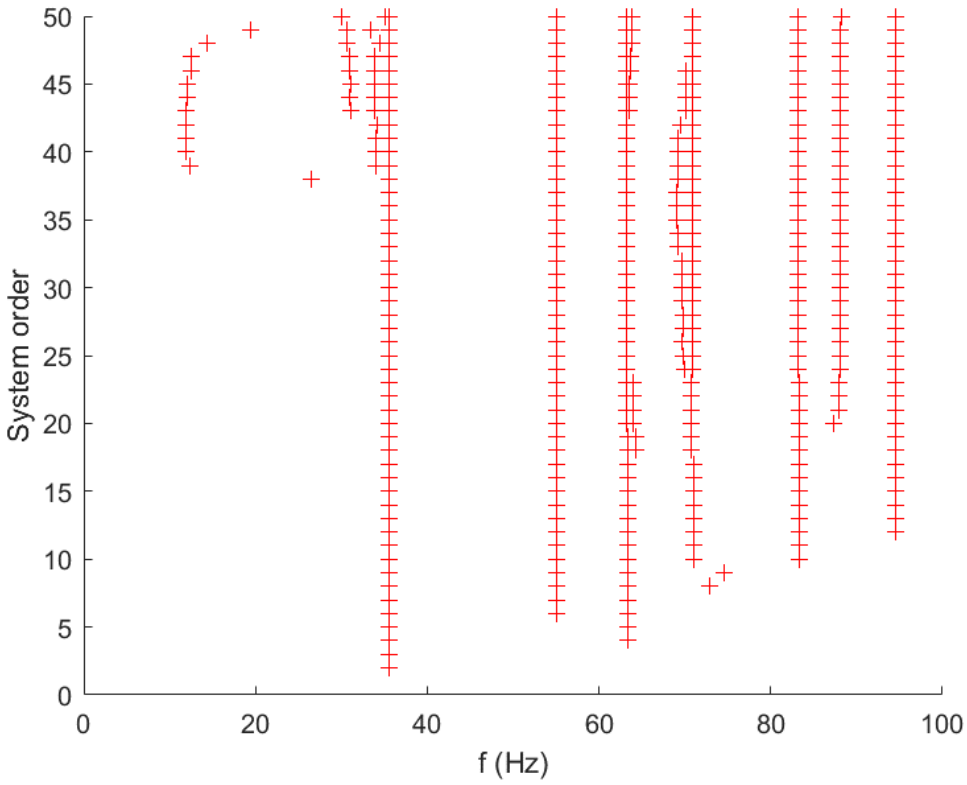


Figure 4-1. The stabilisation diagram estimated by SSI method.

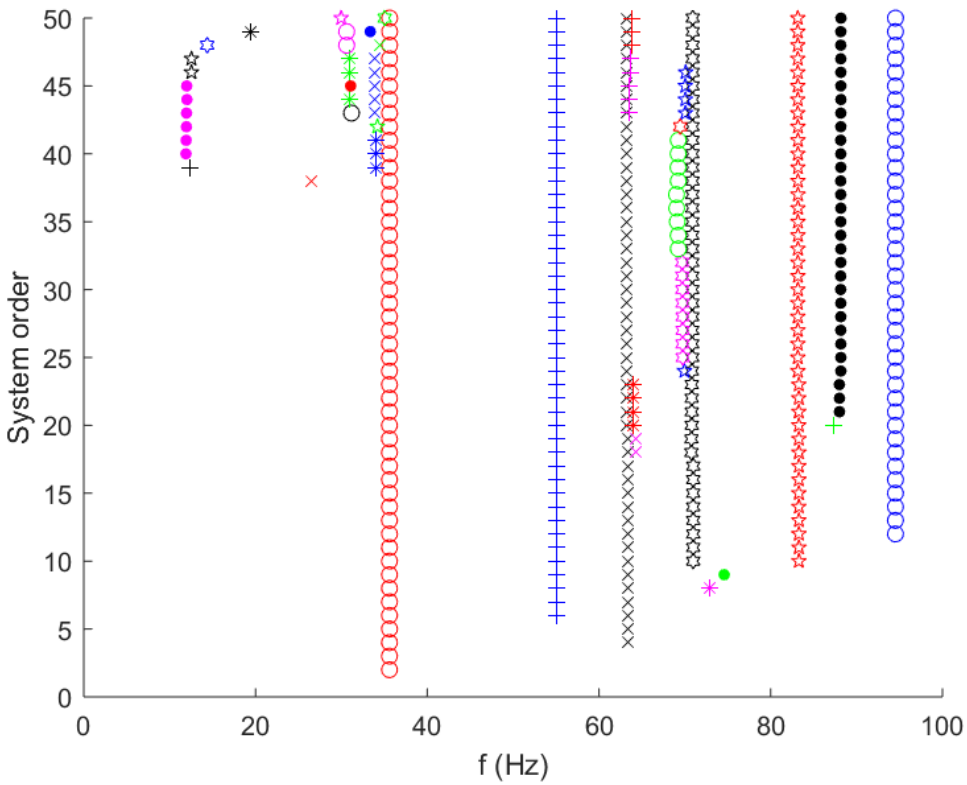


Figure 4-2. The clustering of poles from stabilisation diagram estimated by SSI method.

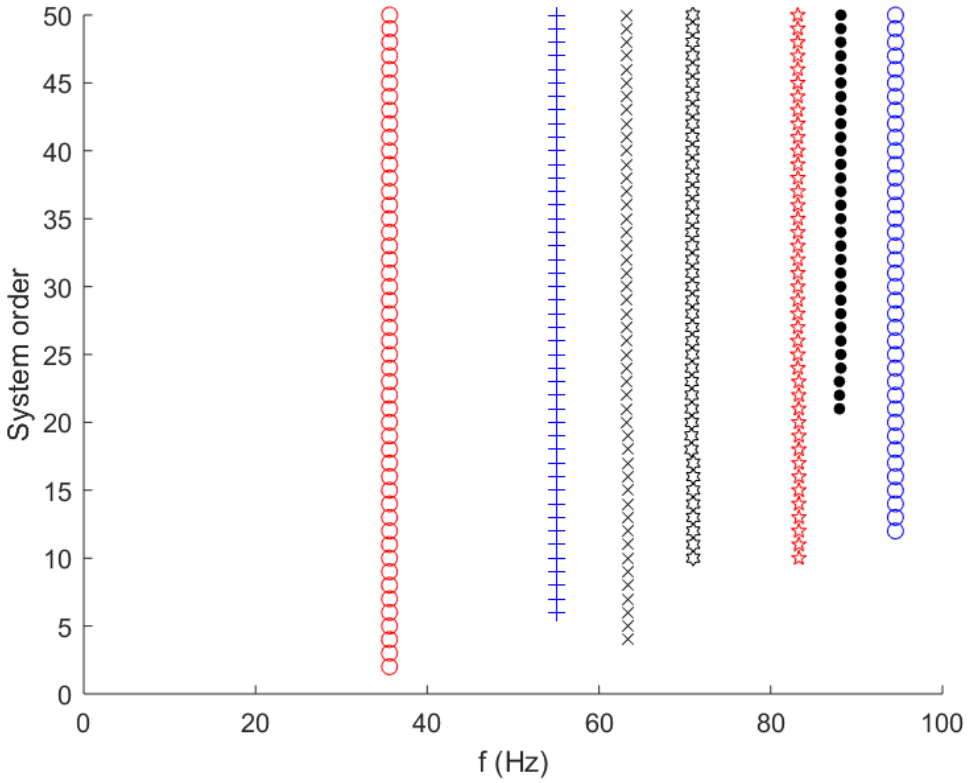


Figure 4-3. The stable modes extracted from stabilisation diagram estimated by SSI method.

### 4.4.2 Frequency-domain method

#### 4.4.2.A **Frequency-domain decomposition (FDD) method**

The calculation of spectra by Welch's method involves two steps: First, the recorded response is divided into $n_b$ segments $\mathbf{y}_b$ with the same length $n_{tb}$, which may present some percentage of overlap. The second step is the calculation of the discrete Fourier transform (DFT) of each block with the application of a window function $m_k$.

$$\mathbf{Y}_b(\omega_j) = \sum_{b=1}^{n_{tb}-1} m_k \mathbf{y}_{b,k} e^{-i\omega_j k\Delta t} \in \mathbb{C}^{n_o \times 1} \quad (4\text{-}15)$$

The output spectrum matrix at frequency $\omega_j$ is

$$\hat{\mathbf{S}}_{yy}(\omega_j) = \frac{1}{n_b}\sum_{b=1}^{n_b} \mathbf{Y_b}(\omega_j)\mathbf{Y_b}(\omega_j)^H \in \mathbb{C}^{n_o \times n_o} \tag{4-16}$$

where the auto-spectra and cross spectra of output states are the diagonal and off-diagonal elements respectively.

By applying SVD on each 2D spectral matrix at each DFT frequency, the singular value spectra can be formed. The possible modes are contained in the singular value spectrum formed by all the largest singular values at each DFT frequency as shown in Figure 4-4.

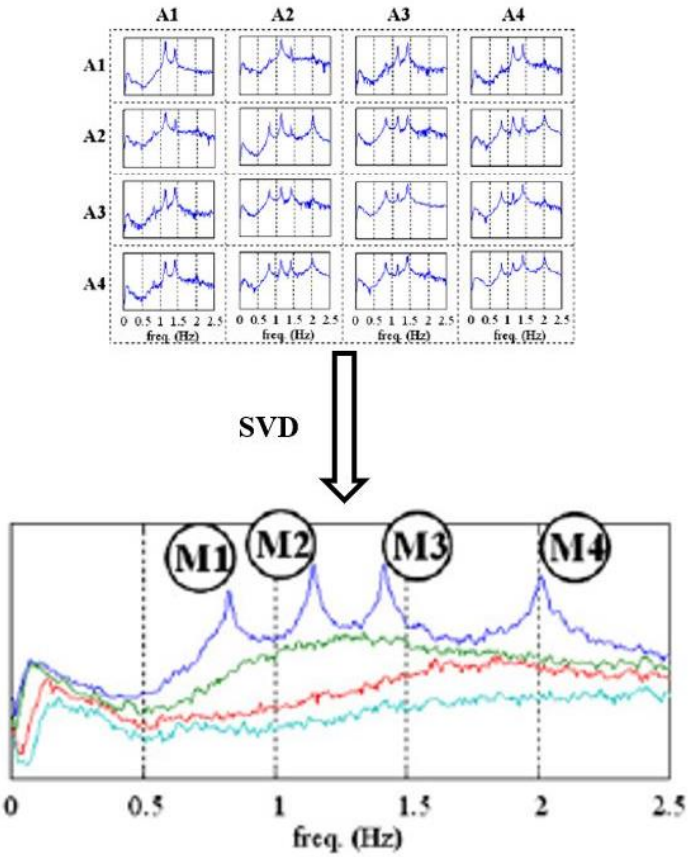


Figure 4-4. An illustration of mode estimation from the SVD of output spectrum matrices [107]. The largest singular value spectrum containing all the possible modes marked by symbol M. (A1~A4 represent measurements of acceleration from four different positions of an arch bridge.)

#### 4.4.2.B Poly-reference least square complex frequency-domain (P-LSCF) method

A right matrix-fraction half-spectrum matrix at a given discrete frequency $\omega_j$ is modelled as below

$$\mathbf{S}_{yy}^{+}(\omega_j) = \mathbf{B}\mathbf{A}^{-1} = \left[\sum_{r=0}^{p} \mathbf{B}_r e^{i\omega_j \Delta t r}\right]\left[\sum_{r=0}^{p} \mathbf{A}_r e^{i\omega_j \Delta t r}\right]^{-1} \quad (4\text{-}17)$$

$\mathbf{A}_r, \mathbf{B}_r$ are matrices of polynomial coefficients, $p$ is the order of the polynomials and $\Delta t$ is the sampling time. The difference between the measured and theoretical half spectrum matrix is

$$\mathbf{E}^{NLS}(\omega_j) = \left[\sum_{r=0}^{p} \mathbf{B}_r e^{i\omega_j \Delta t r}\right]\left[\sum_{r=0}^{p} \mathbf{A}_r e^{i\omega_j \Delta t r}\right]^{-1} - \hat{\mathbf{S}}_{yy}^{+}(\omega_j) \quad (4\text{-}18)$$

where $NLS$ represents non-linear least square.

To further linearize the difference by multiplying the denominator.

$$\mathbf{E}^{LS}(\omega_j) = \left[\sum_{r=0}^{p} \mathbf{B}_r e^{i\omega_j \Delta t r}\right] - \hat{\mathbf{S}}_{yy}^{+}(\omega_j)\left[\sum_{r=0}^{p} \mathbf{A}_r e^{i\omega_j \Delta t r}\right] \quad (4\text{-}19)$$

where $LS$ represents linear least square and $\mathbf{E}^{LS}(\omega_j) \in \mathbb{C}^{n_o \times n_o}$ with the errors $\mathbf{E}_{o,r}(\omega_j)$ to be minimised.

Instead of Equation 4-19, the problem is solved by least square cost function as following equation, which is evaluated at all the discrete frequency values, $\omega_1$ to $\omega_{n_f}$

$$\varepsilon = \sum_{o=1}^{n_o} \sum_{r=1}^{n_o} \sum_{j=1}^{n_f} \mathbf{E}_{o,r}(\omega_j) \mathbf{E}_{o,r}(\omega_j)^{*} \quad (4\text{-}20)$$

, where $n_o$ is the number of outputs and $n_f$ is the number of DFT frequencies.

By defining some variables, the cost function can be simplified. Assume the polynomial

basis functions at $\omega_j$ frequency is

$$\boldsymbol{\Omega}(\omega_j) = \begin{bmatrix} \Omega_0(\omega_j) & \Omega_1(\omega_j) & \dots & \Omega_{\mathrm{p}}(\omega_j) \end{bmatrix}$$

$$= \begin{bmatrix} e^{i\omega_j \Delta t0} & e^{i\omega_j \Delta t1} & \dots & e^{i\omega_j \Delta tp} \end{bmatrix} \quad (4\text{-}21)$$

Then, one general line $o$ of the error matrix can be calculated with the following equation (the subscript $LS$ was dropped to simplify the notation):

$$E_o(\omega_j) = \boldsymbol{\Omega}(\omega_j) \cdot \begin{bmatrix} \mathbf{B}_{0_o} \\ \mathbf{B}_{1_o} \\ \vdots \\ \mathbf{B}_{p_o} \end{bmatrix} + \begin{bmatrix} -\Omega_0(\omega_j)\hat{\mathbf{S}}_{yyo}^{+} & -\Omega_1(\omega_j)\hat{\mathbf{S}}_{yyo}^{+} & \dots & -\Omega_{\mathrm{p}}(\omega_j)\hat{\mathbf{S}}_{yyo}^{+} \end{bmatrix} \begin{bmatrix} \mathbf{A}_0 \\ \mathbf{A}_1 \\ \vdots \\ \mathbf{A}_p \end{bmatrix}$$

(4-22)

By the following definitions, Equation 4-22 can be generalised to all the discrete frequency values, $\omega_1$ to $\omega_{n_f}$

$$\mathbf{E}_o(\boldsymbol{\beta}_o, \boldsymbol{\alpha}) = \begin{bmatrix} \mathbf{X}_o & \mathbf{Y}_o \end{bmatrix} \begin{bmatrix} \boldsymbol{\beta}_o \\ \boldsymbol{\alpha} \end{bmatrix} \quad (4\text{-}23)$$

, where

$$\boldsymbol{\beta}_o = \begin{bmatrix} \mathbf{B}_{0_o} \\ \mathbf{B}_{1_o} \\ \vdots \\ \mathbf{B}_{p_o} \end{bmatrix}, \boldsymbol{\alpha} = \begin{bmatrix} \mathbf{A}_0 \\ \mathbf{A}_1 \\ \vdots \\ \mathbf{A}_p \end{bmatrix}$$

$$\mathbf{X}_o = \begin{bmatrix} \mathbf{\Omega}(\omega_1) \\ \vdots \\ \mathbf{\Omega}(\omega_{n_f}) \end{bmatrix}$$

$$\mathbf{Y}_o = -\begin{bmatrix} \Omega_0(\omega_1)\hat{\mathbf{S}}^+_{yyo}(\omega_1) & \Omega_1(\omega_1)\hat{\mathbf{S}}^+_{yyo}(\omega_1) & \dots & \Omega_{\mathrm{p}}(\omega_1)\hat{\mathbf{S}}^+_{yyo}(\omega_1) \\ \dots & \dots & \dots & \vdots \\ \Omega_1\left(\omega_{n_f}\right)\hat{\mathbf{S}}^+_{yyo}\left(\omega_{n_f}\right) & \Omega_1\left(\omega_{n_f}\right)\hat{\mathbf{S}}^+_{yyo}\left(\omega_{n_f}\right) & \dots & \Omega_{\mathrm{p}}\left(\omega_{n_f}\right)\hat{\mathbf{S}}^+_{yyo}\left(\omega_{n_f}\right) \end{bmatrix}$$

With Equation 4-23, the cost function can be expressed as

$$\varepsilon(\beta_o, \alpha) = \sum_{o=1}^{n_o} tr\{\mathbf{E}_o(\boldsymbol{\beta}_o, \boldsymbol{\alpha})^H \mathbf{E}_o(\boldsymbol{\beta}_o, \boldsymbol{\alpha})\}$$

$$= \sum_{o=1}^{n_o} tr\{[\boldsymbol{\beta}_o^T \quad \boldsymbol{\alpha}^T] \begin{bmatrix} \mathbf{R}_o & \mathbf{S}_o \\ \mathbf{S}_o^T & \mathbf{T}_o \end{bmatrix} \begin{bmatrix} \boldsymbol{\beta}_o \\ \boldsymbol{\alpha} \end{bmatrix}\} \tag{4-24}$$

where

$$\mathbf{R}_o = Re(\mathbf{X}_o^H \mathbf{X}_o), \mathbf{S}_o = Re(\mathbf{X}_o^H \mathbf{Y}_o), \mathbf{T}_o = Re(\mathbf{Y}_o^H \mathbf{Y}_o)$$

and $tr(\cdot)$ means the trace, or the sum of the elements in the main diagonal, of a matrix and $Re(\cdot)$ selects the real part of a complex number.

The minimum of the cost function is then determined by forcing its derivatives with respect to the unknowns to become zero:

$$\begin{cases} \frac{\partial \varepsilon}{\partial \boldsymbol{\beta}_o} = 0 \\ \frac{\partial \varepsilon}{\partial \boldsymbol{\alpha}} = 0 \end{cases} \tag{4-25}$$

And

$$2(\mathbf{R}_o \boldsymbol{\beta}_o + \mathbf{S}_o \boldsymbol{\alpha}) = 0 \Leftrightarrow \boldsymbol{\beta}_o = -\mathbf{R}_o^{-1} \mathbf{S}_o \boldsymbol{\alpha} \tag{4-26}$$

$$2\sum_{o=1}^{n_o} (\mathbf{T}_o - \mathbf{S}_o^T \mathbf{R}_o^{-1} \mathbf{S}_o)\boldsymbol{\alpha} = 0 \Leftrightarrow \mathbf{M}\boldsymbol{\alpha} = 0 \tag{4-27}$$

The stochastic state-space system matrix and output matrix using right fraction-matrix model parameters are

$$\mathbf{A} = \begin{bmatrix} -\mathbf{A}_p^{-1}\mathbf{A}_{p-1} & -\mathbf{A}_p^{-1}\mathbf{A}_{p-2} & \cdots & -\mathbf{A}_p^{-1}\mathbf{A}_1 & -\mathbf{A}_p^{-1}\mathbf{A}_0 \\ \mathbf{I} & \mathbf{0} & \cdots & \mathbf{0} & \mathbf{0} \\ \vdots & \ddots & \cdots & \vdots & \vdots \\ \mathbf{0} & \mathbf{0} & \cdots & \mathbf{I} & \mathbf{0} \end{bmatrix}$$

$$\mathbf{C} = \begin{bmatrix} \mathbf{B}_{p-1} - \mathbf{B}_p\mathbf{A}_p^{-1}\mathbf{A}_{p-1} & \cdots & \mathbf{B}_0 - \mathbf{B}_p\mathbf{A}_p^{-1}\mathbf{A}_o \end{bmatrix} \quad (4\text{-}28)$$

After the system matrix is estimated, the stable system modes can be identified by drawing a stabilisation diagram as described in the previous section.

### 4.4.2.C Bayesian method

By assuming classical damping, the acceleration data is denoted as

$$\hat{\ddot{\mathbf{x}}}_j = \sum_i \boldsymbol{\phi}_i \ddot{\eta}_i(t_j) + \boldsymbol{\varepsilon}_j \quad (4\text{-}29)$$

where $i$ is the mode number, $j$ is the sample number, $\boldsymbol{\phi}_i \in \mathbb{R}^n$ is the ith mode shape, $\boldsymbol{\varepsilon}_j \in \mathbb{R}^n$ is the predition error and $\eta_i(t)$ is the ith modal response which satisfies the uncoupled modal equation as following

$$\ddot{\eta}_i(t) + 2\zeta_i\omega_i\dot{\eta}_i(t) + \omega_i^2\eta_i(t) = p_i(t) \quad (4\text{-}30)$$

where $\omega_i = 2\pi f_i$, $f_i$ is the natural frequency, $\zeta_i$ is the damping ratio, and $p_i(t)$ is the modal force.

The fast Fourier transform (FFT) of $\hat{\ddot{\mathbf{x}}}_j$ is

$$\boldsymbol{\mathcal{F}}_k = \sqrt{\frac{2\Delta t}{N}} \sum_{j=1}^{N} \hat{\ddot{\mathbf{x}}}_j \exp\left[-2\pi i \frac{(k-1)(j-1)}{N}\right] \quad (k = 1, \ldots, N) \quad (4\text{-}31)$$

The covariance matrix formulated from the Fourier coefficients and the unknown parameters is

$$\mathbf{C}_k = \frac{1}{2}\begin{bmatrix} \boldsymbol{\Phi}\mathrm{Re}\mathbf{H}_\mathrm{k}\boldsymbol{\Phi}^\mathrm{T} & -\boldsymbol{\Phi}\mathrm{Im}\mathbf{H}_\mathrm{k}\boldsymbol{\Phi}^\mathrm{T} \\ \boldsymbol{\Phi}\mathrm{Im}\mathbf{H}_\mathrm{k}\boldsymbol{\Phi}^\mathrm{T} & \boldsymbol{\Phi}\mathrm{Re}\mathbf{H}_\mathrm{k}\boldsymbol{\Phi}^\mathrm{T} \end{bmatrix} + \frac{S_e}{2}\mathbf{I}_{2n} \quad (4\text{-}32)$$

where $\boldsymbol{\Phi} = [\boldsymbol{\phi}_1, \ldots, \boldsymbol{\phi}_\mathrm{m}] \in \mathbb{R}^{n\times m}$ is the mode shape matrix; $S_e$ is the (constant) spectral density of the prediction error; $\mathbf{I}_{2n}$ is the $2n \times 2n$ identity matrix; $\mathbf{H}_k = diag(\mathbf{h}_k)\mathbf{S}\, diag(\mathbf{h}_k^*) \in \mathbb{C}^{m\times m}$ is the theoretical spectral density matrix of the modal acceleration responses, where $\mathbf{S} \in \mathbb{C}^{m\times m}$ is the (constant) spectral density matrix of modal forces; $\mathbf{h}_k$ is a vector of modal transfer functions with the ith element equal to $h_{ik} = [(\beta_{ik}^2 - 1) + i(2\zeta_i\beta_{ik})]^{-1}$, and $diag(\mathbf{h}_k) \in \mathbb{C}^{m\times m}$ denotes a diagonal matrix with the ith diagonal element equal to $h_{ik}$; * denotes complex conjugate transpose; $\beta_{ik} = f_i/f_k$ is a frequency ratio.

The element of $\mathbf{H_k}$ is

$$\mathbf{H}_k(i,j) = S_{ij}h_{ik}h_{jk}^* \quad (4\text{-}33)$$

Generally speaking, $\mathbf{S}^* = \mathbf{S}$, i.e. $\mathbf{S}$ is a Hermitian matrix.

According to Bayesian theory,

$$p(\theta|D,M) = p(D|M)^{-1}p(D|\theta,M)p(\theta|M) \quad (4\text{-}34)$$

where $D$ denotes the measured data, $M$ is the modeling assumption, and $\theta$ is a set of parameters to be identified.

The posterior probability density function (PDF) is proportional to the negative log-likelihood function (NLLF)

$$p(\theta|D,M) \propto exp[-L(\theta)] \tag{4-35}$$

where

$$L(\theta) = \frac{1}{2}\sum_k \ln \det \mathbf{C}_k(\theta) + \frac{1}{2}\sum_k \mathbf{Z}_k^T \mathbf{C}_k(\theta)^{-1} \mathbf{Z}_k \tag{4-36}$$

where $\mathbf{Z_k} = [Re\mathbf{F}_k; Im\mathbf{F}_k] \in \mathbb{R}^{2n}$.

The log-likelihood function provided in Equation 4-36 is relatively complicated for computation, thus through mathematical derivation, Au [53] provided a faster algorithm for the calculation of the NLLF. The new NLLF with $\theta = \{f, \zeta, S, \sigma^2\}$ is presented as

$$L(f, \zeta, S, \sigma^2)$$

$$= -nN_f ln2 + (n-1)N_f ln\sigma^2 + \sum_k \ln(SD_k + \sigma^2) + \sigma^{-2}(d - \hat{\lambda}) \tag{4-37}$$

, where $D_k = [(\beta_k^2 - 1)^2 + (2\zeta\beta_k)^2]^{-1}$, $\beta_k = f/f_k$, $\mathbf{A} = \sum_k [1 + (\sigma^2/SD_k)]^{-1} \mathbf{D}_k$, $\mathbf{D}_k = \mathbf{F}_k\mathbf{F}_k^T + \mathbf{G}_k\mathbf{G}_k^T$, $d = \sum_k(\mathbf{F}_k^T\mathbf{F}_k + \mathbf{G}_k^T\mathbf{G}_k)$, $\hat{\lambda}$ is the largest eigenvalue of $\mathbf{A}$, $N_f$ is the number of discrete frequency points, $\sigma^2$ is the spectral density of prediction error, and $S$ is the spectral density, $\mathbf{F}_k = Re(\boldsymbol{\mathcal{F}}_k)$ and $\mathbf{G}_k = Im(\boldsymbol{\mathcal{F}}_k)$.

Summary of the procedure:

1. Calculate the Fourier sequence $\boldsymbol{\mathcal{F}}_k$ of a chosen bandwidth from singular value spectrum and corresponding parameters.

2. Numerically optimise Equation 4-36 with respect to $\{f; \zeta; S; \sigma^2\}$. During optimisation, the most probable value (MPV) of $\boldsymbol{\phi}$ is calculated as the eigenvector of $\mathbf{A}$ with the largest eigenvalue. If the asymptotic MPVs have been calculated, they may be used as initial guess. Otherwise, the initial guess of $f$ can be obtained from the singular value spectrum. The initial guess of $\zeta$ may be set as 1%. The initial guess of $\sigma^2$ can be set as $(d - \hat{\lambda}_0)/(n-1)N_f$. By noting that the value of $trace(\mathbf{D}_k)$ at the resonant peak is approximately $S/4\sigma^2\zeta^2$, the initial guess of $S$ may be set as this value multiplied by $4\sigma^2\zeta^2$. $\hat{\lambda}_0$ is the maximum eigenvalue of $\mathbf{A}_0 = \sum_k \mathbf{D}_k$.

### 4.5 Closure

The OMA methods introduced in this chapter are applied in the analysis of data in Chapter 6 and 7. The SSI and P-LSCF methods are based upon the assumption of discrete-time stochastic state-space model and the drawing of stablisation diagram for the identification of possible stable modes and corresponding modal parameters. For the formation of Hankel or spectral matrix, the measured signals are segmented and arranged in a specified way with user-chosen parameters, such as the dimension of matrix and the length of segment. On the other hand, Bayesian method relies on the use of largest singular value spectrum built from FDD method for the selection of DFT data within an assigned bandwidth and the initial guess of natural frequency. Each set of modal parameters of a particular mode are determined individually from one set of DFT data related to a particular peak in the spectrum, which is different from state-space model methods. However, the methods mentioned herein in general have similar identification results. A verification of the OMA methods used in the thesis is provided in Appendix B.

# 5 Decomposition of Images by using Shape Descriptors

The idea of the shape descriptor of a shape (also known as the moment descriptor) comes from pattern recognition in the computer vision discipline. The accuracy of pattern or character recognition is often influenced by position, size, and orientation, thus Hu [73] proposed the use of geometric moments to recognise shapes. He took advantage of the property of invariance of geometric moments under translation and rotation. Other than geometric moments, there are several kernel functions which can be applied for shape decomposition, and they are introduced in the following sections. For this chapter, the mathematical formulas of some of the most widely used descriptors are provided. The geometric descriptor is the earliest SD developed and it is used as the initial guess in the AGMD method, which is the latest adaptive SD developed. Tchebichef and Zernike descriptors are the most common SDs applied, and they are suitable for rectangular and circular domains, respectively.

## 5.1 Image decomposition and reconstruction

The relation between the image to be decomposed, the basis functions and shape descriptors are introduced here. The shape descriptors (or coefficients) are acquired by projecting an image onto the kernel functions as following

$$SD_i = \frac{<\mathbf{\Lambda}(x,y),\mathbf{S_i}(x,y)>}{<\mathbf{S_i}(x,y),\mathbf{S_i}(x,y)>} \tag{5-1}$$

where $SD_i$ represents the shape descriptor corresponding to the $i^{th}$ basis (or kernel) function $\mathbf{S_i}(x,y)$ and $\mathbf{\Lambda}(x,y)$ denotes the image to be decomposed. For the definition of $<\cdot>$ please refer to Appendix A.

The reconstruction of shape is given by the summation of the products of shape descriptors and kernels

$$\widehat{\mathbf{\Lambda}}(x,y) = \sum_i SD_i \cdot \mathbf{S}_i\,(x,y) \tag{5-2}$$

From the simple example in Figure 5-1, the concept of shape decomposition can be clearly demonstrated. A 3D sinusoidal shape placed at 45 degrees relative to x and y axes is shown in Figure 5-1 (a). This shape can be expressed as a linear combination of coefficients (shape descriptors) in Figure 5-1 (b) and the kernels in Figure 5-1 (c).

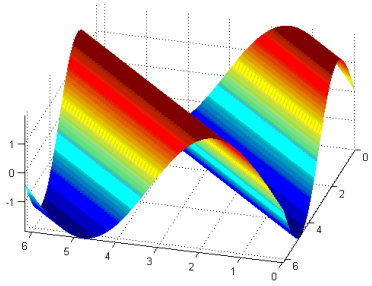

(a) 3D sine shape

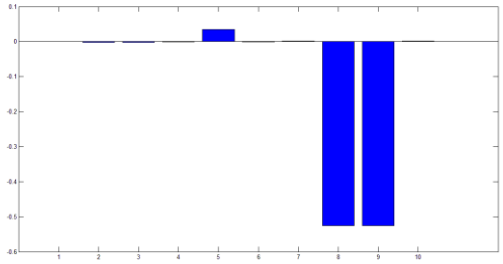

(b) Shape descriptors

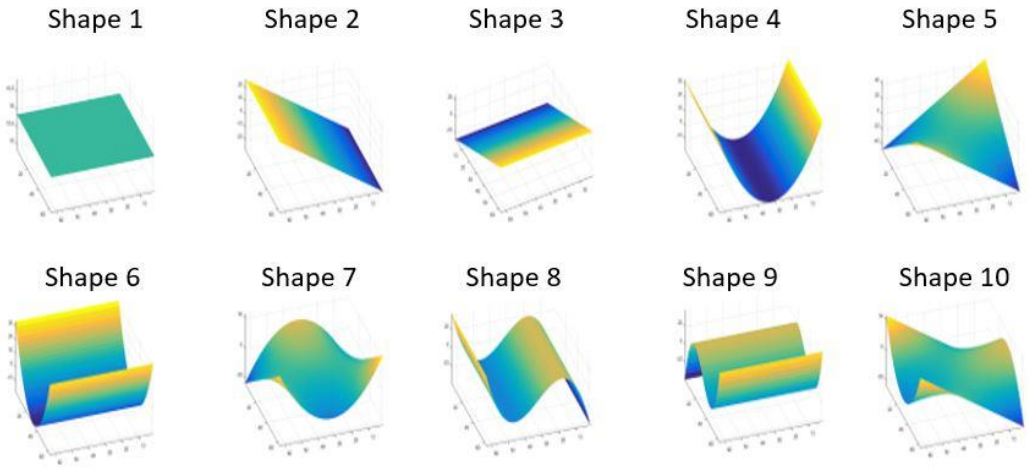


(c) Shape basis

Figure 5-1. A simple example for the explanation of shape decomposition.

The correlation coefficient is defined as

$$\rho(\mathbf{\Lambda}(x,y),\widehat{\mathbf{\Lambda}}(x,y)) = \frac{1}{N-1}\sum_{i=1}^{N}\frac{(\mathbf{\Lambda_i}(x,y)-\mu_{\mathbf{\Lambda}})(\widehat{\mathbf{\Lambda}}_i(x,y)-\mu_{\widehat{\mathbf{\Lambda}}})}{(\sigma_{\mathbf{\Lambda}})(\sigma_{\widehat{\mathbf{\Lambda}}})} \tag{5-3}$$

where $\mu$ is the mean and $\sigma$ is the standard deviation of either original or reconstructed image function, and $N$ is the pixel count in the discretised image.

## 5.2 Geometric moment descriptor

The geometric monomials may be written as,

$$G_{pq}(x, y) = x^p y^q \tag{5-4}$$

where $x$ and $y$ are coordinates, and $p, q \in \mathbf{N}$ are monomial orders.

For an image $\mathbf{\Lambda}(x, y)$, the moment of order $(p + q)$ is defined as

$$m_{pq} = \int_{-\infty}^{\infty} \int_{-\infty}^{\infty} x^p y^q \mathbf{\Lambda}(x, y)\, dxdy \tag{5-5}$$

The central moment is defined accordingly as

$$\mu_{pq} = \int_{-\infty}^{\infty} \int_{-\infty}^{\infty} (x - \bar{x})^p (y - \bar{y})^q \mathbf{\Lambda}(x, y)\, dxdy \tag{5-6}$$

where

$$\bar{x} = \frac{m_{10}}{m_{00}}, \bar{y} = \frac{m_{01}}{m_{00}} \tag{5-7}$$

The geometric moment of order $(p + q)$ of a discrete shape function $\mathbf{\Lambda}(x, y)$ may be calculated as

$$m_{pq} = \sum_{x=1}^{N_x} \sum_{y=1}^{N_y} x^p y^q \mathbf{\Lambda}(x, y) \tag{5-8}$$

$$\mu_{pq} = \sum_{x=1}^{N_x} \sum_{y=1}^{N_y} (x - \bar{x})^p (y - \bar{y})^q \mathbf{\Lambda}(x, y) \tag{5-9}$$

where $N_x, N_y$ denote the pixel counts in the discretised image along horizontal and vertical axes.

Given by Hu [72], there are seven moment invariants with respect to translation,

scaling, rotation and reflection.

$$\tau_1 = \eta_{20} + \eta_{02} \tag{5-10}$$

$$\tau_2 = (\eta_{20} - \eta_{02})^2 + 4\eta_{11}^2 \tag{5-11}$$

$$\tau_3 = (\eta_{30} - \eta_{03})^2 + (3\eta_{21} - \eta_{03})^2 \tag{5-12}$$

$$\tau_4 = (\eta_{30} + \eta_{12})^2 + (\eta_{21} + \eta_{03})^2 \tag{5-13}$$

$$\tau_5 = (\eta_{30} - 3\eta_{12})(\eta_{30} + \eta_{12})[(\eta_{30} + \eta_{12})^2 - 3(\eta_{21} + \eta_{03})^2]$$

$$+(3\eta_{21} - \eta_{03})(\eta_{21} + \eta_{03})[3(\eta_{30} + \eta_{12})^2 - (\eta_{21} + \eta_{03})^2] \tag{5-14}$$

$$\tau_6 = (\eta_{20} - \eta_{02})[(\eta_{30} + \eta_{12})^2 - (\eta_{21} + \eta_{03})^2]$$

$$+4\eta_{11}(\eta_{30} + \eta_{12})(\eta_{21} + \eta_{03}) \tag{5-15}$$

and the last one is the skew invariant,

$$\tau_7 = (3\eta_{21} - \eta_{03})(\eta_{30} + \eta_{12})[(\eta_{30} + \eta_{12})^2 - 3(\eta_{21} + \eta_{03})^2]$$

$$+(\eta_{30}-3\eta_{12})(\eta_{21}+\eta_{03})[3(\eta_{30}+\eta_{12})^2-(\eta_{21}+\eta_{03})^2] \quad (5\text{-}16)$$

where

$$\eta_{pq}=\mu_{pq}/\mu_{00}^{w} \quad (5\text{-}17)$$

and

$$w=1+\frac{(p+q)}{2}, for\ (p+q)=2,3,\dots \quad (5\text{-}18)$$

The basis of geometric moments is not orthogonal, which means that the moment sequence contains redundant information. Also, the high-order terms tend to be very sensitive to noise. Therefore, an orthogonal polynomial basis is preferred for a compact and representative shape decomposition.

## 5.3 Tchebichef moment descriptor

### 5.3.1 Theory

The Tchebichef polynomials [75] is suitable for the decomposition of images confined within rectangular domains. The polynomial is calculated recursively starting from the Equation 5-19 for the zeroth order and Equation 5-20 for the first order functions, and the higher order polynomials are just the combination of lower order ones as shown in Equation 5-21. The first 6 scaled one-dimensional Tchebichef kernels can be seen in Figure 5-2.

$$\tau_0(x)=1, x=0,\dots,N-1 \quad (5\text{-}19)$$

$$\tau_1(x) = \frac{2x+1-N}{N}, x = 0, \dots, N-1 \quad (5\text{-}20)$$

$$\tau_n(x) = \frac{(2n-1)\tau_1(x)\tau_{n-1}(x) - (n-1)\left(1-\frac{(n-1)^2}{N^2}\right)\tau_{n-2}(x)}{n}, n > 1, x = 0, \dots, N-1 \quad (5\text{-}21)$$

where the subscript $n$ represents the order of Tchebichef kernel, $x$ is the coordinate, and $N$ is the total number of discrete points.

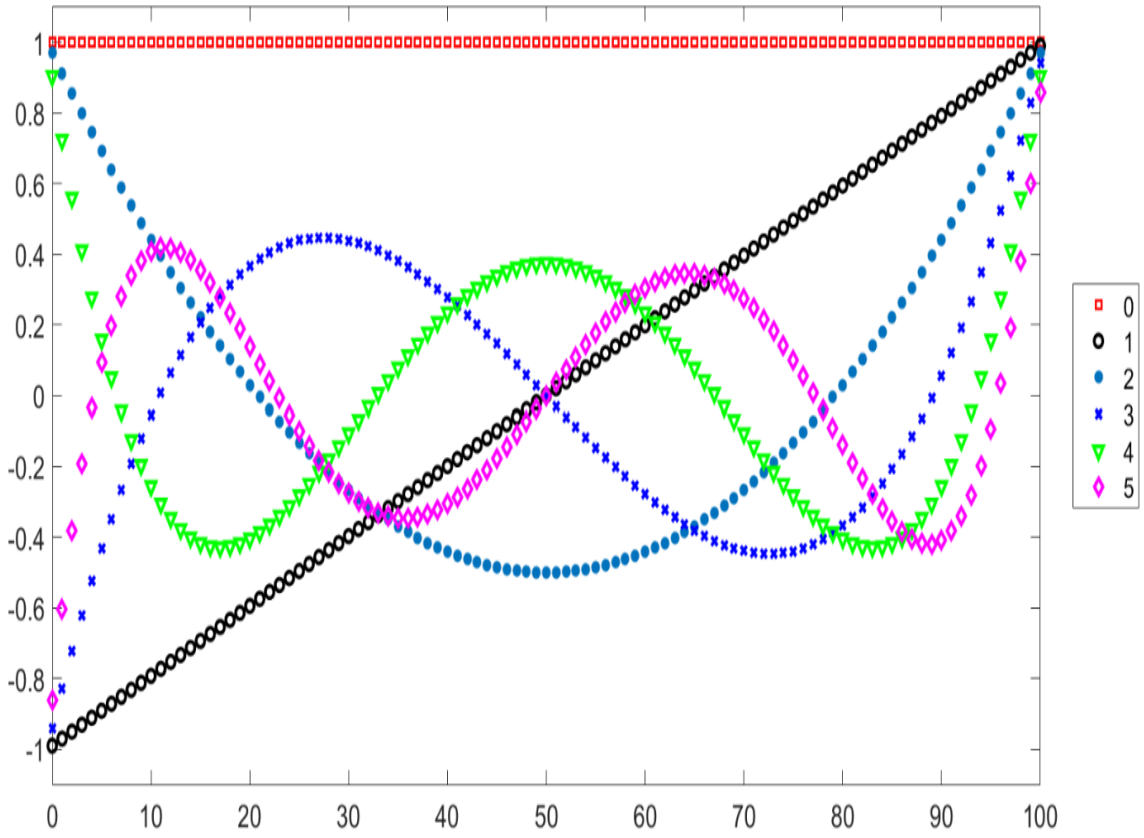


Figure 5-2. Scaled 1D Tchebichef moment. $N$ = 101. (x axis – position, y axis – magnitude)

For 2D Tchebichef polynomials, they are the products of 1D Tchebichef polynomials as described in Equation 5-22. The first 16 2D scaled Tchebichef polynomials are illustrated in Figure 5-3, which are useful for the decomposition of

shape in rectangular domain.

$$T_{pq}(x,y) = \text{ד}_p(x)\text{ד}_q(y) \tag{5-22}$$

where $x, y$ are coordinates, and $p, q$ are polynomial orders in $x$ and $y$ direction, respectively.

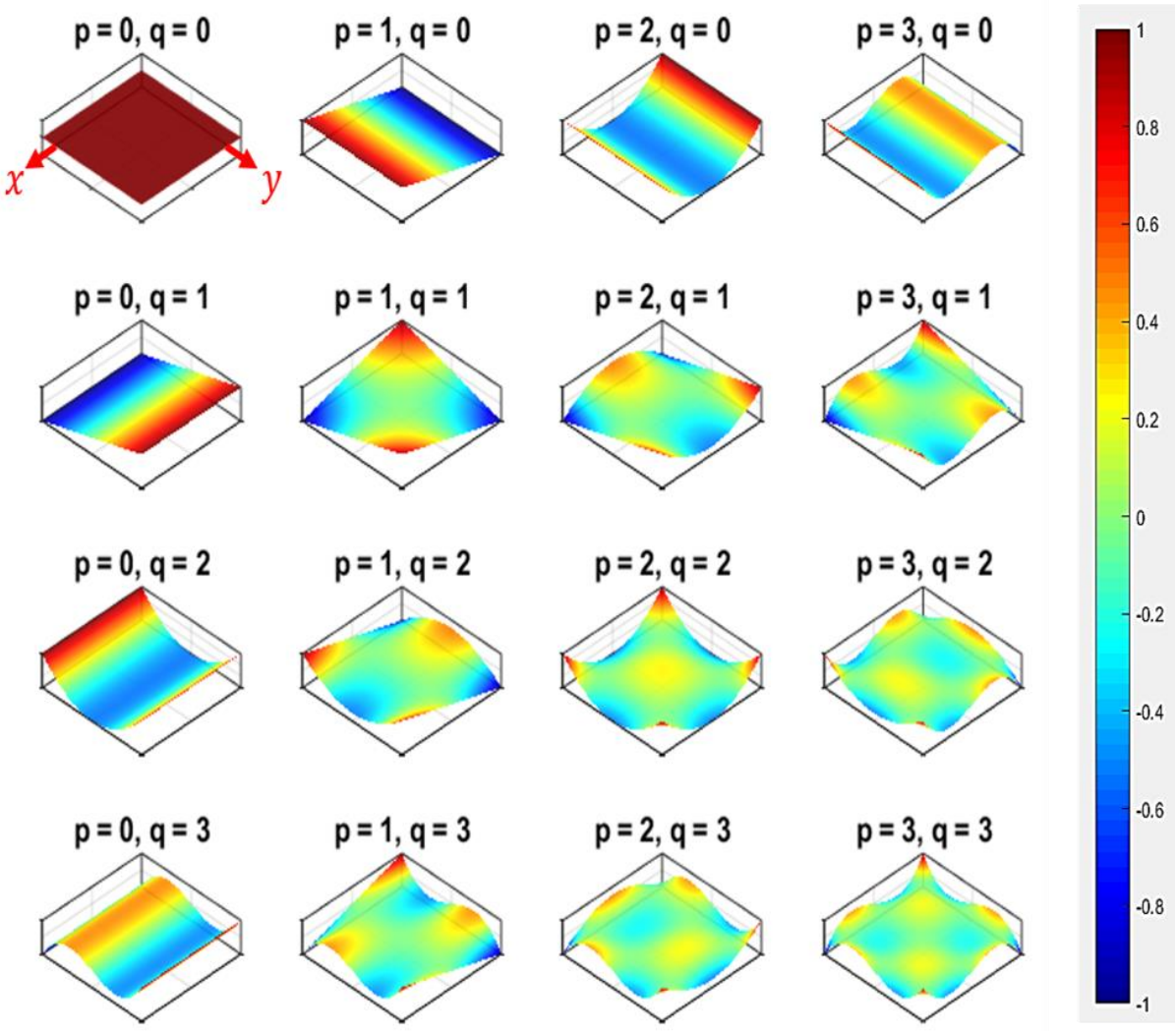


Figure 5-3. The first 16 2D scaled Tchebichef polynomials in rectangular domain.

### 5.3.2 Example

In order to demonstrate SD decomposition by using Tchebichef moment descriptors, the mode shapes of a rectangular plate with rectangular hole and non-symmetric boundary conditions in Figure 5-4 are served as the image to be decomposed. The parameters of simulation are provided in Table 5-1, and the mode shapes are given in Figure 5-5.

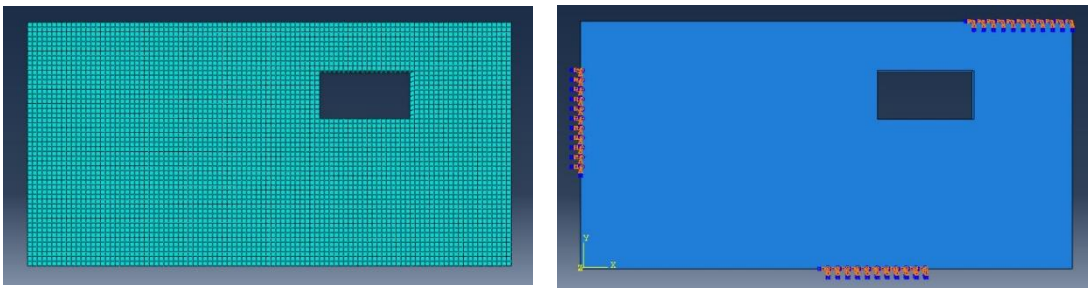

(a) Mesh (b) Boundary conditions

Figure 5-4. FE model of plate.

Table 5-1. The parameters of simulation – plate with a rectangular hole.

| | |
|---|---|
| Length | 1 m |
| Width | 0.5 m |
| Thickness | 0.03 m |
| Density | 7850 $kg/m^3$ |
| Young's modulus | 200 GPa |
| Poisson ratio | 0.26 |

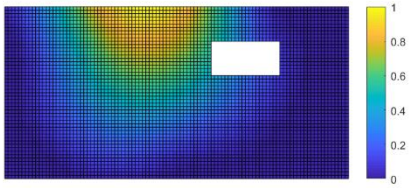


(a) 26.418 Hz

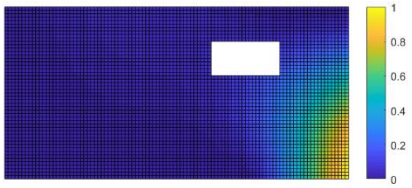


(b) 33.549 Hz

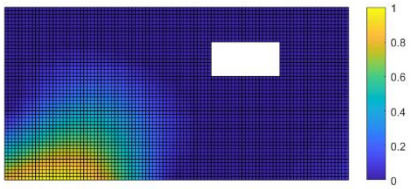


(c) 43.574 Hz

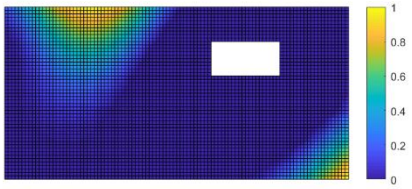


(d) 59.377 Hz

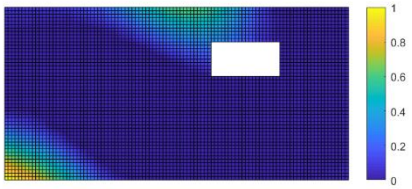


(e) 70.536 Hz

Figure 5-5. Mode shapes of plate.

The orders of Tchebichef polynomials involved in the decomposition of the example range from 1 to 10 for $p$ and 1 to 5 for $q$, respectively, and the orthogonality map is provided in Figure 5-6. From Figure 5-7, the necessary number of terms of Tchebichef polynomials for a reconstruction with a correlation coefficient higher than 95 % is 9. As shown in Figure 5-8 (a), the reconstructed mode shape is quite similar to

the original one. By increasing the number of terms to 15, i.e. with a correlation coefficient higher than 99 %, the difference between the original and reconstructed becomes subtle as shown in Figure 5-8 (b).

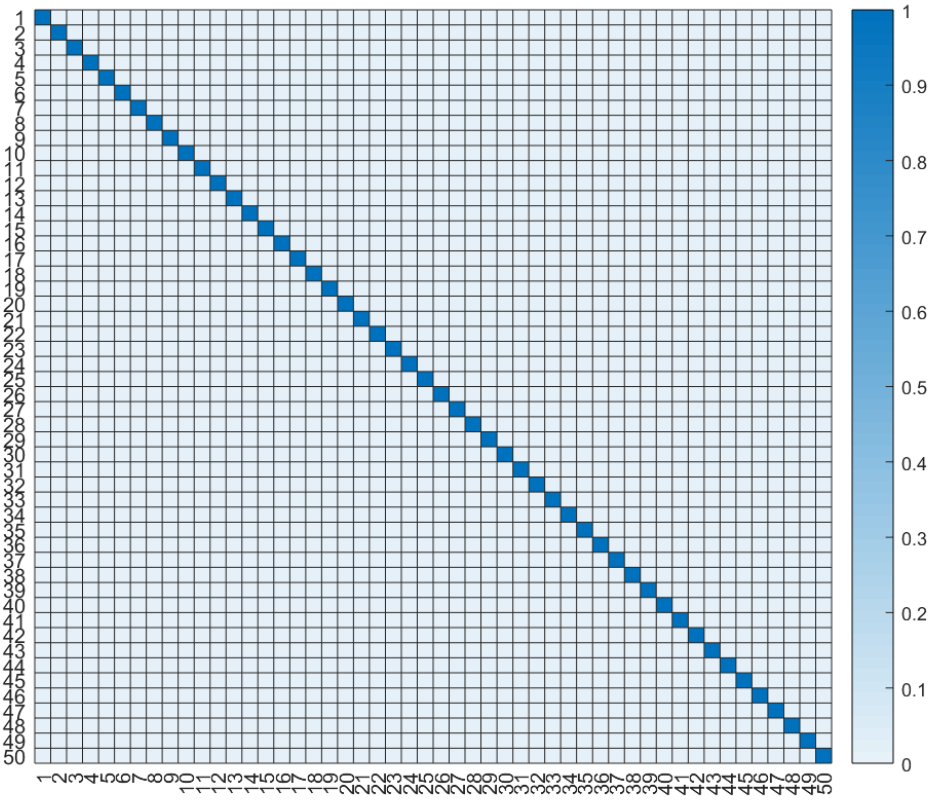


Figure 5-6. The orthogonality map of the Tchebichef polynomials used in the example.

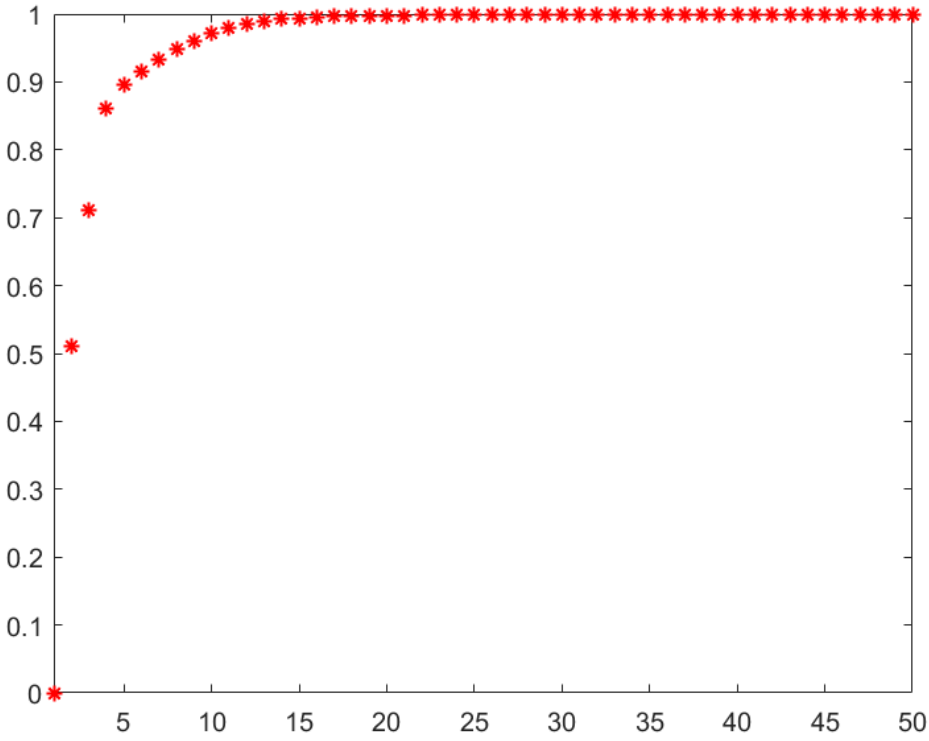


Figure 5-7 Correlation of original and reconstructed mode shapes of mode at 43.574 Hz. The horizontal axis is the number of terms of Tchebichef polynomials used for reconstruction, and the vertical axis is the correlation coefficient, which is between 0 and 1.

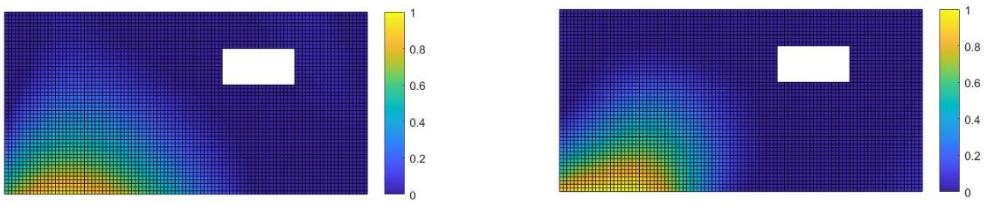


(a) Reconstruction with the first 9 significant terms of Tchebichef 2D polynomials

(b) Reconstruction with the first 15 significant terms of Tchebichef 2D polynomials

Figure 5-8. Reconstructed mode shape at 43.574 Hz with different terms of Tchebichef polynomials.

## 5.4 Zernike moment descriptor

### 5.4.1 Theory

Zernike moment descriptors [68, 74] are mostly applied to circular domains for shape decomposition, and the polynomials are calculated by Equation 5-23 with the first and the second equations representing even and odd Zernike kernels, respectively:

$$\begin{cases} Z_n^m(r,\theta) = R_n^m(r)\cos(m\theta)\,, m > 0 \\ Z_n^{-m}(r,\theta) = R_n^m(r)\sin(m\theta)\,, m < 0 \end{cases} \tag{5-23}$$

where $m$ and $n$ are nonnegative integers with $n \geq m$, $\theta$ is the azimuthal angle, $r$ is the radial distance $0 \leq r \leq 1$, and $R_n^m$ is the radial polynomial defined below.

$$R_n^m(r) = \begin{cases} \sum_{k=0}^{\frac{n-m}{2}} \frac{(-1)^k (n-k)!}{k!\left(\frac{n+m}{2}-k\right)!\left(\frac{n-m}{2}-k\right)!} r^{n-2m} & ,n-m\ even \\ 0 & ,n-m\ odd \end{cases} \tag{5-24}$$

The first 21 scaled Zernike polynomials can be seen in Figure 5-9.

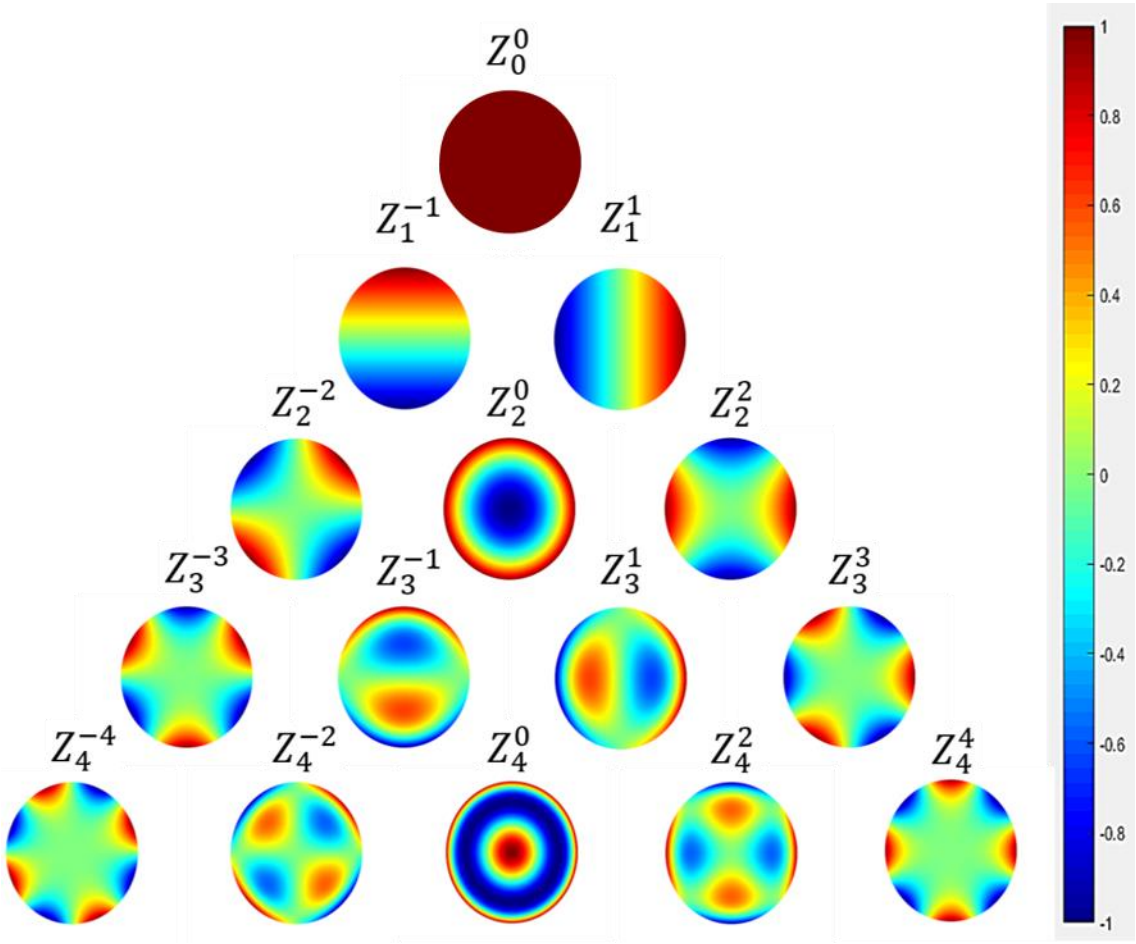


Figure 5-9. The first 21 scaled Zernike polynomials.

### 5.4.2 Example

In order to demonstrate SD decomposition by using Zernike moment descriptors, the mode shapes of a simulated circular disk in Figure 5-10 is served as the shape to be decomposed. The parameters of simulation can be seen in Table 5-2, and the mode shapes generated from finite element analysis are displayed in Figure 5-11.

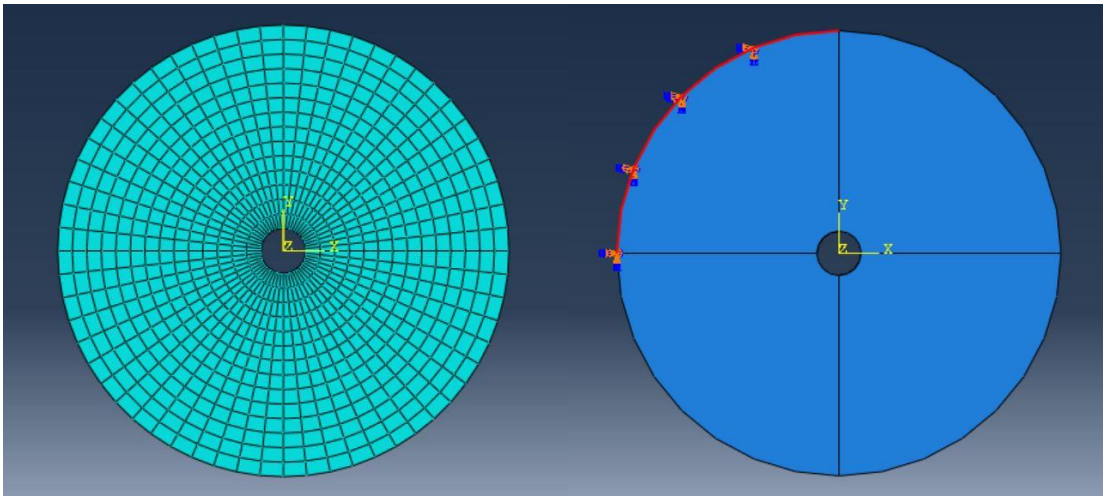

Figure 5-10. Circular disk with a hole and boundary condition. The upper left quadrant has all DOF fixed on the circumference.

Table 5-2. The parameters of simulation – circular disk.

| | |
|---|---|
| Outer radius | 1 m |
| Inner radius | 0.1 m |
| Thickness | 0.1 m |
| Density | 7850 $kg/m^3$ |
| Young's modulus | 200 GPa |
| Poisson ratio | 0.26 |

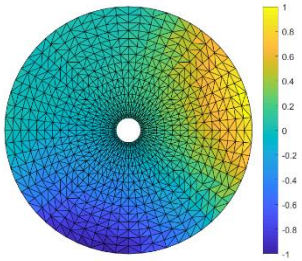

(a) 68.437 Hz

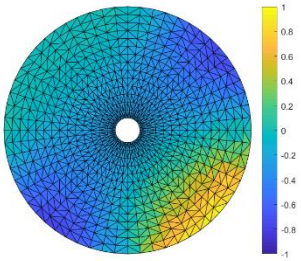

(b) 142.005 Hz

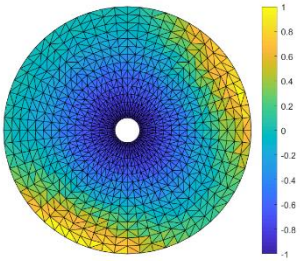

(c) 202.771 Hz

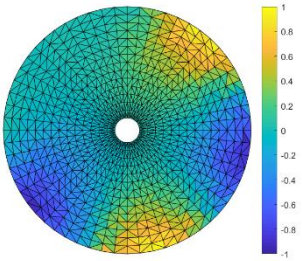

(d) 243.836 Hz

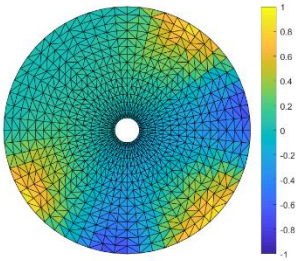

(e) 365.325 Hz

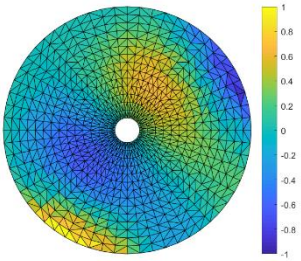

(f) 433.672 Hz

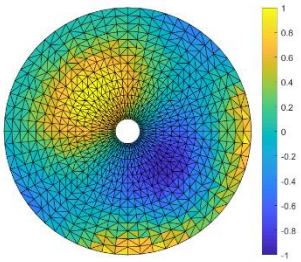

(g) 451.031 Hz

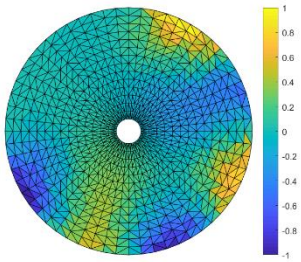

(h) 513.918 Hz

Figure 5-11. Mode shapes of circular disk.

The orders of Zernike polynomials applied for shape decomposition range from 0 to 6 for both m and n, and there are in total 28 Zernike polynomials. However, as can be seen from Figure 5-12, the discretized Zernike polynomials are not orthogonal anymore. An extra step of Gram–Schmidt orthonormalisation (GSO) procedure, which is explained in Appendix A.1, is necessary for the establishment of an orthonormal set of basis, which is crucial for successful reconstruction of image. By viewing Figure 5-13, it is obvious that the orthogonality of basis is confirmed. From Figure 5-14, the

correlation coefficient is increased gradually with the involvement of more terms of basis function but using 10 most significant terms is enough for a reconstruction with high correlation coefficient. A comparison of reconstructed mode shape is shown in Figure 5-15. The distribution of significant terms of descriptors can be seen in Figure 5-16. The correlation coefficients of reconstructed mode shapes involving all 28 terms of polynomials are listed in Table 5-3.

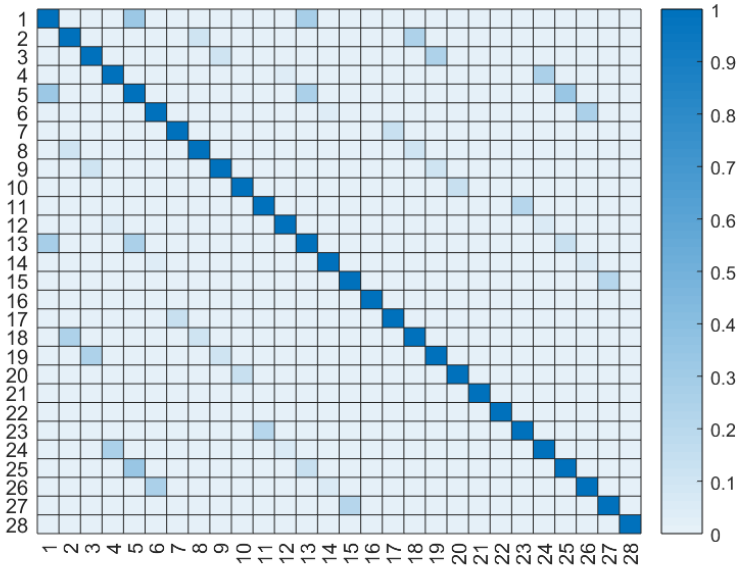

Figure 5-12. The original orthogonality map.

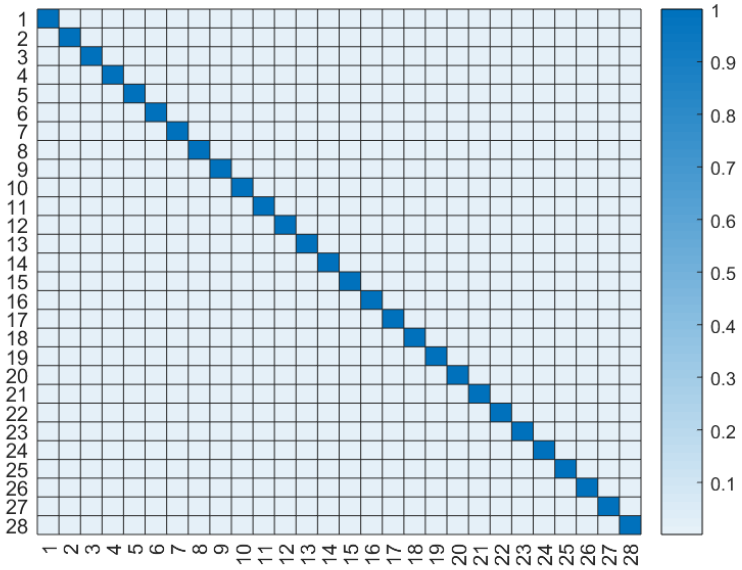

Figure 5-13. The diagonalised orthogonality map.

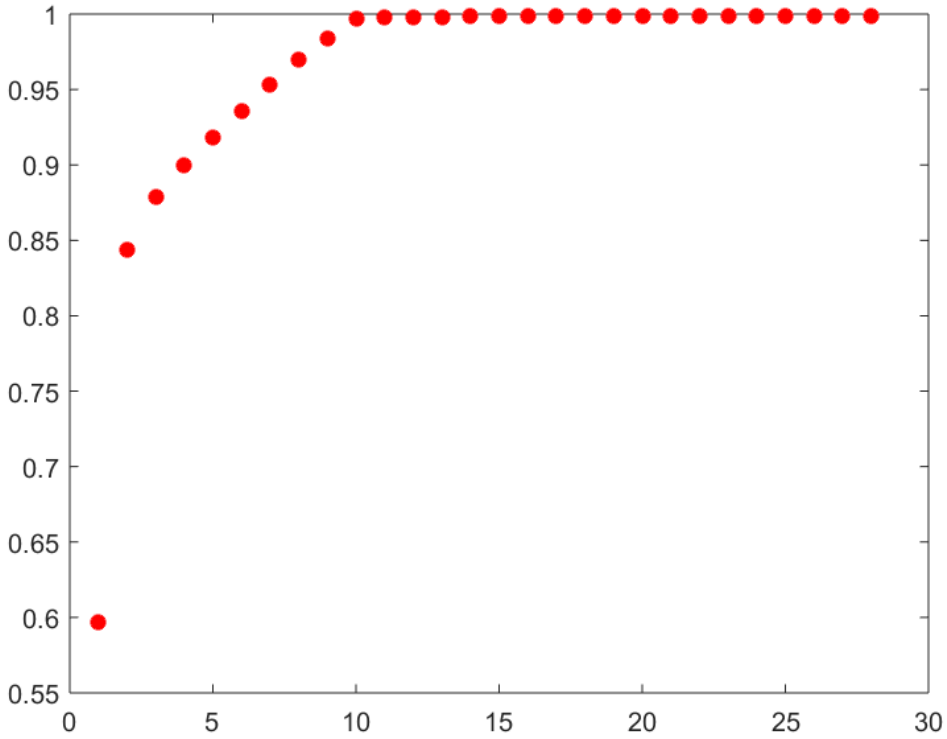


Figure 5-14. Correlation coefficient plot of reconstructed mode shape of 433.672 Hz. The horizontal axis is the number of terms of Zernike polynomials used for reconstruction, and the vertical axis is the correlation coefficient, ranging from 0 to 1.

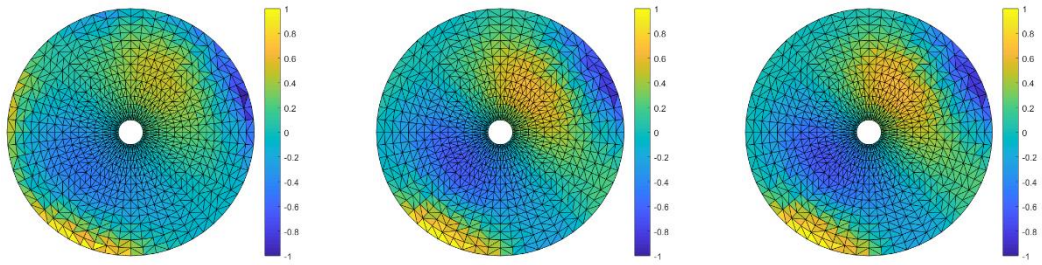

(a) First 5 significant terms. (b) First 10 significant terms. (c) All 28 terms.

Figure 5-15. The reconstructed mode shapes for mode at 433.672 Hz by Zernike moment descriptor.

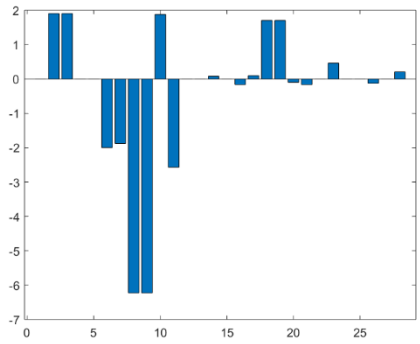

(a) 433.672 Hz

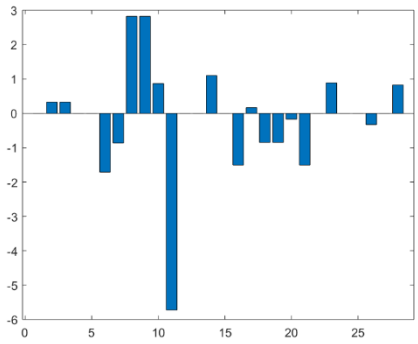

(b) 513.918 Hz

Figure 5-16. The Zernike moment descriptors bar charts.

Table 5-3. The correlation coefficients of reconstructed mode shapes by all 28 Zernike moment descriptors.

| Frequency | Correlation coefficient |
|---|---|
| 68.437 Hz | 0.9718 |
| 142.005 Hz | 0.9307 |
| 202.771 Hz | 0.9393 |
| 243.836 Hz | 0.9813 |
| 365.325 Hz | 0.9790 |
| 433.672 Hz | 0.9830 |
| 451.031 Hz | 0.9818 |
| 513.918 Hz | 0.9801 |

## 5.5 Adaptive geometric moment descriptor (AGMD)

### 5.5.1 Theory

For DIC measurement, the complexity of the measured domain for real engineering cases is much higher, i.e. there might be irregularities or discontinuities in

the image (possibly a displacement map). In terms of irregularity, it means that the outer boundary of the image does not belong to a simple geometry, such as a circle, ellipse, or rectangle, but might be a non-convex polygonal shape. Also, the measured surface of an object might contain holes or out-of-plane curvature, possibly resulting in internal no-data regions with inner boundaries. In order to apply SD technique to a measured domain with discontinuity and irregularity, Wang *et al.* [78] proposed the AGMD as a solution to the problem of finding basis functions applicable to general shapes as encountered in engineering. For the application of SD technique, it is firstly necessary to carry out an isomorphic mapping from the 3D surface to a 2D plane. In [77], this was achieved by bijectively using discrete conformal mapping as described by Desbrun et al. in [79]. This process involves meshing of the surface so that the difference in angle of individual triangular-element vertices on the curved surface and flat plane is minimised (Pinkall and Polthier in [80]). The surface parameterisation can be achieved by the following equation as mentioned in [79]

$$\begin{bmatrix} \lambda \mathbf{M}^{\mathrm{A}} & \mu \mathbf{M}^{\chi} \\ \mathbf{0} & \mathbf{I} \end{bmatrix} \begin{bmatrix} \mathbf{U}^{internal} \\ \mathbf{U}^{boundary} \end{bmatrix} = \begin{bmatrix} \mathbf{0} \\ \mathbf{C}^{boundary} \end{bmatrix} \tag{5-25}$$

where $\mathbf{U}^{internal}$ and $\mathbf{U}^{boundary}$ are the matrices of 2D-coordinates of internal and boundary vertices to solve for, $\mathbf{C}^{boundary}$ is a matrix of boundary conditions that contains the positions where the boundary vertices are placed, and $\mathbf{M}^{\mathbf{A}}$ and $\mathbf{M}^{\chi}$ are sparse matrices whose coefficients are given respectively by

$$\mathbf{M}_{ij}^{\mathbf{A}} = \begin{cases} cot(\alpha_{ij}) + cot(\beta_{ij}) & if\ j \in \aleph(i) \\ -\sum_{k \in \aleph(i)} \mathbf{M}_{ik}^{\mathrm{A}} & if\ i = j \\ 0 & otherwise \end{cases} \tag{5-26}$$

$$\mathbf{M}_{ij}^{\chi} = \begin{cases} (cot(\gamma_{ij}) + cot(\delta_{\mathrm{ij}}))/|\mathbf{x}_i - \mathbf{x}_{\mathbf{j}}|^2 & if\ j \in \aleph(i) \\ -\sum_{k \in \aleph(i)} \mathbf{M}_{ik}^{\chi} & if\ i = j \\ 0 & otherwise \end{cases} \tag{5-27}$$

And $\lambda$ and $\mu$ are two arbitrary real constants. $\aleph(i)$ represents the set of neighboring vertices of an internal vertex $i$. For $\alpha_{ij}, \beta_{ij}, \gamma_{ij}, and\ \delta_{ij}$, they are the angles shown in Figure 5-17. $\mathbf{x}_i$ and $\mathbf{x}_j$ are the surface coordinates of vertices. and $\mathbf{u}_i$ and $\mathbf{u}_j$ are the associated plane coordinates of vertices.

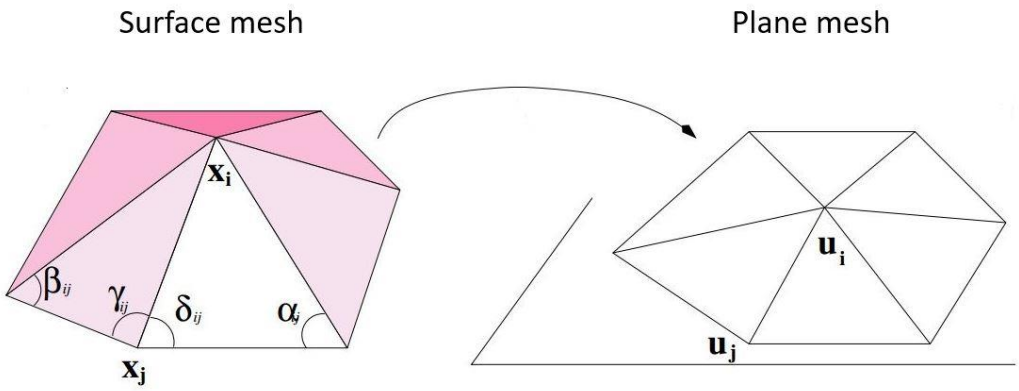


Figure 5-17. The boundary mapping of surface mesh and its associated flattened plane mesh.

For $\lambda = 0$ and $\mu = 1$, it is the authalic (area-preserving) mapping of surface and plane mesh. For $\lambda = 1$ and $\mu = 0$, it is the conformal (angle-preserving) mapping of surface and plane mesh. In [78], Wang *et al.* adopted conformal mapping and projected boundary condition, i.e. the projected 2D coordinates of boundary vertices are the same as original 3D surface mesh, for surface parameterisation. The equation of conformal mapping is

$$\begin{bmatrix} \mathbf{M}^{\mathrm{A}} & \mathbf{0} \\ \mathbf{0} & \mathbf{I} \end{bmatrix} \begin{bmatrix} \mathbf{U}^{internal} \\ \mathbf{U}^{boundary} \end{bmatrix} = \begin{bmatrix} \mathbf{0} \\ \mathbf{C}^{boundary} \end{bmatrix} \tag{5-28}$$

To establish a compact decomposition, Wang et al. [70] further proposed an orthonormal basis achieved using Gram–Schmidt orthonormalisation (GSO), which is explained in Appendix A.1. By the procedures, an orthonormal basis may be formed for any 3D surface. In Figure 5-18 and 5-19, a comparison of geometric monomials and those generated from AGMD can be seen.

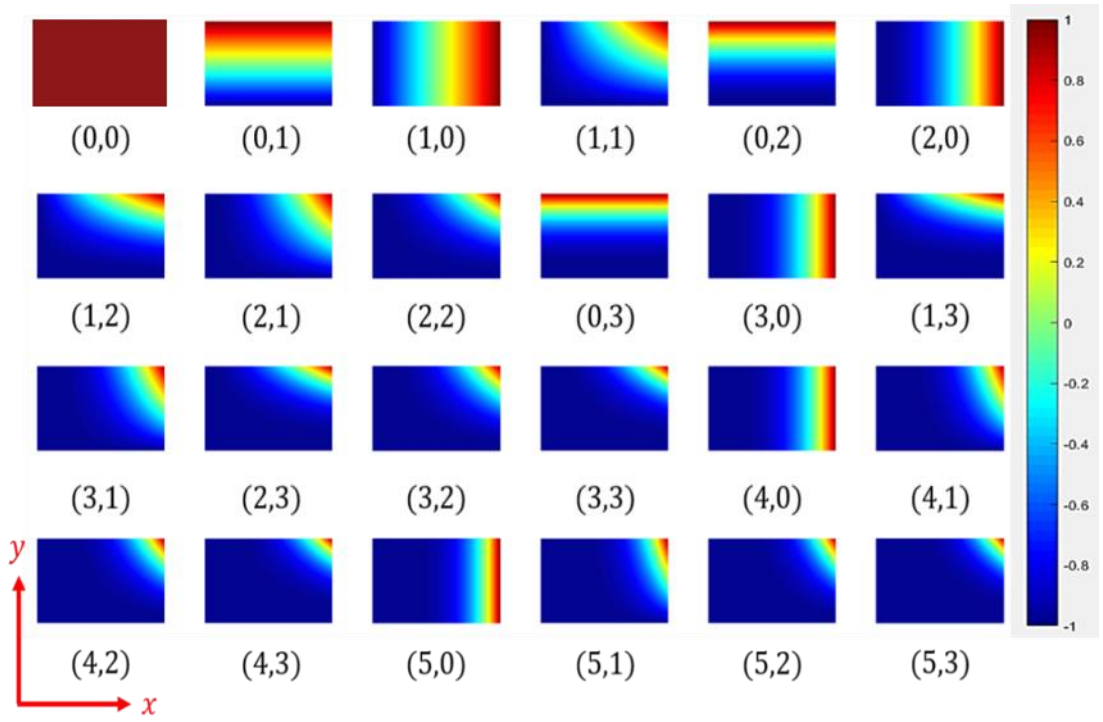


Figure 5-18. First 24 scaled geometric monomials with orders in x and y directions respectively.

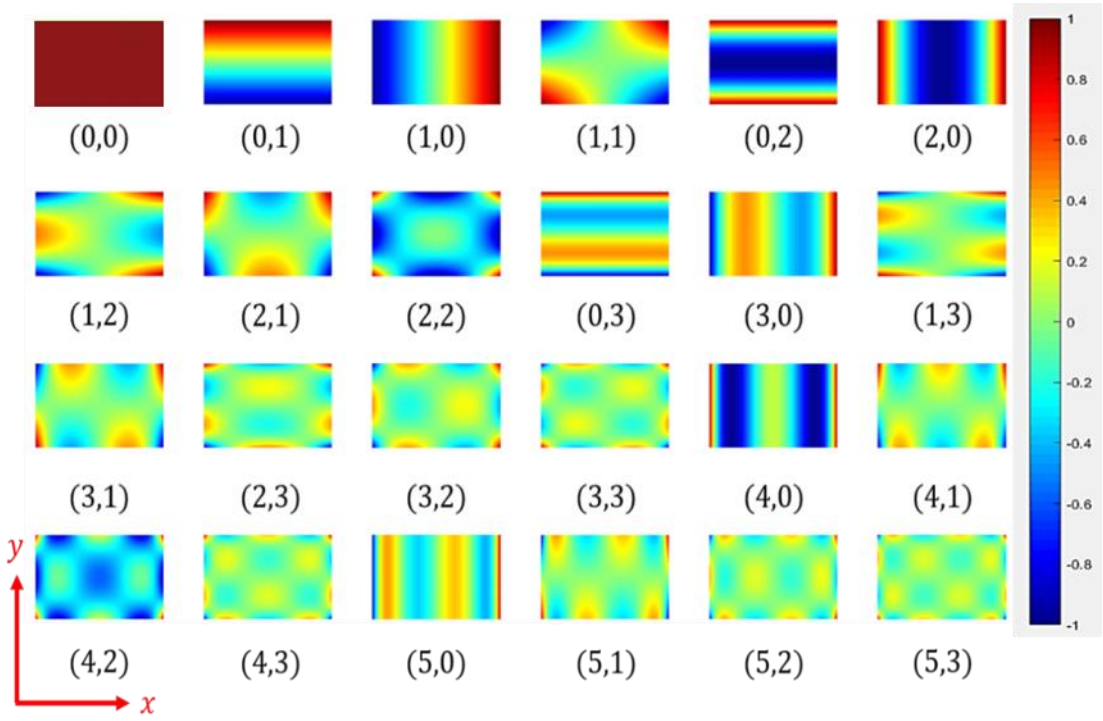


Figure 5-19. First 24 scaled polynomials by AGMD with orders in x and y directions respectively.

### 5.5.2 Example

The example in this section is a car bonnet liner in Figure 5-20, and the parameters of experiments are provided in Table 5-4. Following the procedure explained before, a 3D surface to 2D plane mapping is first formed as shown in Figure 5-21 using conformal mapping.

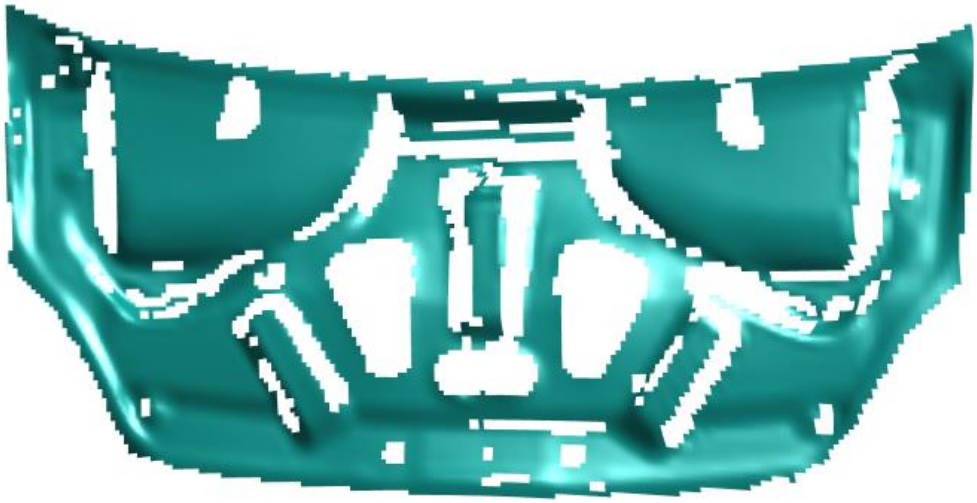

Figure 5-20. Car bonnet liner.

Table 5-4. The parameters of experiment – car bonnet liner.

| | |
|---|---|
| Object | Car bonnet liner |
| Excitation range | 0 ~ 128 Hz |
| Sampling frequency | 300 Hz |
| Number of steps | 7200 |
| Duration | 24 seconds |
| Boundary condition | Free-free |

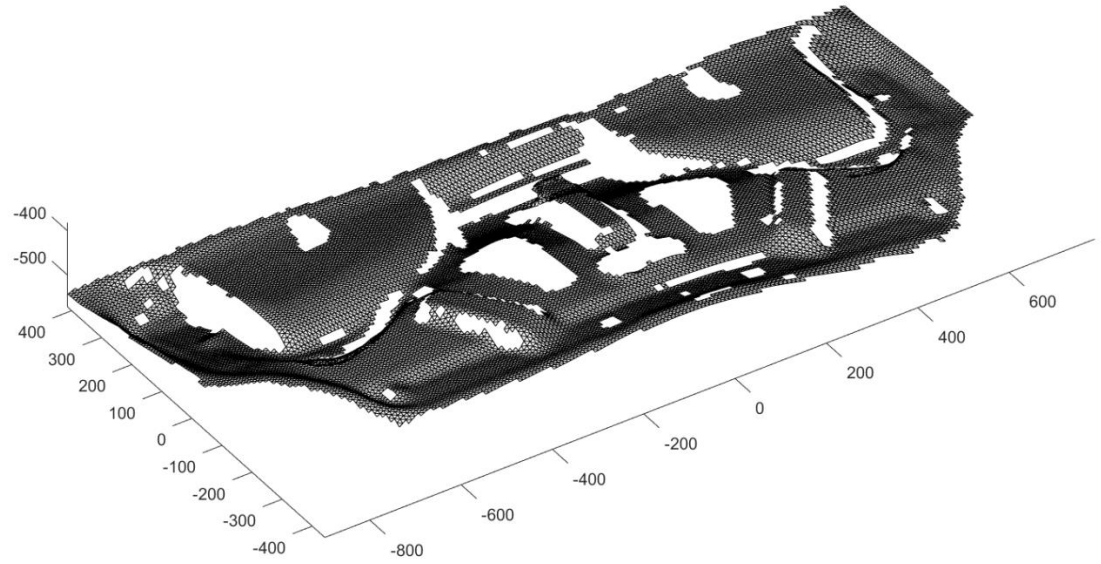


(a) 3D surface triangular mesh

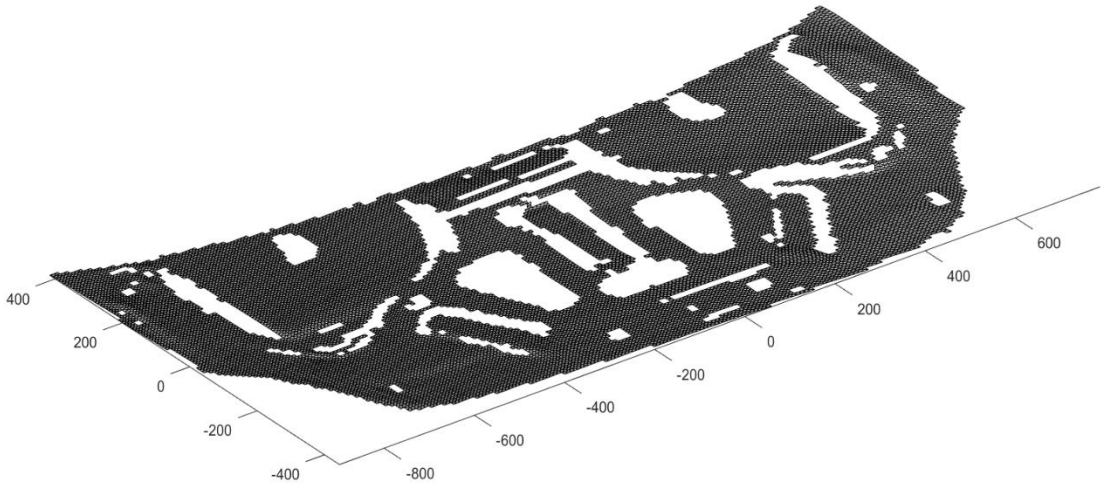


(b) 2D plane triangular mesh

Figure 5-21. A conformal mapping of 3D surface and 2D plane mesh of car bonnet liner.

The orders of AGMD applied for shape decomposition range from 0 to 9 for m and 0 to 7 for n, and there are in total 80 terms. As shown Figure 5-22, the orthogonality between any pair of AGMD is ensured by GSO. The correlation coefficients of reconstructed displacement maps of all instants can be seen in Figure 5-23, and most of them are above 0.99 when all 80 terms are used for reconstruction. In Figure 5-24, the individual displacement map captured at 12 second is shown in (a), and the

reconstructed displacement map is displayed in (b) with the bar chart of descriptors in (c). However, for a reconstructed displacement map at 12 second with a correlation coefficient higher than 0.95, only 7 most significant terms is necessary as shown in Figure 5-25.

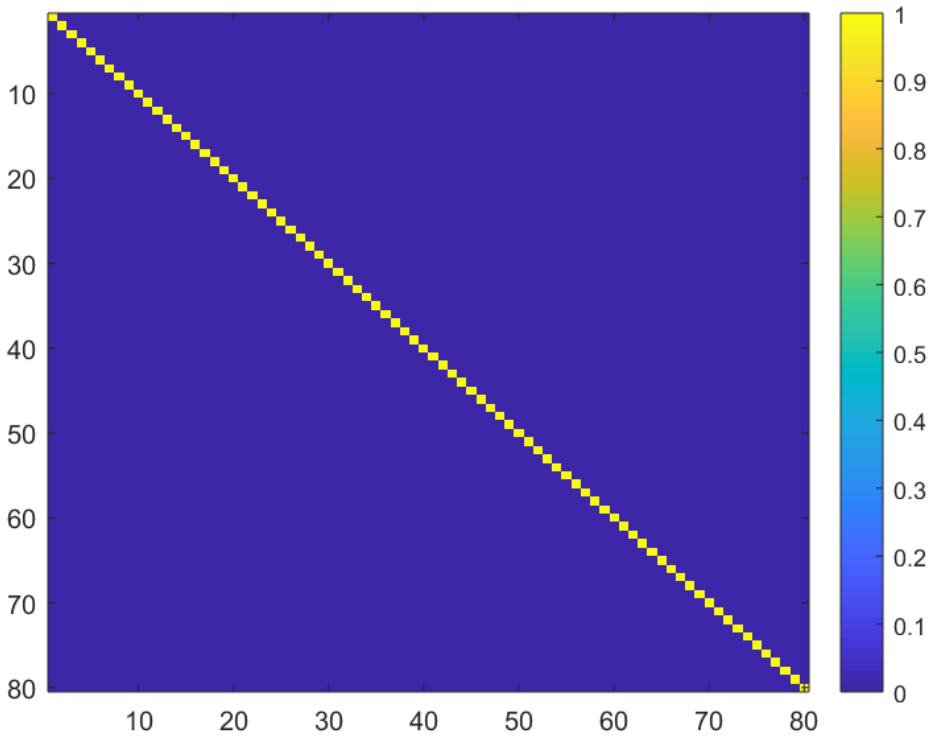


Figure 5-22. The orthogonality map.

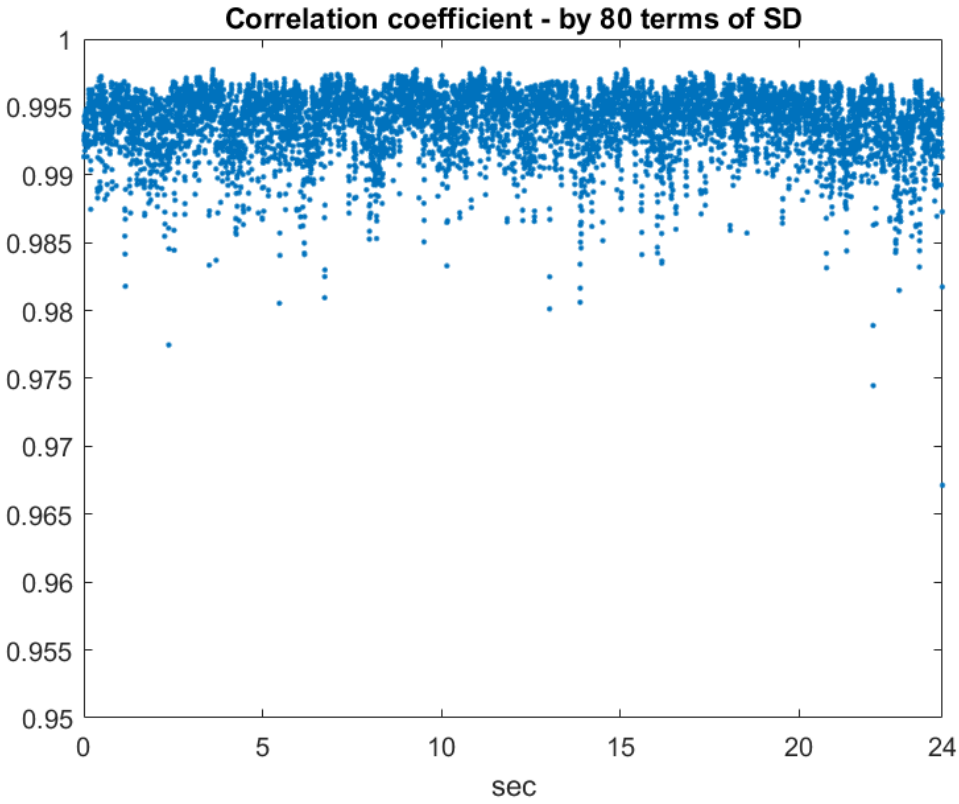


Figure 5-23. Correlation coefficients of reconstructed displacement maps of all instants.

(x axis – time in second, y axis – correlation coefficient).

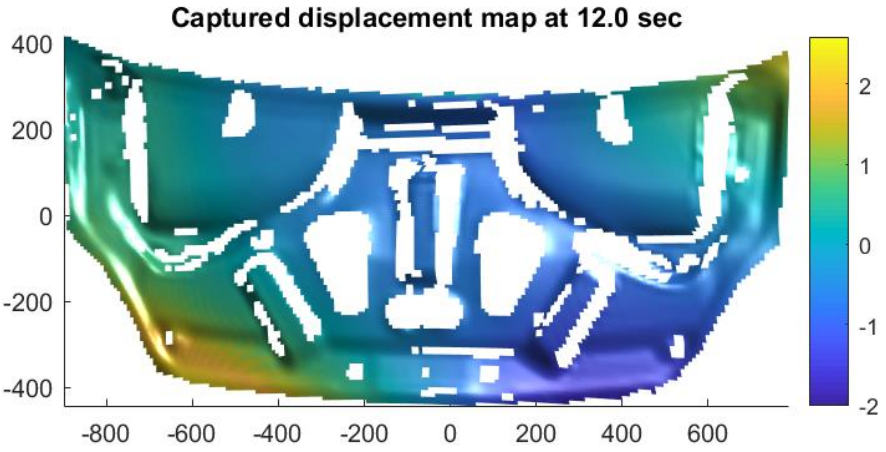


(a) The displacement map captured at 12 seconds.

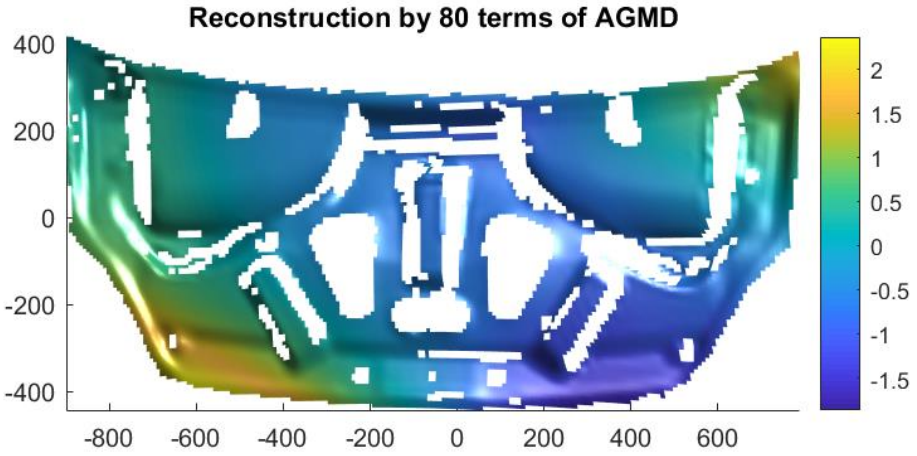


(b) The reconstructed displacement map at 12 seconds.

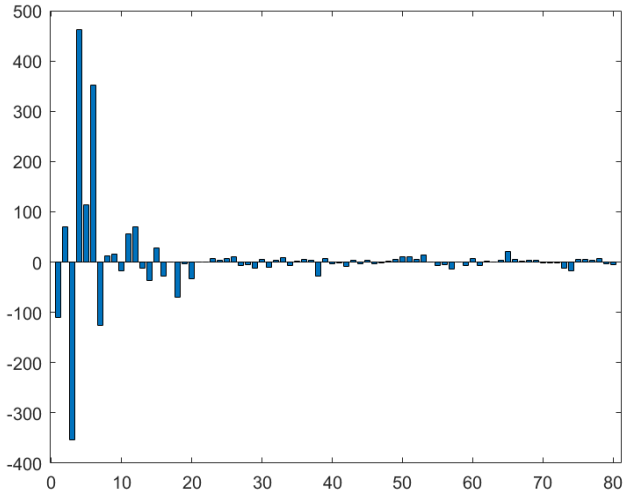


(c) The bar chart of decomposed descriptors of displacement map at 12 seconds.

Figure 5-24. The captured, reconstructed displacement maps and bar chart of descriptors.

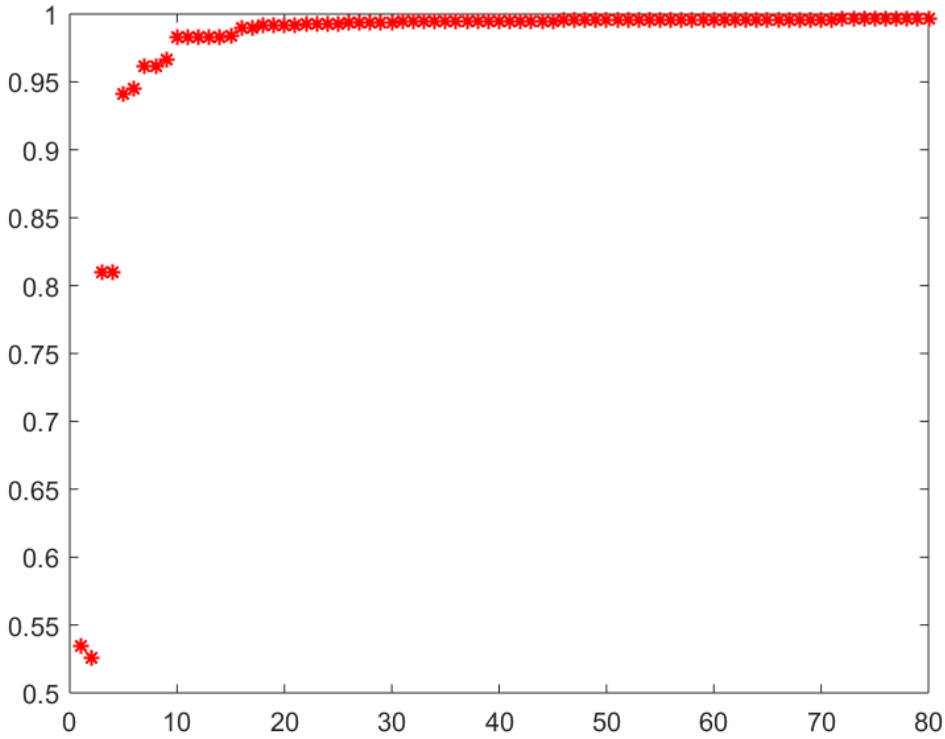


Figure 5-25. The correlation coefficient of reconstructed displacement maps at 12 seconds vs. the number of terms of AGMD.

## 5.6 Closure

From this chapter, the basic ideas of shape decomposition using shape descriptors are explained, and geometric, Tchebichef, Zernike, and adaptive geometric moment descriptors are given in full details. From the examples given, the selection of basis functions and the orders of basis function have a great influence on the compactness and representativeness of shape decomposition. This leads to the development of basis-updating algorithm for shape descriptors in the next chapter. With the developed algorithm, a more representative decomposition can be formed.

# 6 Basis-Updating Algorithm

The extraction of useful information and removal of redundant noise from data has become a major research topic in recent years. Data compression is necessary for all kinds of analysis, and the demand for efficient compression techniques has gained much attention. Digital image correlation is a camera-based measuring system, which has been widely applied in strain analysis because of the convenience of measuring displacement fields by simply selecting a region of interest. Currently, there is interest in applying such methods to engineering structures in dynamics. However, one of the major issues related to the integration of camera-based systems with dynamic measurement is the generation of huge amounts of data, typically extending to many thousands of data points, because of the requirements of high sampling rate, spatial resolution, and long duration of recording. In this section, a new algorithm is presented that addresses the need for efficiency in full-field data processing. By making use of the data itself and combining the concept of sparse representation with Gram-Schmidt orthonormalisation, the number of basis function used to represent the data can be reduced and a concise decomposition established. In both simulated and experimental cases, the compression ratios for data size and number of signals used in operational modal analysis are substantially diminished, thereby demonstrating the effectiveness of the proposed algorithm. A reduced number of new basis functions is determined for the representation of data under the condition that the reconstructed displacement map reproduces the raw measured data to within a chosen threshold on the coefficient of correlation.

### 6.1 Basis learning & sparse representation

Recently, there has been an increasing interest in the research of sparse representation of images. Due to the complexity, such as local details, that an image might possess, some researchers in computer science tend to divide image into patches or blocks, which are relatively simple, for further processing. The definition of basis is a collection of kernels, which are the basic elements for representation. Applying an overcomplete basis $\boldsymbol{\mathcal{H}} \in \mathbb{R}^{n \times K}$ that contains $K$ kernels and $K > n$, which is the dimension of image, images are represented by sparse linear combinations of these kernels. Many examples use sparse representation, including image inpainting [109], image super-resolution [110], image denoising [111], and so on. The focus in this field has concentrated mainly on the study of pursuit algorithms that decompose images with respect to a given basis as formulated in the following equation.

$$\min_{\mathbf{x}} \|\mathbf{x}\|_0 \text{ subject to } \mathbf{y} = \boldsymbol{\mathcal{H}}\mathbf{x} \tag{6-1}$$

where $\|\cdot\|_0$ is defined in Appendix A.2.

This goal can be achieved by either selecting a pre-specified basis or forming an adaptive basis to a set of training images. Both techniques have been demonstrated successfully, and still more new methods are emerging. K-SVD is one of the algorithms that can be used to form an adaptive basis, and the algorithm will be covered in later sections. As mentioned in the beginning of the section, images are first separated into blocks or patches as demonstrated in Figure 6-1 for reducing complexity, and then each block is represented by sparse linear combination of kernels from a basis, such as discrete cosine transform basis in Figure 6-2, which is commonly used for image decomposition.

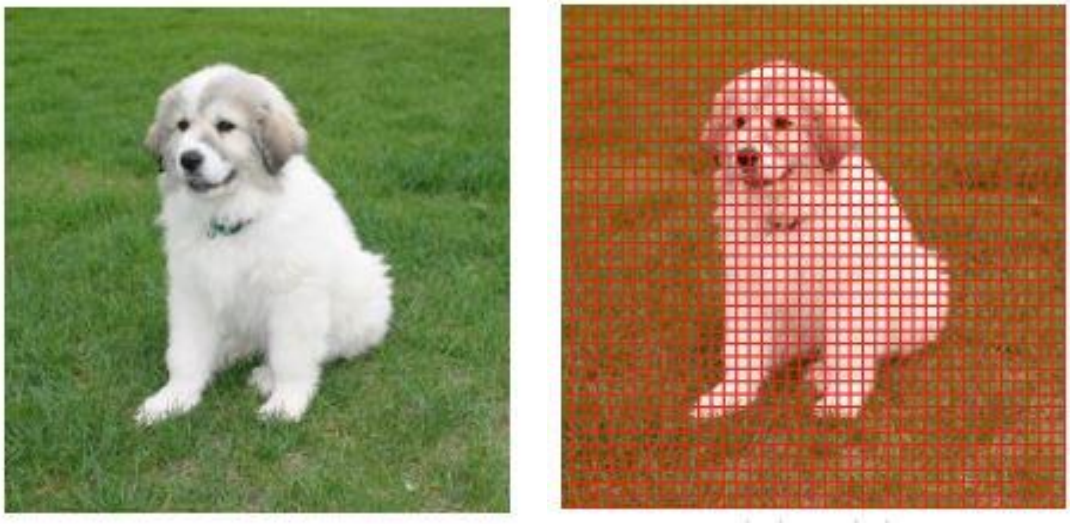

(a) Original image (b) Image blocks

Figure 6-1. Image blocking.

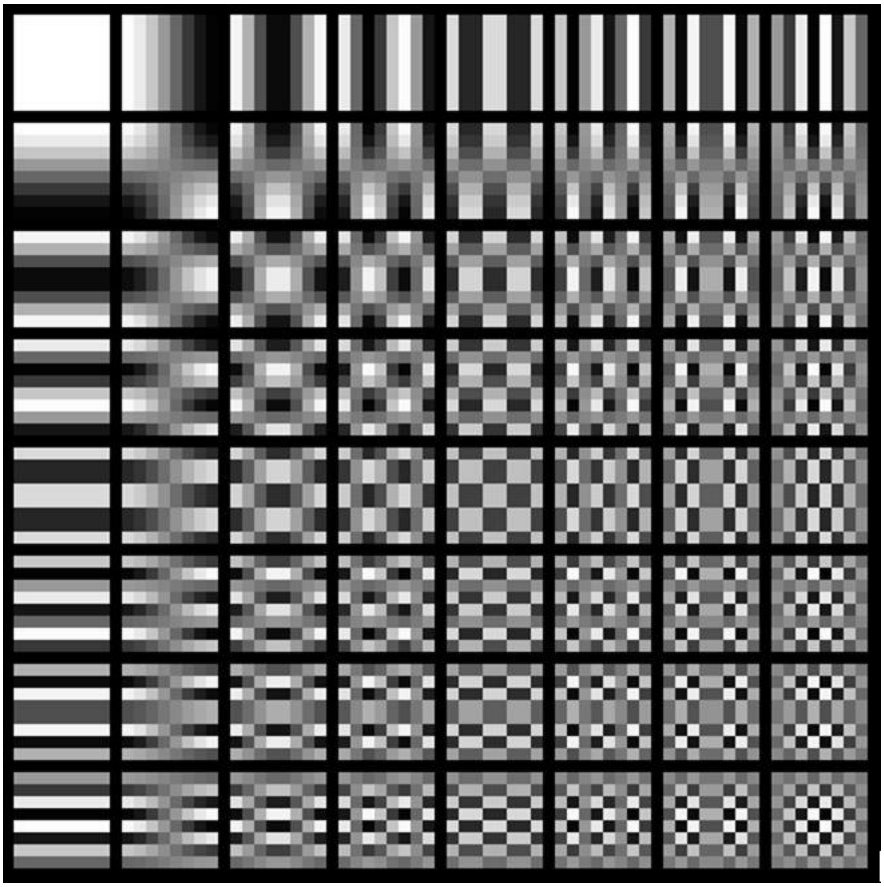

Figure 6-2. Discrete cosine transform basis.

## 6.2 K-means & K-SVD

### 6.2.1 K-means algorithm

K-means clustering is a method of vector quantisation that is popular for cluster analysis in data mining. K-means clustering aims to divide $N$ observations into $K$ clusters, where each observation belongs to the cluster with the nearest mean, serving as a representative of the cluster. A basis $\mathbf{\Pi} = [\mathbf{c}_1, \mathbf{c}_2, \mathbf{c}_3, \dots, \mathbf{c}_K] \in \mathbb{R}^{n \times K}$, where $n$ is the dimension of image block and each column of $\mathbf{\Pi}$ is an kernel. When $\mathbf{\Pi}$ is given, each image block in the set of image blocks $\mathbf{Y}_{imb} = \{\mathbf{y}_i\}_{i=1}^{N} (N \gg K)$, $N$ is the total number of image blocks, is represented by its closest kernel in Euclidean distance as following.

$$\mathbf{y}_i = \mathbf{\Pi}\mathbf{x}_i \tag{6-2}$$

where

$$\mathbf{x}_i = \mathbf{e}_i \tag{6-3}$$

is a unit vector with only the $i^{th}$ element being one.

The K-means algorithm is provided below:

**Objective:** Find the best possible basis to represent

$$\min_{\mathbf{C},\mathbf{X}} \{\|\mathbf{Y}_{imb} - \mathbf{\Pi}\mathbf{X}\|_F^2\} \text{ subject to } \forall i, \mathbf{x}_i \in \mathbf{e}_k \text{ for some } k \tag{6-4}$$

where $\mathbf{Y}_{imb} \in \mathbb{R}^{n \times N}$ is the image block matrix, $\mathbf{\Pi} \in \mathbb{R}^{n \times K}$ is the basis matrix and $\mathbf{X} \in \mathbb{R}^{K \times N}$ is the representation matrix. Frobenius norm $\|\cdot\|_F$ is defined in Appendix

A.2.

**Initialisation:** Set the basis matrix $\mathbf{C}^{(\mathbf{0})}$.

Set $J = 1$

**Repeat until convergence:**

1. Sparse coding stage (C step): partition the training samples $\mathbf{Y}_{\text{imb}}$ into $K$ sets

$$(R_1^{(J-1)}, R_2^{(J-1)}, \dots, R_K^{(J-1)}) \tag{6-5}$$

Each holding the sample indices most similar to the column $\mathbf{c}_k^{(J-1)}$

$$R_1^{(J-1)} = \{i | \forall_{l \neq k}, \left\| \mathbf{y}_i - \mathbf{c}_k^{J-1} \right\|_2 < \left\| \mathbf{y_i} - \mathbf{c}_l^{J-1} \right\|_2 \} \tag{6-6}$$

2. Basis update stage (M step): For each column $k$ in $\mathbf{\Pi}^{(J-1)}$, update it by

$$\mathbf{c}_k^{(J)} = \frac{1}{|R_k|} \sum_{i \in R_k^{(J-1)}} \mathbf{y}_i \tag{6-7}$$

where $|R_k|$ represents the total number of samples in the set $R_k$.

Set $J = J + 1$.

A simple illustration of the procedures can be seen in Figure 6-3, and the C and M steps are the same as described in the algorithm.

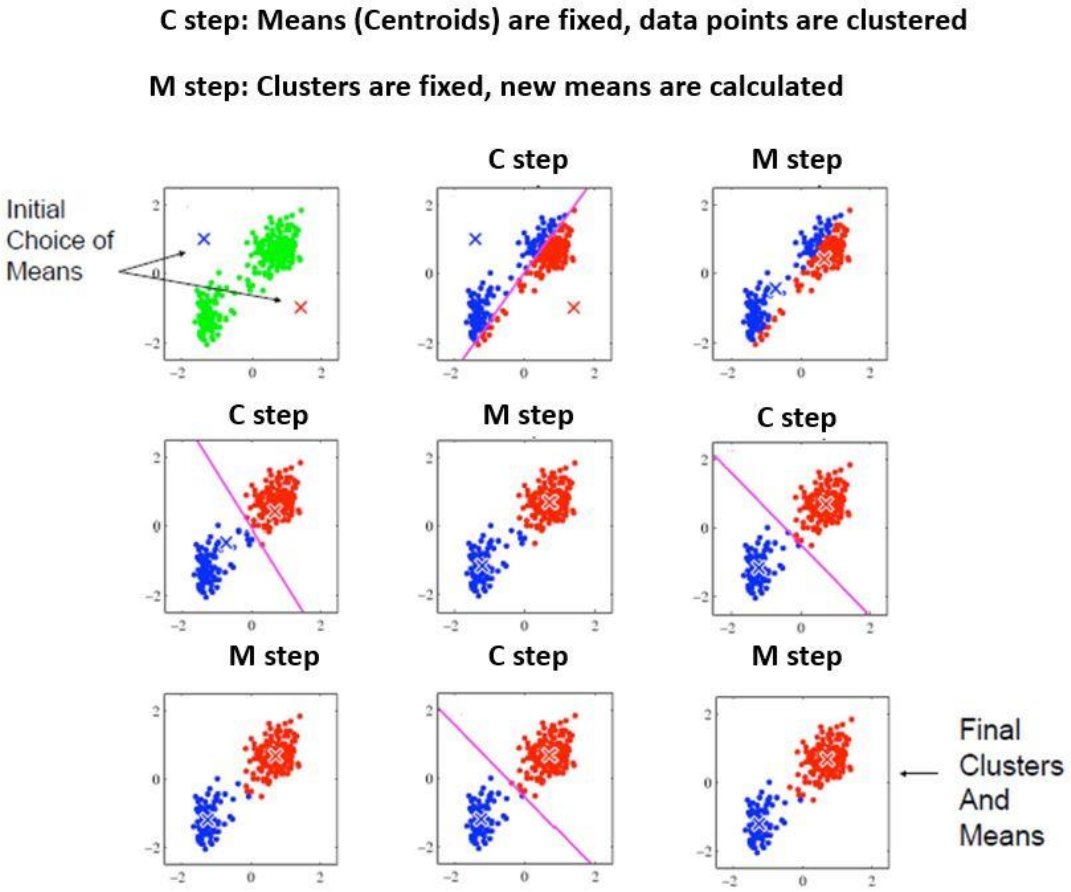


Figure 6-3. A simple illustration of K-means clustering.

### 6.2.2 K-SVD algorithm

K-SVD takes the concept of gradually approaching the best solution from K-means, but different from K-means algorithm, which represents image block as the mean of cluster, K-SVD is used to form a better sparse representation of image block by updating the kernels in a basis sequentially.

The procedure of K-SVD algorithm is listed below:

**Objective:** Find the best basis to represent the image blocks $\mathbf{Y}_{imb} = \{y_i\}_{i=1}^{N}$ as sparse compositions by solving

$$\min_{\mathbf{D},\mathbf{X}}\{\|\mathbf{Y}_{imb}-\boldsymbol{\mathcal{H}}\mathbf{X}\|_F^2\}\ \text{subject to}\ \forall i,\|\mathbf{x}_i\|_0\le T_0 \tag{6-8}$$

where $\mathbf{Y}_{imb}\in\mathbb{R}^{n\times N}$ is the image block matrix, $\boldsymbol{\mathcal{H}}=[\mathbf{d}_1\ \ \cdots\ \ \mathbf{d}_K]\in\mathbb{R}^{n\times K}$ is the basis matrix and $\mathbf{X}=[\mathbf{x}_1\ \ \cdots\ \ \mathbf{x}_N]=\begin{bmatrix}\mathbf{x}_T^1\\ \vdots\\ \mathbf{x}_T^K\end{bmatrix}\in\mathbb{R}^{K\times N}$ is the representation matrix, where $\mathbf{x}_T^j\in\mathbb{R}^{1\times N}$ is row vector. $\boldsymbol{\mathcal{H}}\mathbf{X}=[\mathbf{d}_1\ \ \cdots\ \ \mathbf{d}_K]\begin{bmatrix}\mathbf{x}_T^1\\ \vdots\\ \mathbf{x}_T^K\end{bmatrix}=\sum_{j=1}^{K}\mathbf{d}_j\mathbf{x}_T^j$. Frobenius norm $\|\cdot\|_F$ is defined in appendix A.2.

**Initialisation:** Set the basis matrix $\boldsymbol{\mathcal{H}}^{(0)}$ with $\ell 2$ normalised columns.

Set $J=1$.

**Repeat until convergence:**

1. Sparse coding stage: Use any algorithm to compute the representation vectors $\mathbf{x}_i$ for each image block $\mathbf{y}_i$, by approximating the solution of

$$i=1,2,\dots,N,\ \min_{x_i}\{\|\mathbf{y}_i-\boldsymbol{\mathcal{H}}\mathbf{x}_i\|_2^2\}\ \text{subject to}\ \|\mathbf{x}_i\|_0\le T_0 \tag{6-9}$$

2. Basis update stage: For each column $z=1,2,\dots,K$ in $\boldsymbol{\mathcal{H}}^{(J-1)}$, update it by

(1) Define $\omega_z$ as the set of indices pointing to image blocks that use the kernel $\mathbf{d}_z$, $\omega_z=\{i|1\le i\le N,\mathbf{x}_T^z(i)\neq 0\}$ and $\boldsymbol{\Omega}_z$ as a matrix of size $N\times|\omega_z|$, with ones on $(\omega_z(i),i))th$ entries and zeros elsewhere.

(2) Compute the overall representation error matrix $\mathbf{E}_z$ by

$$\mathbf{E}_z = \mathbf{Y} - \sum_{j \neq z} \mathbf{d}_j \mathbf{x}_T^j \tag{6-10}$$

(3) Restrict $\mathbf{E}_z$ by choosing only the columns corresponding to $\omega_z$, and obtain

$$\mathbf{E}_z^R = \mathbf{E}_z \mathbf{\Omega}_z, \ \mathbf{x}_R^z = \mathbf{x}_T^z \mathbf{\Omega}_z \tag{6-11}$$

(4) Apply SVD decomposition on $\mathbf{E}_z^R$

$$\mathbf{E}_z^{\mathrm{R}} = \mathbf{U} \Sigma \mathbf{V}^{\mathrm{T}} \tag{6-12}$$

(5) Update $\mathbf{d}_z$ to be the first column of $\mathbf{U}$. Update the coefficient vector $\mathbf{x}_R^z$ to be the first column of $\mathbf{V}$ multiplied by $\mathbf{\Sigma}(1,1)$.

Set $J = J + 1$.

### 6.3 Basis-updating algorithm

The motivation of the research is that AGMD as proposed by Wang et al. [78] might not provide the best decomposition of a full-field image, because the data are not considered in the generation of the basis. In this section, an updating algorithm for the basis, which is utilised to decompose huge amounts of raw data, is proposed. Within a finite number of iterations, a more succinct or representative description of data is generated, i.e. a fewer number of SD terms than the number of AGMD terms containing the same amount or more of information. As can be seen from the procedure described in chapter 5, the formulation of the AGMD is done completely independently of the

displacement map that it seeks to reproduce. Hence, by taking inspiration from the K-SVD algorithm as proposed by Aharon et al. in [112] and the utilisation of GSO, a new algorithm for basis-updating [113] for DIC displacement maps is provided herein.

The procedure of the algorithm is described below:

Given an image matrix $\mathbf{Y}_{im} = [\mathbf{y}_1, \mathbf{y}_2, \dots, \mathbf{y}_q] \in \mathbb{R}^{p \times q}$, where $p$ is the dimension of vectorised image and $q$ is the total number of images

**Initialisation:** Generate an initial basis matrix $\mathbf{N} = [\boldsymbol{a}_1 \quad \cdots \quad \boldsymbol{a}_m] \in \mathbb{R}^{p \times m}$, where $m \leq p$, and the corresponding coefficient matrix is $\mathbf{S} = [\mathbf{s}_1 \quad \cdots \quad \mathbf{s}_q] \in \mathbb{R}^{m \times q}$ and set a tolerance $\epsilon$ on the representation error.

1. Sequentially update each column $k = 1, 2, \dots, m$ in $\mathbf{N}$ with image matrix $\mathbf{Y}_{im}$

(1) Calculate the complement matrix $\mathbf{Y}_k \in \mathbb{R}^{p \times q}$,

$$\mathbf{Y}_k = \mathbf{Y}_{im} - \mathbf{N}_k \mathbf{S} \tag{6-13}$$

where $\mathbf{N}_k$ is the basis matrix with $\boldsymbol{a}_k$ set to be a zero vector, i.e. removed from the basis.

(2) Apply singular value decomposition on $\mathbf{Y}_k$,

$$\mathbf{Y}_k = \mathbf{U}\boldsymbol{\Sigma}\mathbf{V}^T \tag{6-14}$$

(3) Update $\boldsymbol{a}_k$ using the first column of $\mathbf{U}$

2. Upon completion, when all the kernels have been updated, Gram-Schmidt orthonormalisation is applied and any repeated kernels are removed. A new set of coefficients are then produced by projecting the images onto the new basis functions.

3. Iteration precedes until the difference between the data and its SD representation falls below the chosen threshold

$$\|\mathbf{Y}_{im} - \mathbf{NS}\|_F \leq \epsilon \tag{6-15}$$

At each iteration any SD coefficients and kernels deemed to be insignificant are removed. Finally, a set of kernels and SDs based on the data and generally much smaller in dimension than the initial one is produced. Frobenius norm $\|\cdot\|_F$ is defined in Appendix A.2.

### 6.4 Analysis procedure

The analysis procedure is illustrated in the flowchart of Figure 6-4, with steps explained as follows. In the first step, a collection of measured displacement maps serves as the target of the analysis. These maps are then decomposed into several SDs and kernel functions, generated by the AGMD method and further updated by the algorithm described in previous section. After decomposition, the SD signals are used as input for OMA in the identification of modal properties. Since the analysis is implemented in SD domain, another step of conversion is necessary for the presentation of mode shapes in spatial domain. This is done by linear combination of mode shapes of SDs from step 2 and kernel functions from step 1.

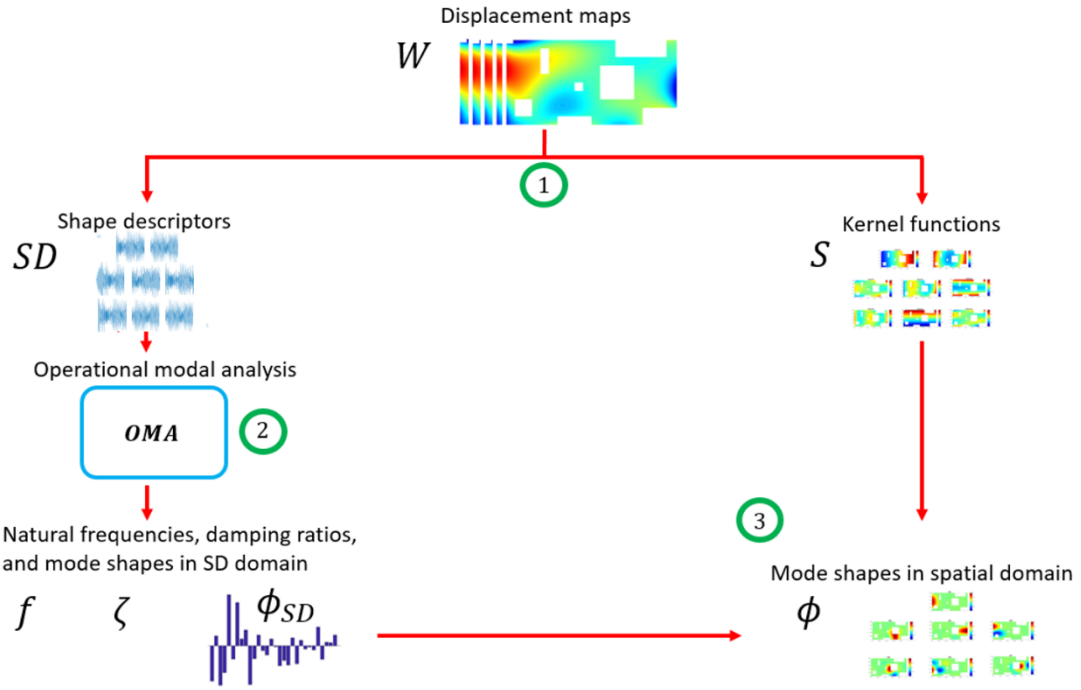


Figure 6-4. Flow chart of analysis.

## 6.5 Case Studies

For the validation of the proposed algorithm, both simulated and experimental data are analysed.

### 6.5.1 Simulated data

Simulated data is produced by using the ABAQUS finite element (FE) code. The FE mesh of an irregular plate-like structure with fully-fixed and pinned boundary conditions are shown in Figure 6-5. Full details of the FE model and analysis are provided in Table 6-1 and the first seven modal frequencies are given in Table 6-2.

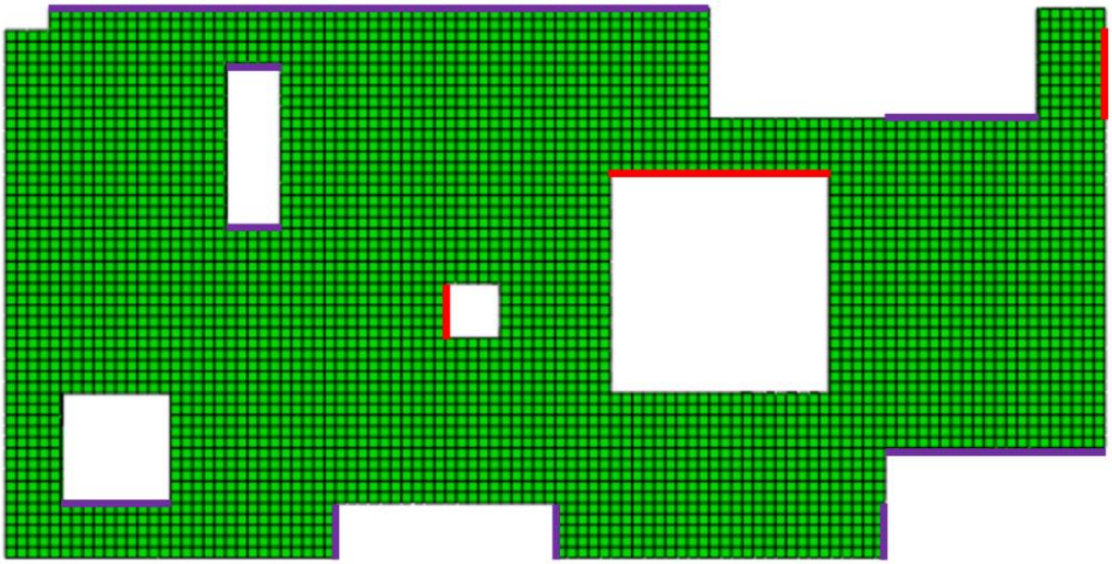

Figure 6-5. FE model: Purple line – fixed in 6 degrees of freedom; Red line – pinned in 3 degrees of freedom.

Table 6-1. The parameters of FE simulation.

| | |
|---|---|
| Material | A36 Steel: Young's Modulus: 200GPa<br>Poisson's ratio: 0.26<br>Density: 7850 Kg/$m^3$ |
| Dimension | Width: 1 m Height: 0.5 m Thickness: 0.01 m |
| Section | Solid, Homogeneous |
| Element size | 0.01 m by 0.01 m by 0.01 m |
| Boundary condition | As shown in Figure 6-5 |
| Excitation | Excitation: Zero-mean Gaussian white noise (0 ~ 100 Hz) |
| Sampling frequency | 1000 Hz |
| Number of steps | 4000 (4 seconds) |
| Output | 4044 out-of-plane displacement recordings |

Table 6-2**.** Natural frequencies. (Hz)

| Mode | 1 | 2 | 3 | 4 | 5 | 6 | 7 |
|---|---|---|---|---|---|---|---|
| FE | 35.783 | 54.863 | 63.342 | 71.012 | 82.858 | 89.328 | 94.546 |

### 6.5.2 Experimental PCB circuit board

The circuit board is a real experimental example of DIC data from an industrial company, and only the displacement maps, not the original images, are received. It is partly obscured by other parts so that the camera has only two separate parts of the circuit board in view, as shown in Figure 6-6. The boundary condition of the circuit board was not known by the company, who were able to provide only the following information. The structure was excited by a random excitation with a frequency range from 200 to 1000 Hz, and the sampling frequency of the high-speed cameras was set at 2000 Hz. The total duration of measurement was 1.579 seconds, and hence the resulting number of steps was 3158.

(a) part 1

(b) part 2

Figure 6-6**.** Circuit board parts 1 (a) and 2 (b).

## 6.6 Result and discussion

In this section, the results of OMA with AGMD and updated kernel functions in simulated and experimental cases are provided, compared, and discussed.

### 6.6.1 Simulated data

The proposed algorithm in section 6-3 allows for a threshold to be set on the coefficient of correlation between the original data and its representation by using the updated basis. In the present example, the number of modes within the excitation range is 7, thus at least 7 kernel functions are necessary for a successful reconstruction of mode shapes. Figure 6-7 shows that if the threshold is too low, then over-compression can happen, i.e. some of the mode shapes might not be successfully identified and reconstructed. In Figure 6-8, the updated kernel functions from the basis-updating method are listed, and the mode shapes from the FE model are provided in Figure 6-9. Figure 6-10 shows the tables of modal assurance criteria (MAC) values between the original data and either 30 AGMD terms, 7 AGMD terms and 7 terms of the updated basis. The three sets of the figure correspond to 3 different OMA methods ((a)~(c): SSI-COV/ (d)~(f): P-LSCF/ (g)~(i): Bayesian). The MAC maps of mode shapes identified from each OMA method with updated kernel functions are better than those that include the 30 most significant terms AGMD kernels. Also, with the same number of kernel functions, some of the mode shapes were not identifiable using AGMDs, but the proposed method succeeded in the identification by preserving the important features of the displacement maps. Figure 6-11 shows the effect of over-compression, when the number of kernel functions was less than the number of modes, so that the MAC matrix could not be diagonalised. For comparison, the compression ratios in terms of data size and number of shape functions are provided in Table 6-3, and as can be seen, both

compression-ratio measures are significantly improved by the proposed method.

Table 6-3**:** Compression ratios for simulated data.

| | Data size (bytes) | Compression ratio | Data number | Compression ratio |
|---|---|---|---|---|
| Original | 115 MB | 1 | 4044 data points | 1 |
| AGMD | 1.76 MB | 65.34 | 30 SD terms | 134.80 |
| proposed method | 465 KB | 253.25 | 7 SD terms | 577.71 |

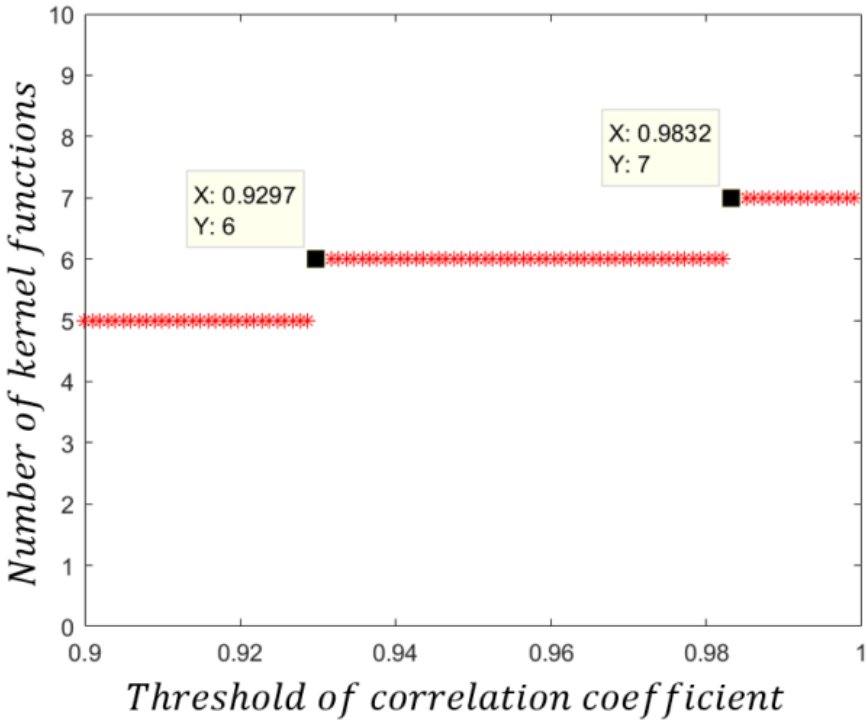


Figure 6-7**.** Number of kernel functions vs. threshold of correlation coefficient.

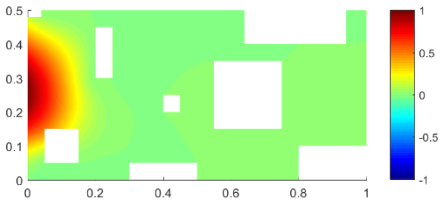

(a) First updated kernel function

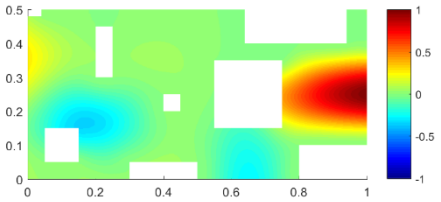

(b) Second updated kernel function

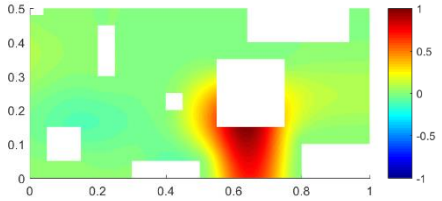

(c) Third updated kernel function

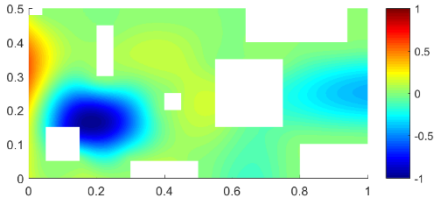

(d) Fourth updated kernel function

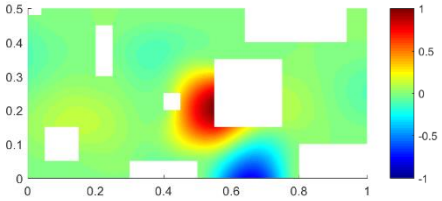

(e) Fifth updated kernel function

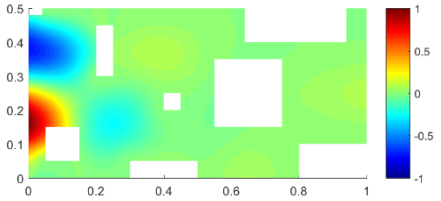

(f) Sixth updated kernel function

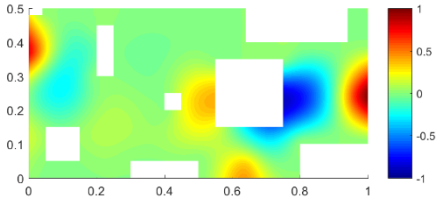

(g) Seventh updated kernel function

Figure 6-8. Updated kernel functions.

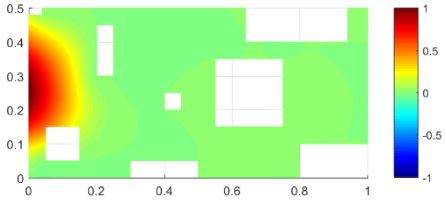

(a) First mode shape

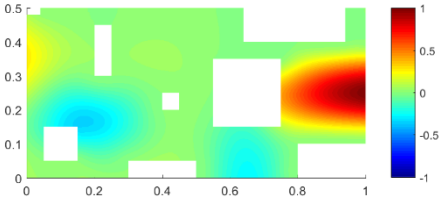

(b) Second mode shape

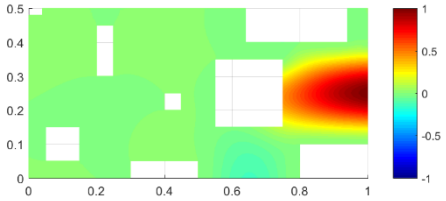

(c) Third mode shape

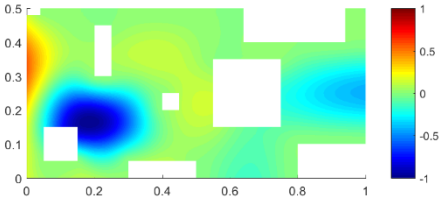

(d) Fourth mode shape

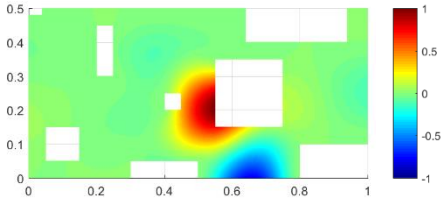

(e) Fifth mode shape

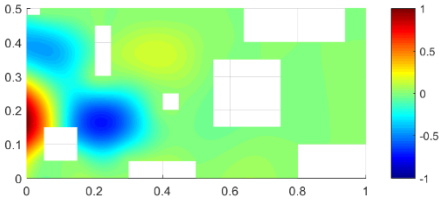

(f) Sixth mode shape

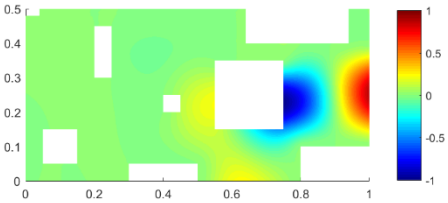

(g) Seventh mode shape

Figure 6-9. Simulated mode shapes from FE model.

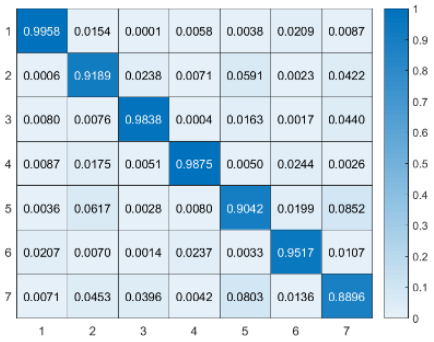


(a) 30 terms of AGMD

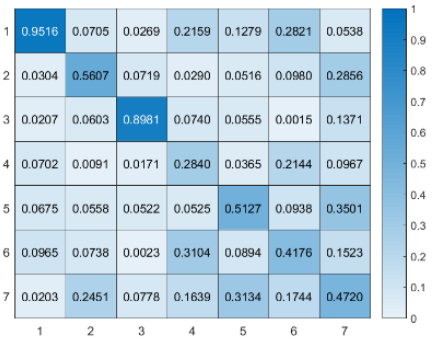


(b) 7 terms of AGMD

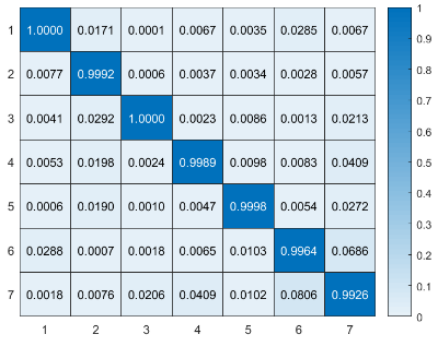


(c) Updated basis of 7 terms

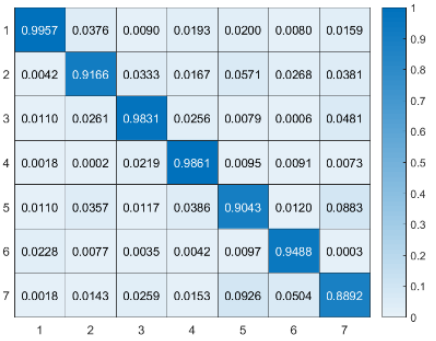


(d) 30 terms of AGMD

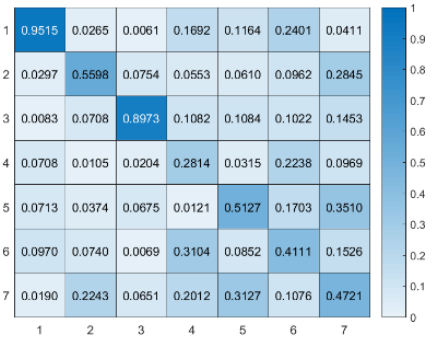


(e) 7 terms of AGMD

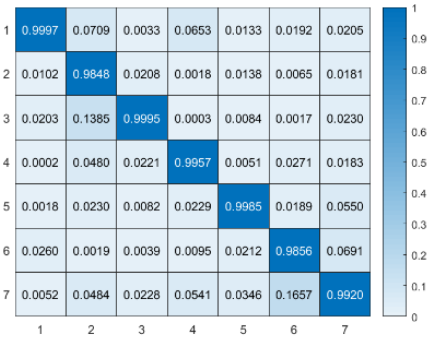


(f) Updated basis of 7 terms

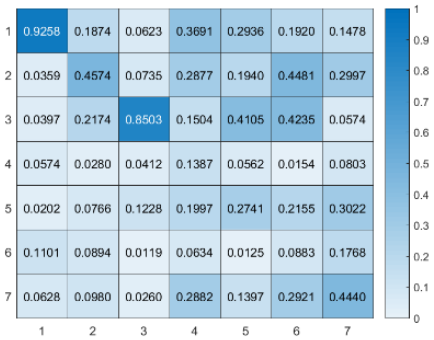


(g) 30 terms of AGMD

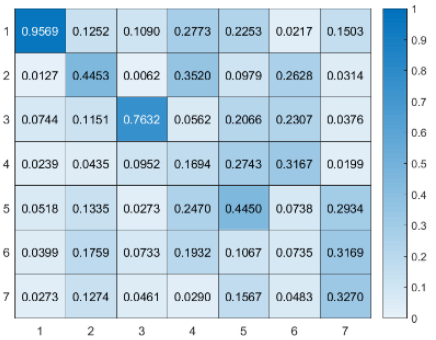


(h) 7 terms of AGMD


(i) Updated basis of 7 terms

Figure 6-10**.** MAC maps for AGMDs and updated SDs. (a)~(c): SSI-COV. (d)~(f): PLSCF. (g)~(i): Bayesian method (x axis - SD, y axis - FE).

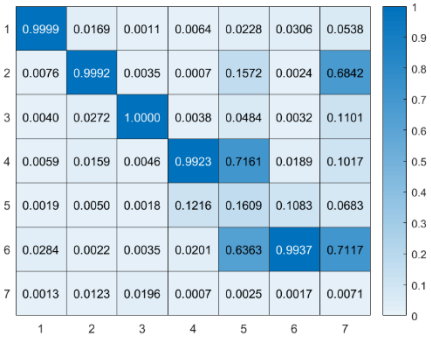


(a) Updated basis of 5 terms by SSI-COV

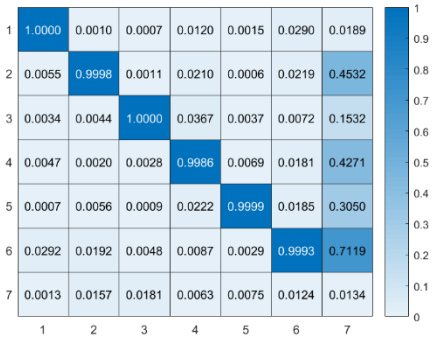


(b) Updated basis of 6 terms by SSI-COV

Figure 6-11**.** MAC maps from over-compressed bases. (x axis – SD, y axis - FE,)

### 6.6.2 Printed circuit board (PCB)

For the experimental case, the same procedures are applied to determine the modal properties, and the data from both parts of the circuit board are combined in the analysis, with the resulting identified natural frequencies provided in Table 6-4.

Table 6-4. Identified natural frequencies of circuit board by SSI-COV. (Hz)

| Mode | 1 | 2 |
|---|---|---|
| 80 terms of AGMD | 534.886 | 779.037 |
| Updated basis of 8 terms | 535.297 | 779.039 |

Just two modes were identified in the excitation range, but because of the effects of noise and out-of-range modes the number of SDs required to reproduce the data was found to be greater than 2. The compression ratios of both parts 1 and 2 of the circuit board are presented in Tables 6-5 and 6-6, where the advantages of the proposed method are apparent. It is seen in Figure 6-12 that eight updated SDs are necessary to achieve a correlation coefficient of 0.99, and the updated kernel functions of circuit board part 1 and 2 are provided in Figure 6-13 and 6-14. Figure 6-15 shows virtually no difference between 80 AGMD terms and 8 updated SD for the first mode, whereas slight differences can be seen in the second mode. However, by viewing Figure 6-16, which shows the deflected shapes of the second part of the circuit board when excited by a harmonic excitation at 537.3 Hz and 779.3 Hz respectively, it becomes apparent that the second mode shape from the updated basis is the correct one.

Table 6-5. Compression ratios of circuit board part 1.

| | Data size (bytes) | Compression ratio | Data number | Compression ratio |
|---|---|---|---|---|
| Original | 119 MB | 1 | 5300 data points | 1 |
| AGMD | 5.14 MB | 23.15 | 80 SD terms | 66.25 |
| proposed method | 745 KB | 163.57 | 8 SD terms | 662.5 |

Table 6-6. Compression ratios of circuit board part 2.

| | Data size (bytes) | Compression ratio | Data number | Compression ratio |
|---|---|---|---|---|
| Original | 51.8 MB | 1 | 2791 data points | 1 |
| AGMD | 3.58 MB | 14.47 | 80 SD terms | 34.89 |
| proposed method | 480 KB | 110.51 | 8 SD terms | 348.88 |

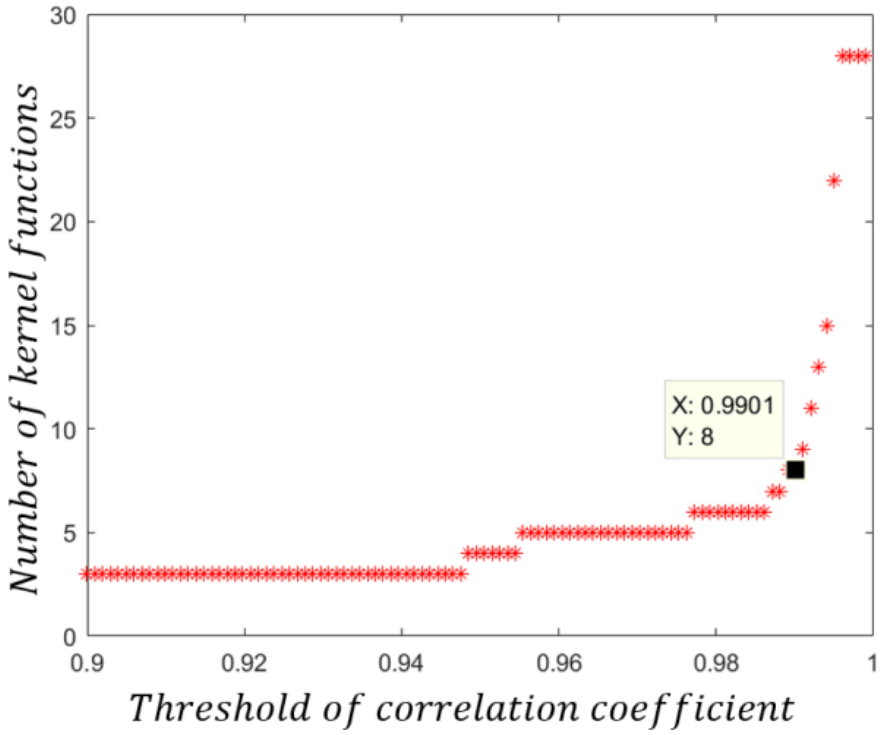


Figure 6-12. Number of kernel functions vs. threshold of correlation coefficient.

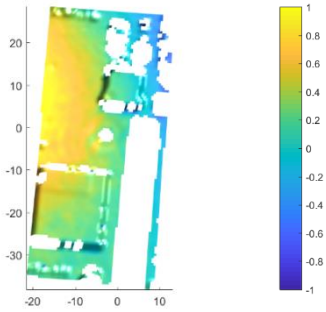

(a) First updated kernel function

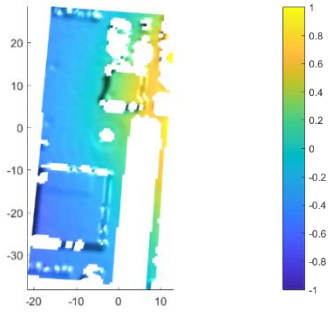

(b) Second updated kernel function

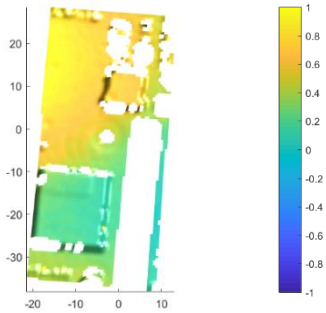

(c) Third updated kernel function

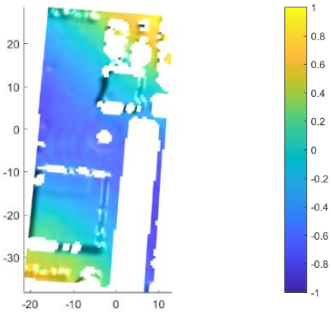

(d) Fourth updated kernel function

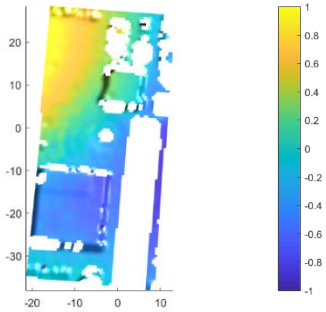

(e) Fifth updated kernel function

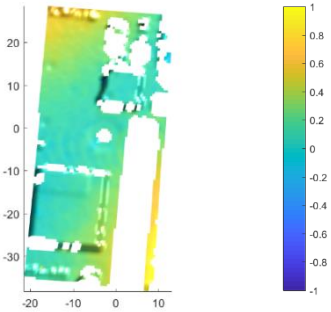

(f) Sixth updated kernel function

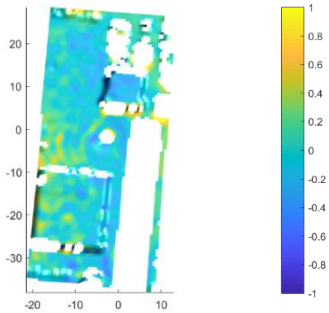

(g) Seventh updated kernel function

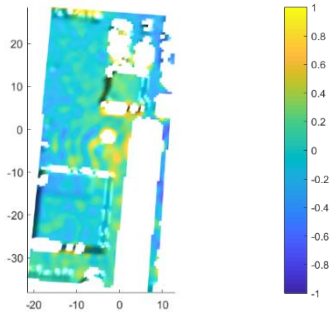

(h) Eighth updated kernel function

Figure 6-13. Updated kernel functions of circuit board part 1.

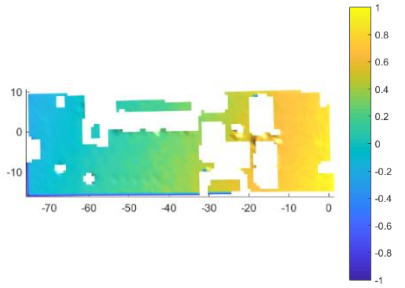

(a) First updated kernel function

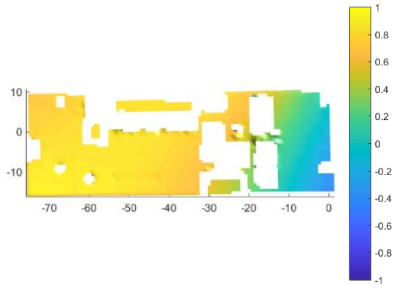

(b) Second updated kernel function

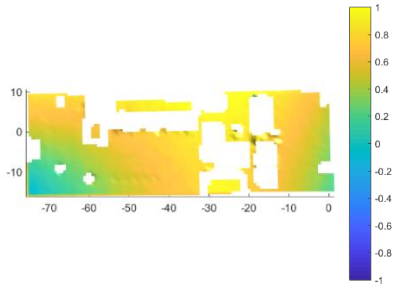

(c) Third updated kernel function

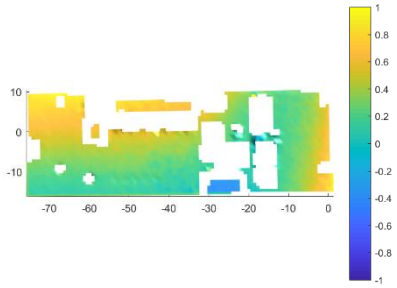

(d) Fourth updated kernel function

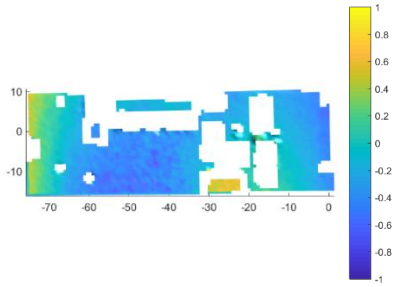

(e) Fifth updated kernel function

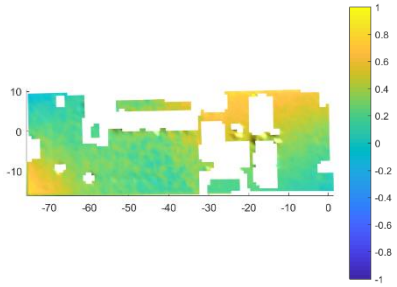

(f) Sixth updated kernel function

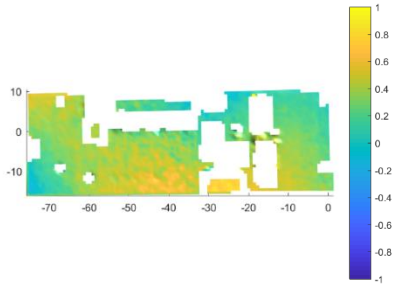

(g) Seventh updated kernel function

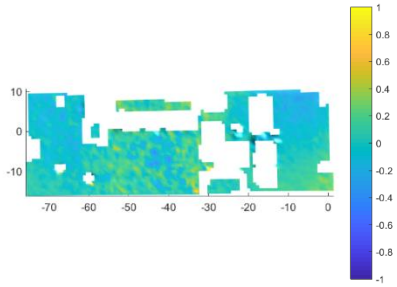

(h) Eighth updated kernel function

Figure 6-14. Updated kernel functions of circuit board part 2.

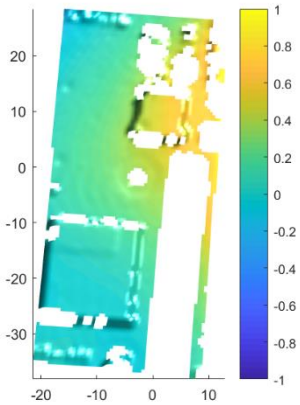


(a) First mode shape of circuit board part 1: 80 terms of AGMD by SSI-COV

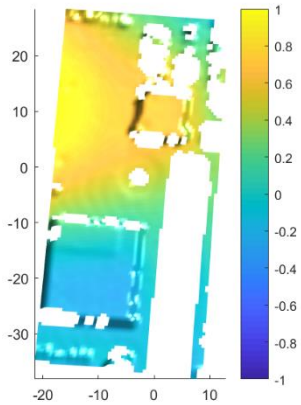


(b) Second mode shape of circuit board part 1: 80 terms of AGMD by SSI-COV

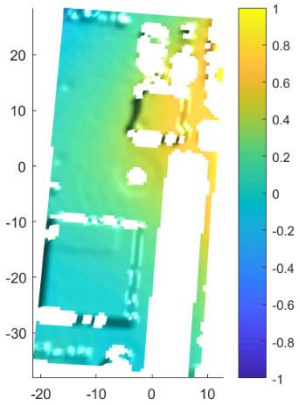


(c) First mode shape of circuit board part 1: updated basis of 8 terms by SSI-COV

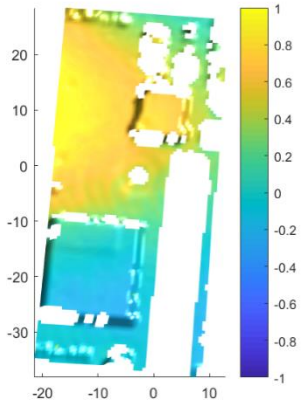


(d) Second mode shape of circuit board part 1: updated basis of 8 terms by SSI-COV

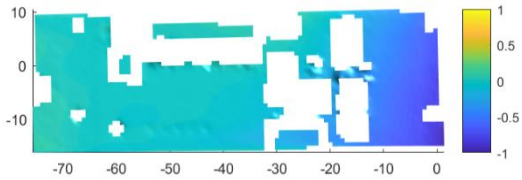


(e) First mode shape of circuit board part 2: 80 terms of AGMD by SSI-COV

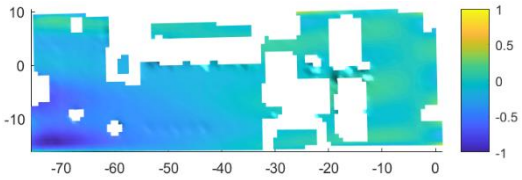


(f) Second mode shape of circuit board part 2: 80 terms of AGMD by SSI-COV

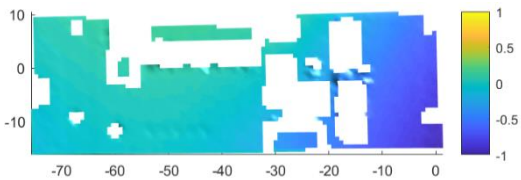


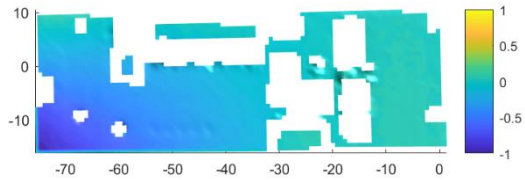

(g) First mode shape of circuit board part 2: updated basis of 8 terms by SSI-COV

(h) Second mode shape of circuit board part 2: updated basis of 8 terms by SSI-COV

Figure 6-15. The identified scaled mode shapes of both circuit board parts. (dimensions in mm)

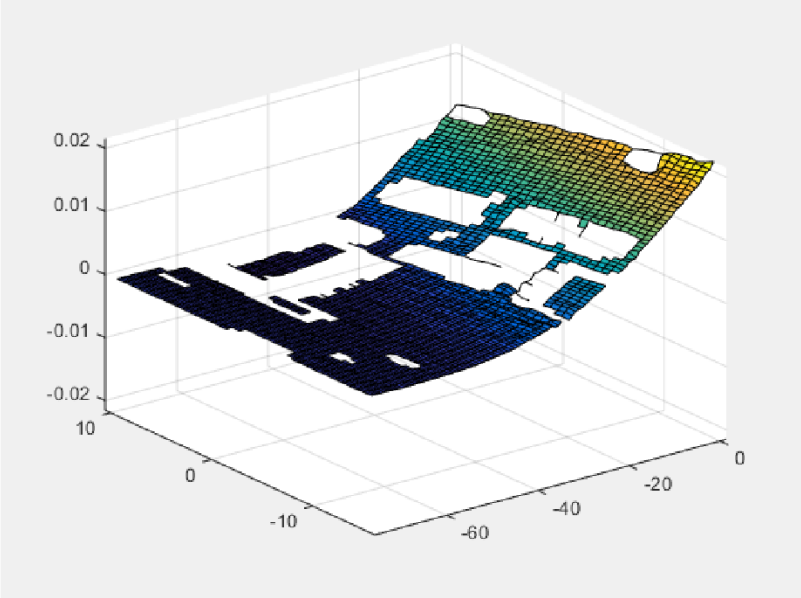


(a) The deflected shape of circuit board part 2 by harmonic excitation at 537.3 Hz.

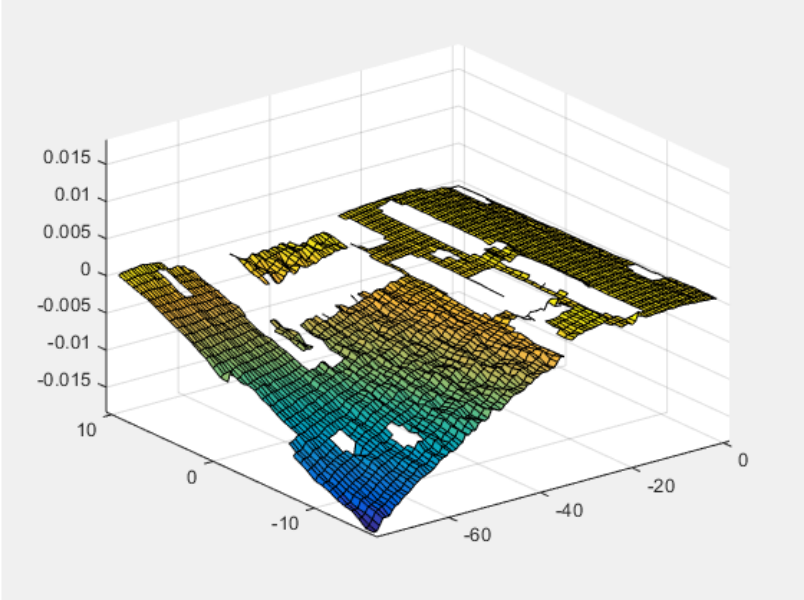


(b) The deflected shape of circuit board part 2 by harmonic excitation at 779.3 Hz.

Figure 6-16. The deflected shapes of circuit board part 2 by harmonic excitation at 537.3 Hz and 779.3 Hz, respectively.

## 6.7 Closure

A new algorithm has been presented for the compression of full-field measurements from DIC. It requires an initial basis as a starting point in an iterative procedure. Probably the most suitable initial basis is that provided by the AGMD, which is ideal for engineering structures and components, because it is capable of providing an orthogonal basis over an arbitrarily shaped domain. The working of the algorithm depends upon the data itself and it is this feature that enables it to achieve such significant improvements in compression ratio over classical orthogonal kernels (including the AGMD). It is particularly useful that a threshold may be placed on the correlation with the raw measured data to ensure that important features of DIC displacement maps are not lost by truncation. Validation of the algorithm has been carried out using both simulated datasets and physical measurement from a real industrial DIC investigation.

# 7 Compressed Sensing

Optically-acquired data, typically from DIC-based displacement measurement, is increasingly being used in the area of structural dynamics, particularly modal testing and damage identification. One of the problems with such data is its extremely large size. Single images regularly extend to tens or even hundreds of thousands of data points and many thousands of images may be required for a vibration test. Such data must be stored and transmitted efficiently for later remote reconstruction and analysis, typically operational modal analysis. It is this requirement that is addressed in the research presented in this chapter. This research builds upon previous work whereby digitised optical data was projected onto an orthogonal basis with coefficients (SDs) of either greater or lesser significance; those deemed to be insignificant, according to a chosen threshold being removed. Data reduction by a combination of SD decomposition and CS is applied to an industrial printed circuit board and reconstructed for OMA by $\ell_1$ optimisation.

## 7.1 Compressed sensing theory

CS is applicable to both signals (in time) and images (in 2-D or 3-D space) but is perhaps easiest explained in terms of an N-vector of time-varying signals. Conventional signal processing using the Nyquist-Shannon sampling theory requires that the sampling rate shall be "uniformly" at least twice the highest frequency present in the signal. CS [10, 83] overturns this theory using principles of sparsity, incoherence and $\ell_1$ optimisation.

Consider the decomposition of the signal as,

$$\mathbf{x} = \boldsymbol{\Psi}\boldsymbol{\kappa} = \sum_{j=1}^{N} \boldsymbol{\psi}_j \kappa_j \; ; \quad \boldsymbol{\Psi} \in \mathbb{R}^{N\times N} \text{ (or } \mathbb{C}^{N\times N}) \tag{7-1}$$

where $\{\boldsymbol{\psi}_j\}_{j=1}^{N}$ is an orthonormal basis and the solution of coefficients $\kappa_j$ is generally an under-determined problem with an infinity of solutions. If the system is $k$-sparse, it means that there are $k$ significant coefficients and $N-k$ which are considered small enough to be neglected. One problem with this is that $k$ is usually unknown without first determining all the coefficients and then deciding which ones should be retained – this is the adaptive approach (as applied in the SD method). An important aspect of CS is that it is non-adaptive and does not require the explicit solution of the underdetermined problem described in Equation 7-1.

In CS [101], $\{\boldsymbol{\psi}_j\}_{j=1}^{N}$ is known as the sparcifying basis and should be minimally coherent with the so-called measurement basis,

$$\mu(\boldsymbol{\Xi}, \boldsymbol{\Psi}) = \sqrt{N} \cdot \max_{1\le p,q\le n} \left|\langle \boldsymbol{\varphi}_q, \boldsymbol{\psi}_p \rangle\right| \tag{7-2}$$

where the measurement is expressed as,

$$\mathbf{y} = \boldsymbol{\Xi}\mathbf{x}; \quad \boldsymbol{\Xi} = \begin{bmatrix} \boldsymbol{\varphi}_1^{\mathrm{T}} \\ \boldsymbol{\varphi}_2^{\mathrm{T}} \\ \vdots \\ \boldsymbol{\varphi}_m^{\mathrm{T}} \end{bmatrix} \in \mathbb{R}^{m\times N} \text{ (or } \mathbb{C}^{m\times N}) \tag{7-3}$$

and $m$ denotes the number of measurements.

If the measurements are selected by the use of delta functions, then the product $\boldsymbol{\Xi} \times \boldsymbol{\Psi}$ results in simply the values of the sparcifying basis at those instants then the delta functions are applied. One advantage of using the delta-function measurement basis is that the coherence of Equation 7-2 is known to be minimal when $\boldsymbol{\Psi}$ is the Fourier-transform basis. Thus, in the case of discrete time observation the Fourier basis

in Equation 7-1 is then defined as,

$$\boldsymbol{\psi}_j = \boldsymbol{\mathcal{F}}\mathbf{x} = \sum_{t=0}^{N-1} \mathbf{x}\, e^{-i\omega_j t};\ \omega_j = \frac{2\pi j}{N};\ \mathrm{j} = 0, 1, \ldots, N-1; \mathrm{i} = \sqrt{-1} \qquad (7\text{-}4)$$

Of course, different measurement and sparcifying bases may be used and it is known that a random measurement basis tends to be incoherent with any orthonormal sparcifying basis. Thus, for efficient storage and transmission of signals or images it is sufficient to define an incoherent product $\boldsymbol{\Xi} \times \boldsymbol{\Psi}$ where the signal is sparse according to the basis $\boldsymbol{\Psi}$ and the measurements (to be stored or transmitted) are compressed according to the basis $\boldsymbol{\Xi}$. Reconstruction of the signal is said to be achievable with overwhelming probability by $\ell_1$ optimisation [101, 114] when,

$$m \geq b \times \mu^2(\boldsymbol{\Xi}, \boldsymbol{\Psi}) k\, log(N) \qquad (7\text{-}5)$$

where *b* is a small positive constant. Then the estimated coefficients are given by,

$$\hat{\boldsymbol{\kappa}} = arg \min_{\boldsymbol{\kappa}} \|\boldsymbol{\kappa}\|_1 \quad \text{subject to} \quad \boldsymbol{\Xi}\boldsymbol{\Psi}\boldsymbol{\kappa} = \mathbf{y} \qquad (7\text{-}6)$$

$\ell_1$ norm $\|\cdot\|_1$ is defined in appendix A.2.

and the reconstructed signal may be expressed as,

$$\hat{\mathbf{x}} = \boldsymbol{\Psi}\hat{\boldsymbol{\kappa}} \qquad (7\text{-}7)$$

The advantage of $\ell_1$ minimisation is easily illustrated by the ball of unit norm in the space of the coefficients $\kappa_j$. Figure 7-1 shows the simple and easily visualised 2-dimensional case. Whereas the 2-norm solution is defined by 2 coefficients, the 1-norm solution is of minimal dimension $k = 1$. Thus, by the non-adaptive CS approach it is

not necessary to determine the number $k$ of significant coefficients explicitly, since this is done as part of (and within) the $\ell_1$ minimisation procedure. An example for illustration of signal reconstruction using CS is presented in Figure 7-2.

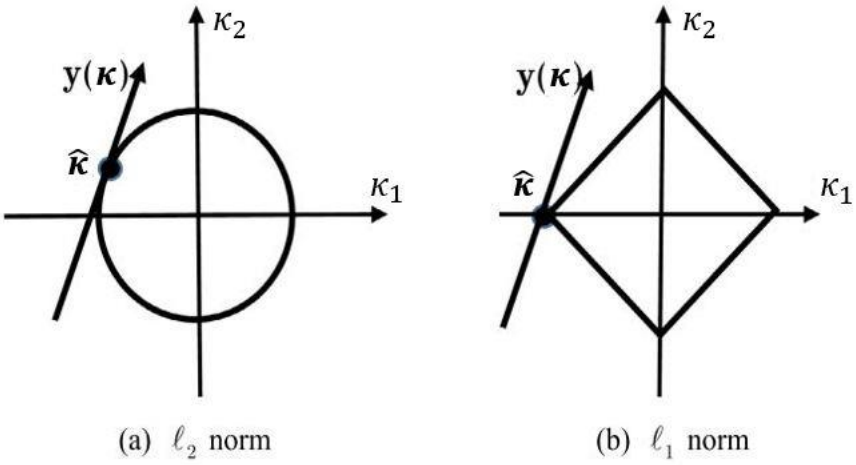


Figure 7-1. $\ell_2$ and $\ell_1$ norm solutions.

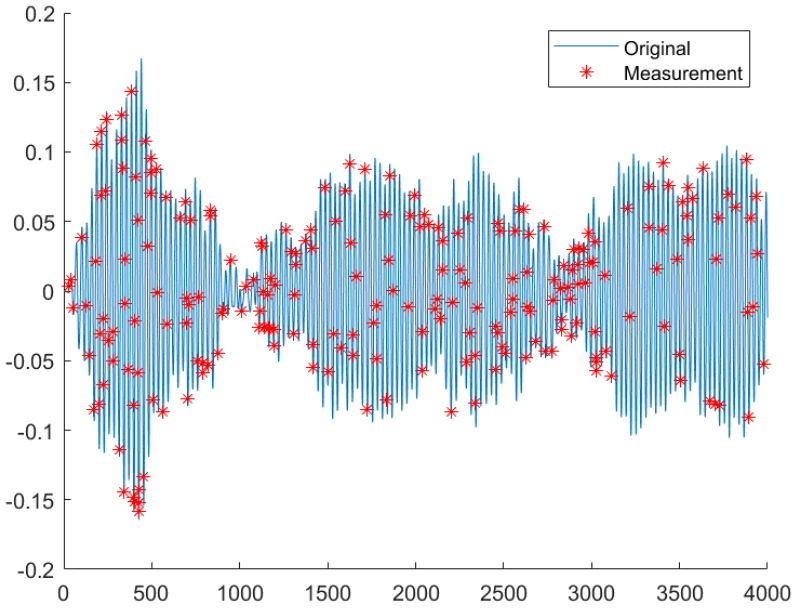


(a) The original signal and measured samples.

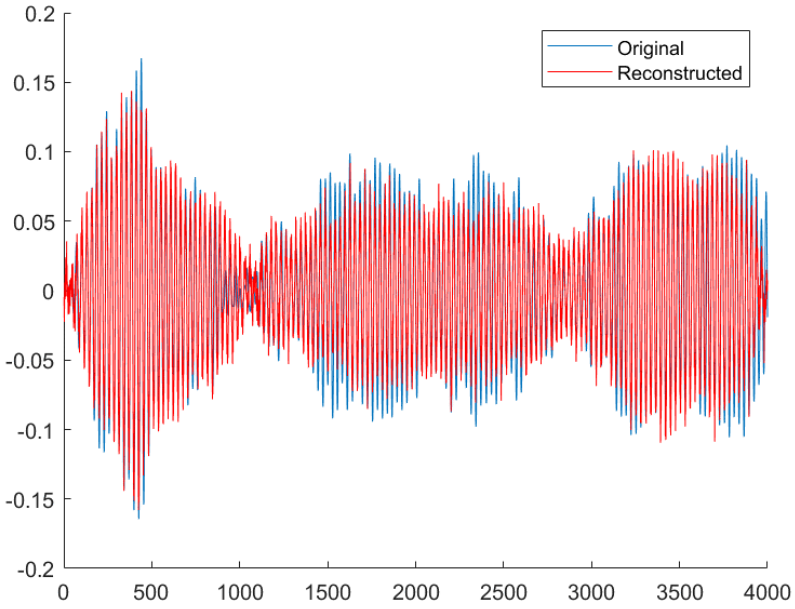


(b) The original and CS reconstructed signal.

Figure 7-2. The CS sampling and reconstruction of a signal.

In the case of vibration images, as described in what follows, the Fourier

Transform basis is used for sparcification and the measurements are delta functions. The minimum total variation (TV) algorithm with equality constraints is applied. This algorithm is fully described in Appendix E of [114] in which the gradients of the image, which tend to be sparser than displacements, are considered and are thus better suited to CS. The TV of $\mathbf{x}$ is thus given by,

$$\mathrm{TV}(\mathbf{x}) = \sum_{pq} \sqrt{\left(D_{h;pq}\mathbf{x}\right)^2 + \left(D_{v;pq}\mathbf{x}\right)^2} \tag{7-8}$$

where the subscripts $h$ and $v$ denote horizontal and vertical,

$$D_{h;pq} = \begin{cases} x_{p+1,q} - x_{pq} ; p < n_h \\ 0 ; p = n_h \end{cases} \quad D_{v;pq} = \begin{cases} x_{p,q+1} - x_{pq} ; q < n_v \\ 0 ; q = n_v \end{cases} \tag{7-9}$$

And $n_h$ and $n_v$ denote the number of data points in each of the two directions.

### 7.2 Experimental case study

The circuit board is a real experimental example of DIC data from an industrial company, and only the displacement maps, not the original images, are received. It was partly obscured by other components so that the camera had only two separate parts of the circuit board in view, as shown in Figure 7-3. The boundary condition of the circuit board was not known by the company, who were able to provide only the following information. The structure was excited randomly within the frequency range of 200 to 1000 Hz, and the sampling frequency of the highspeed cameras was set at 2000 Hz. The total duration of measurement was 1.579 s, and hence the resulting number of steps was 3158.

(b) part 2

(a) part 1

Figure 7-3. Circuit board parts 1 (a) and 2 (b).

The printed circuit board forms the subject of tests carried out in subsequent sections to illustrate the application of SD and CS procedures to industrial full-field vibration test scenarios.

### 7.3 CS procedure

Each of the 3158 DIC images consists of a total number of DIC data points of 8091 for the two parts of the circuit board - after removal of points corresponding to the circuit-board holes. There are two alternative approaches that might be considered here. First, the TV algorithm might be applied to the 3158 DIC images, and secondly CS might be applied to the 8091 data-points time signals. It will be demonstrated subsequently that the first approach incurs an unacceptable computational cost and compression achieved by the second approach is vastly inferior to the combined SD/CS

method proposed herein.

Instead of either of above approaches CS will now be considered with SD decomposition applied a-priori. By this approach each of the 3158 images is projected onto a set of time-independent orthogonal kernel functions, with coefficients, known as SD, that form a time-varying signal. The kernels are developed from the data itself using the algorithm introduced in chapter 6, which has the advantage of significantly reducing the number of kernels necessary to reproduce the original image. In this way, for maximum efficiency of storage and transmission, CS is applied both to the SD signals and to each of the kernel functions separately.

For CS of the SD signals, the measurement basis takes the form of delta functions, random in time [114]. The Fourier transform basis is applied for sparcification. The kernel function gradients require 2-D Fourier transformation for sparcification and the measurements are taken along equi-spaced radial scan lines taken from the centre of the image as illustrated in Figure 7-4. The complete CS procedure is illustrated in Figure 7-5.

(a) pattern of 5 scan lines

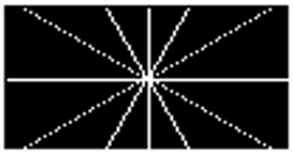

(b) pattern of 6 scan lines

(c) pattern of 7 scan lines

(d) pattern of 8 scan lines

Figure 7-4. Patterns with different numbers of scan lines.

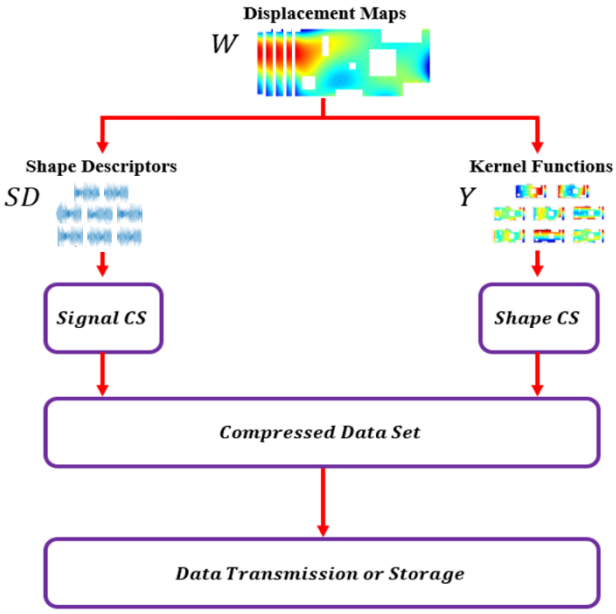


Figure 7-5. Flow chart of the compression scheme.

Reconstruction of SD signals and kernels by $\ell_1$ optimisation is described in section 7-3 and 7-4 and illustrated in Figure 7-6. The procedure described in Figures 7-5 and 7-6 allows for in-situ measurement and compression, with remote reconstruction of transmitted compressed data for OMA.

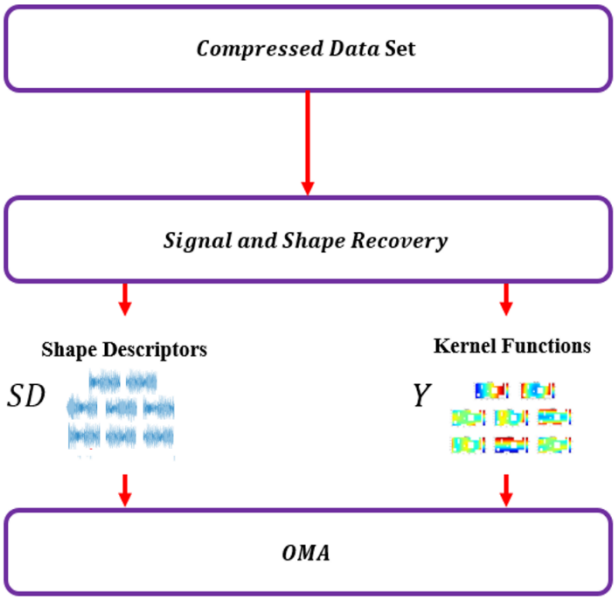


Figure 7-6. Flow charts of the recovery scheme.

### 7.4 CS of a single image

In this section, the problem of applying CS directly to a single DIC image is considered. This corresponds to the first of two possible approaches postulated in section 7-3, and the effect of applying different numbers of scan lines is investigated. Firstly, however, the correlation of CS-recovered images with time-progressing raw DIC data is shown in Figure 7-7 using only nine scan lines. It is immediately apparent that the number of scan lines is not enough to obtain a sufficiently good correlation. The lowest and highest correlations are found to be 0.3546 and 0.8695 at time instants 3020 and 3029 respectively. The corresponding DIC displacement images are shown in Figure 7-8.

The advantage of increased sparcity of data-point gradients over data-point values directly is illustrated in Figure 7-9 for part 2 of the circuit board, where it is seen the number of negligibly small gradients is more than twenty times the number of small data-point values for the displacement image with the lowest correlation. The data-point gradients for the lowest and highest correlated images are compared in Figure 7-10. Although the highest correlated image has the highest gradients it is the shape of the curves in the figure that determines the sparcity. The blue curve for the lowest correlated image bends over and becomes almost flat at around data point 2300 to 2700. It contains a greater number of significant data-point gradients than the sharper red curve, which contains only a few significant gradients near the right-hand tip. The number of data points shown in Figures 7-9 and 7-10 is the total remaining after eliminating those where there are holes in the circuit board material.

To improve the correlation, the number of scan lines should be increased. The effect of doing so is shown in Figure 7-11, where the lowest correlated image is recovered almost perfectly when CS is applied with 25 scan lines. The recovered

displacement images corresponding to the data points in Figure 7-11 are illustrated in Figure 7-12 for purposes of comparison.

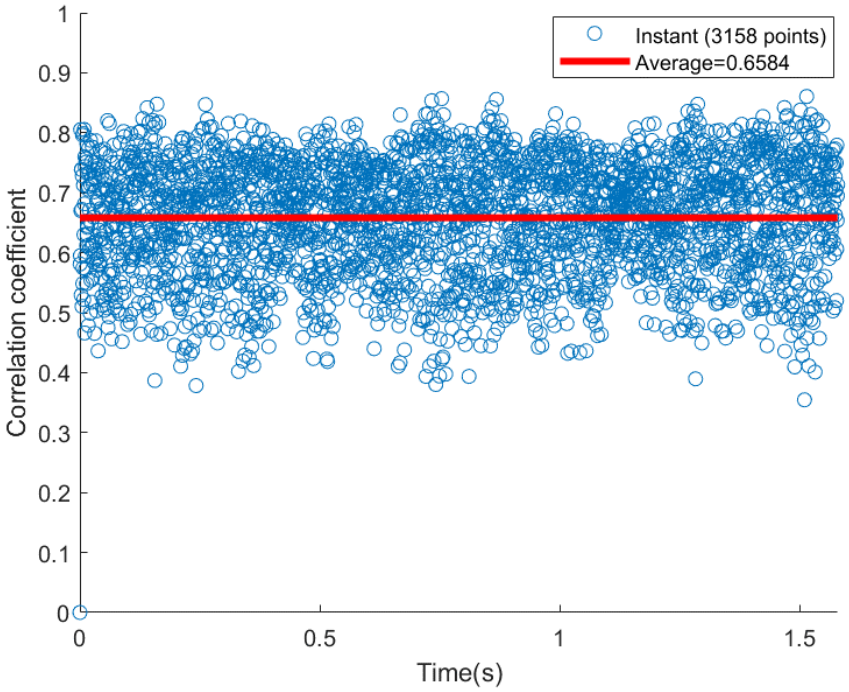


Figure 7-7. Correlation coefficients of recovered displacement images: circuit board part2.

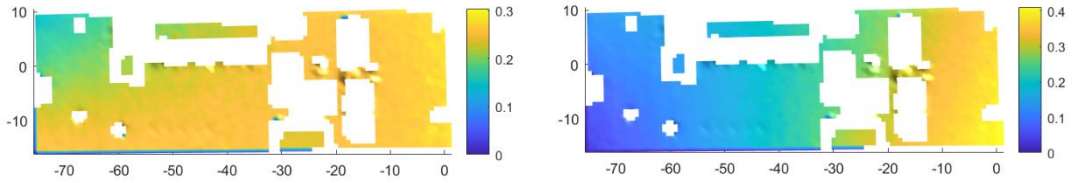


(a) Lowest (b) Highest

Figure 7-8. Displacement images with the lowest and highest correlation coefficients.

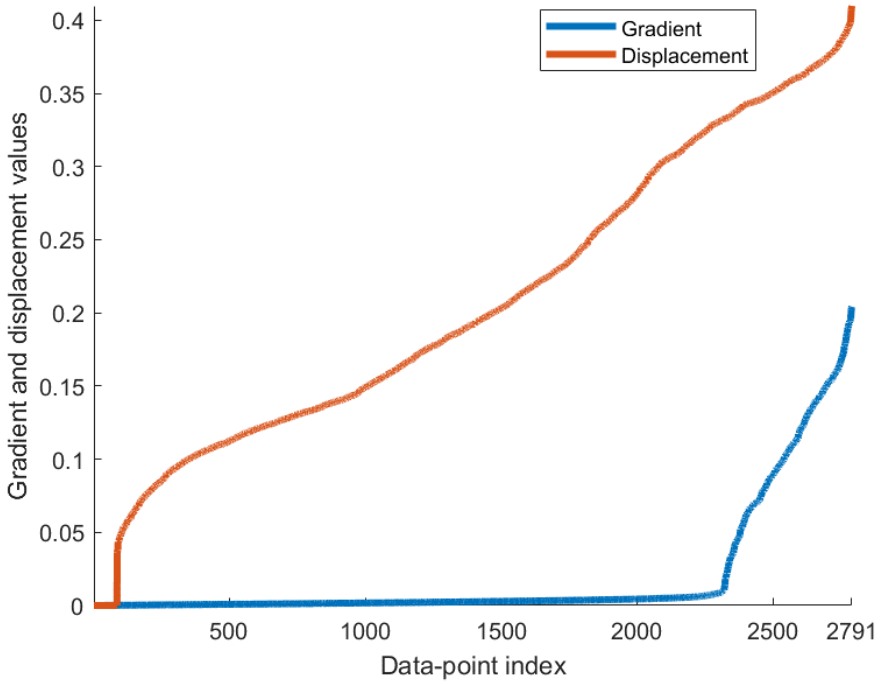


Figure 7-9. Sorted absolute values of data-point gradient and displacement vs. data-point index: highest correlation coefficient.

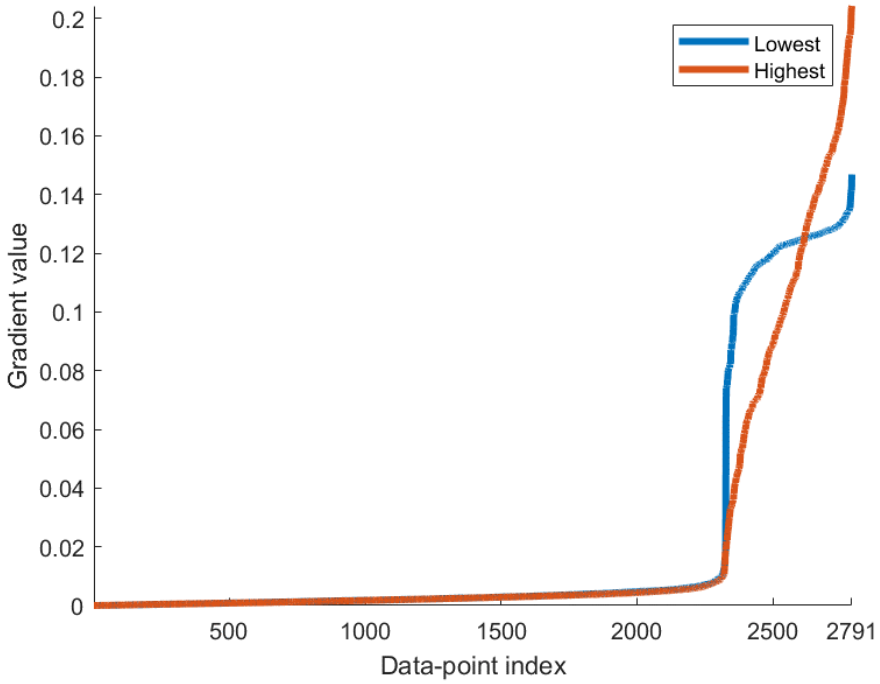


Figure 7-10. Sorted absolute values of data-point gradients vs. data-point index: lowest and highest correlation coefficients.

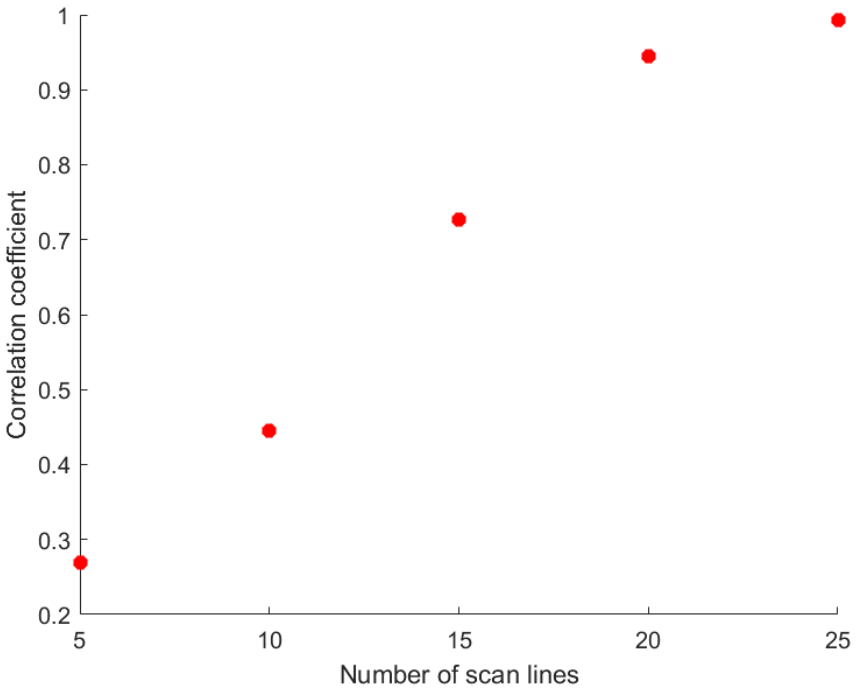


Figure 7-11. Correlation coefficients of recovered images vs. number of scan lines.

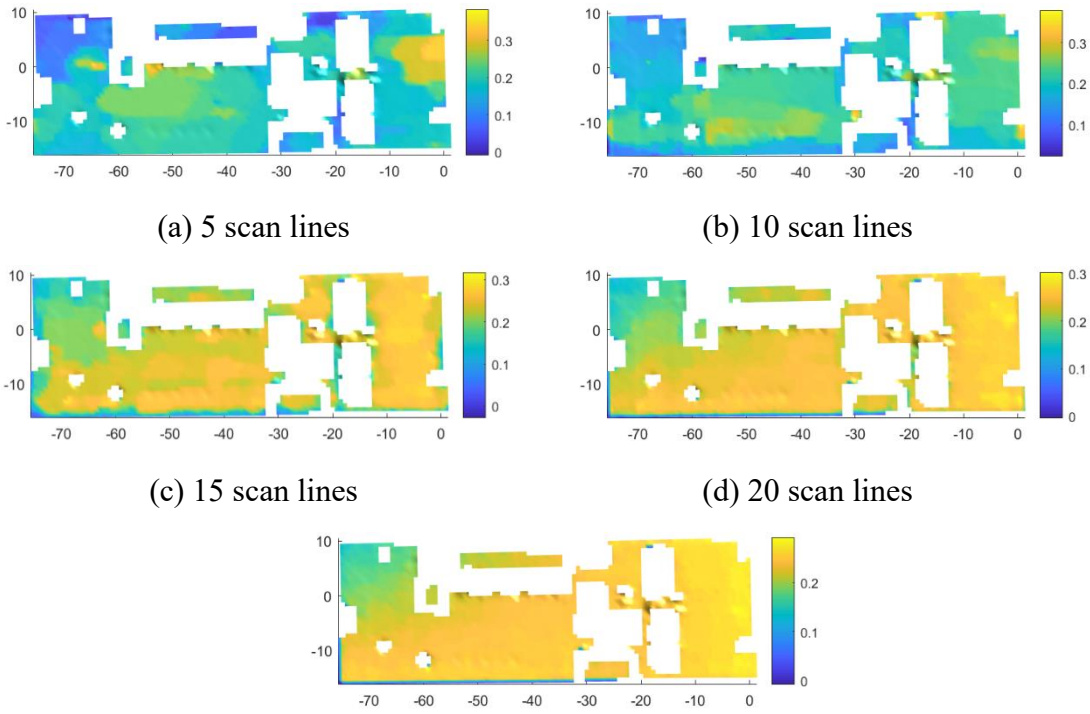

(a) 5 scan lines

(b) 10 scan lines

(c) 15 scan lines

(d) 20 scan lines

(e) 25 scan lines

Figure 7-12. Recovered displacement images with different number of scan lines.

Image recovery by $\ell_1$ optimisation, in the case of 25 scan lines, takes around 20 seconds on a standard desk-top computer. For the full series of 3158 images the recovery time amounts to an excessive 18 hours. As has already been suggested, one way to overcome this problem is to carry out a preliminary SD reduction. Figure 7-13 shows the correlation functions for the first eight SD kernel functions using the same 9 scan-lines as in Figure 7-7. Clearly the kernel functions are sparser than the raw DIC data. Whereas the average correlation coefficient for the kernels is over 88%, that for the displacement images is only around 65%.

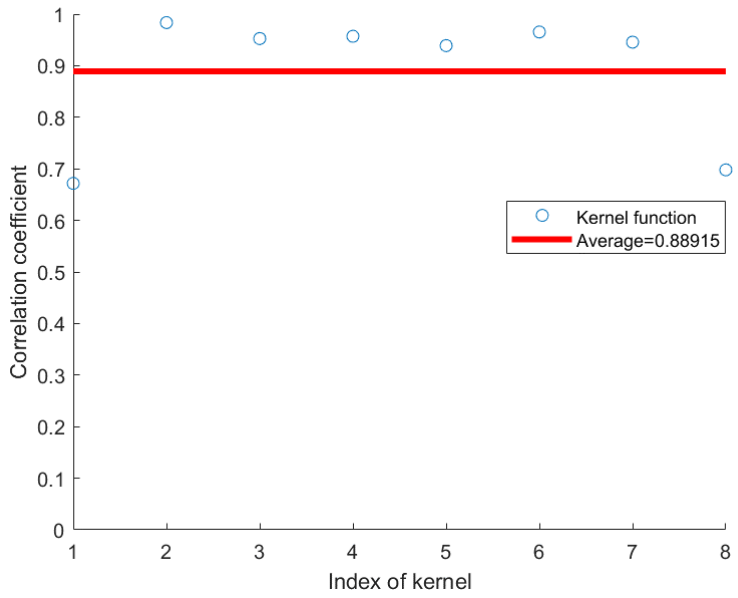


Figure 7-13. Correlation coefficients for kernel functions of circuit board part 2.

## 7.5 CS for OMA

Following the CS recovery, operational modal analysis of the SD data was carried out according to the procedures described in chapter 6. Modal identification requires only the signals in the SD domain, then mode-shape visualisation can be achieved using

the kernel functions. In the present example, the determination of modal properties was conducted using the stochastic subspace identification (SSI) algorithm explained in chapter 4. By using the SD technique described in chapter 6, there were found to be eight significant kernel function terms in the updated basis; the identified frequencies from chapter 6 are presented in Table 7-1.

Table 7-1. Identified natural frequencies from the updated basis of the circuit board.

| Mode | 1 | 2 |
|---|---|---|
| Frequency (Hz) | 535.297 | 779.039 |

Figure 7-14 shows the number of uniformly distributed random samples of the SD signals and the number of radial scan lines of the kernels needed to exceed a threshold of 0.9 on the obtained MAC values, between the recovered and original SD data. It is clear that 650 random samples and 9 scan lines are sufficient. The resulting mode shapes are shown in Figure 7-15 where close agreement between the recovered and original SD images can be observed. Of course, an even greater number of random samples and scan lines would result in even closer agreement.

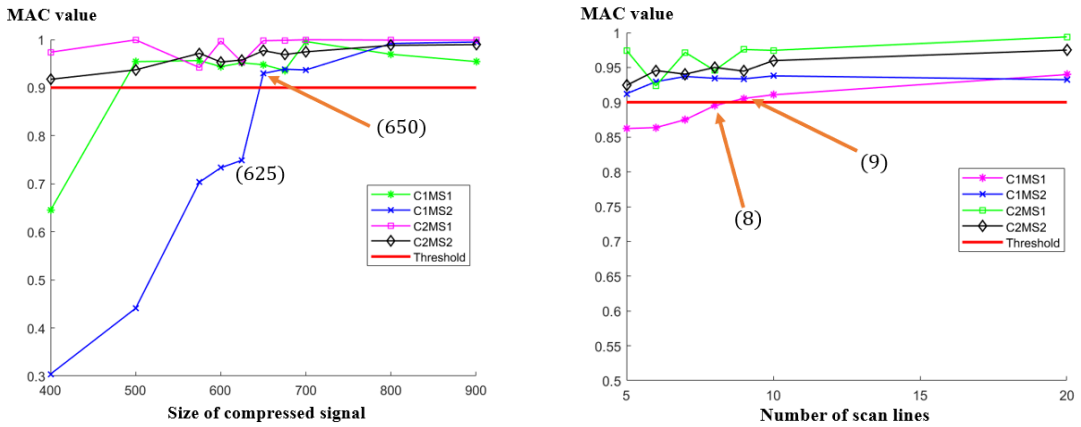


(a) Threshold for SD signals. (b) Threshold for kernel functions.

Figure 7-14. Sampling requirements to exceed MAC threshold of 0.9 (C – circuit board, MS – mode shape).

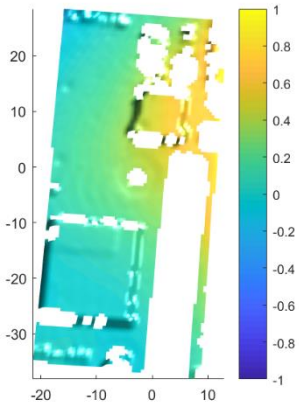


(a) 1st mode shape of circuit board part 1 from original SD data

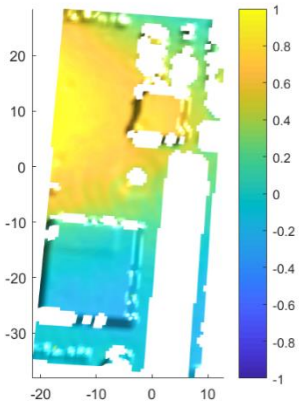


(b) 2nd mode shape of circuit board part 1 from original SD data

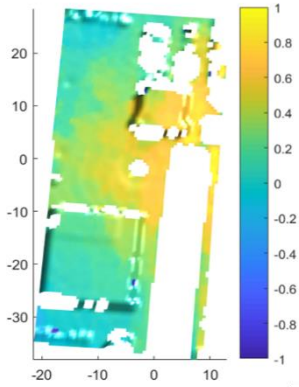


(c) 1st mode shape of circuit board part 1 from recovered SD data

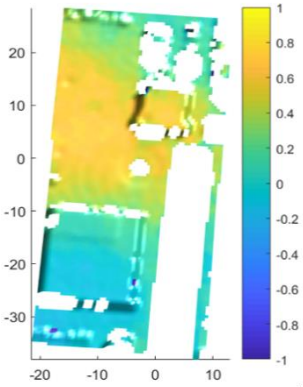


(d) 2nd mode shape of circuit board part 1 from recovered SD data

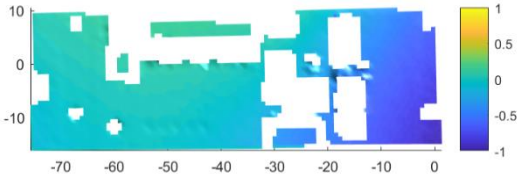


(e) 1st mode shape of circuit board part 2 from original SD data

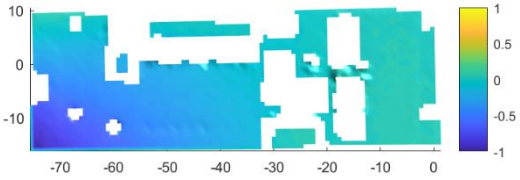


(f) 2nd mode shape of circuit board part 2 from original SD data

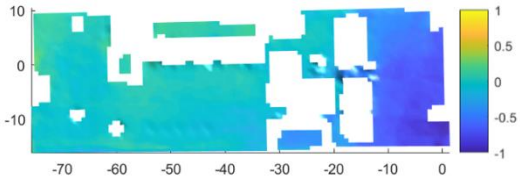


(g) 1st mode shape of circuit board part 2 from recovered SD data

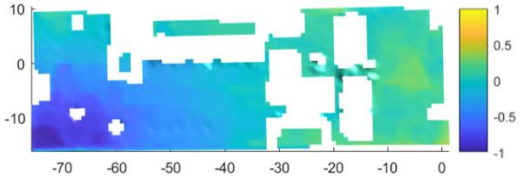


(h) 2nd mode shape of circuit board part 2 from recovered SD data

Figure 7-15. The comparison of identified mode shapes of data measured from circuit board. (Unit of axes in mm)

Natural frequencies from original and recovered SD data are presented in Table 7-2, where differences are given in percentage terms. The compression of signals and kernel functions achieved by CS over prior-reduced SD data is given in Tables 7-3 and 7-4 for parts 1 and 2 of the circuit board respectively. It is seen that the effect of CS is the reduction of kernels by more than fourteen and eleven times for the two parts. In chapter 6 compression ratios of over 160 and 110 for parts 1 and 2 were obtained by SD basis updating. When multiplied by the present compression ratios, the data needed for storage and transmission is further reduced by approximately 5 times more.

Also, from Tables 7-3 and 7-4 it is seen that the compression ratio for SD signals is close to 5. It is clear the second approach postulated in section 7-3, of compressing the 8091 DIC date-point signals, is likely to be highly inefficient when compared to the proposed approach, even if the compressive ratio of 5 were to be exceeded (doubled or greater) for at least some of the data-point signals.

Table 7-2. Identified natural frequencies (Hz)

| Mode | 1 | 2 |
|---|---|---|
| Original SD data | 535.297 | 779.039 |
| Recovered SD data | 533.238 | 779.740 |
| Difference in % | 0.385 | 0.090 |

Table 7-3. Compression ratios for signals and kernel functions: circuit board part 1.

| | Signal size | Compression ratio | Kernel | Compression ratio |
|---|---|---|---|---|
| Original | 3158 time instants | 4.86 | 5300 spatial data | 14.29 |
| proposed method | 650 measurements | | 371 measurements | |

Table 7-4. Compression ratios for signals and kernel functions: circuit board part 2.

| | Signal size | Compression ratio | Kernel | Compression ratio |
|---|---|---|---|---|
| Original | 3158 time instants | 4.86 | 2791 spatial data | 11.3 |
| proposed method | 650 measurements | | 247 measurements | |

## 7.6 Closure

In-situ data compression and remote reconstruction is an important practical issue for numerous industries that rely upon efficient data storage and transmission. However, CS alone is found to be prohibitively expensive for the processing of many thousands of camera images, each containing typically tens or hundreds of thousands of data points. A solution to this problem is presented in the form of a combined approach whereby CS is preceded by SD decomposition and applied to SD time signals and kernel functions. This procedure is demonstrated on industrial DIC data from a partially observed printed circuit board. Further significant compression is achieved (beyond the SD reduction) and OMA is carried out successfully on CS-recovered data.

# 8 Conclusion and Future Studies

## 8.1 Conclusions

In this study, the problem of data compression of displacement maps from 3D-DIC measurement is addressed. As a non-contact optical full-field measurement technique, 3D-DIC displacement measurement is becoming more widely applied to various kinds of dynamic issues. The research presented in this thesis attempts to apply the algorithms of sparse representation to deal with the huge amount of data acquired from 3D-DIC measurement. It aims to develop methods that have the capability of preserving nuances of displacement measurement and retaining the compactness of image decomposition. Accordingly, two useful compression methods based upon the well-known K-SVD algorithm and CS method are developed for the purpose of a succinct and representative decomposition of displacement maps from 3D-DIC measurement.

i. **Basis-updating algorithm:** The major issues related to the integration of camera-based systems with dynamic measurement is the generation of huge amounts of data, because of the requirements of high sampling rate, spatial resolution, and long duration of recording. The proposed algorithm addresses the need for efficiency in full-field data processing. The working of the algorithm depends upon the data itself and it is this feature that enables it to achieve such significant improvements in compression ratio over classical orthogonal kernels (including the AGMD). A reduced number of new basis functions is determined for the representation of data under the condition that the reconstructed displacement map reproduces the raw measured data to within a chosen threshold on the coefficient of correlation. It is particularly useful that a threshold may be placed on the correlation with the raw

measured data to ensure that important features of DIC displacement maps are not lost by truncation. In both simulated and experimental cases, the compression ratios for data size and number of signals used in operational modal analysis are substantially diminished, thereby demonstrating the effectiveness of the proposed algorithm.

ii. **SD-CS method:** The monitoring of an operating structure usually dealing with multiple set of data, which could pose an issue for transmission or storage and is especially true when data acquisition is implemented with cameras, such as 3D-DIC system. Single images regularly extend to tens or even hundreds of thousands of data points and many thousands of images may be required for a single set of vibration tests. Such data must be handled efficiently for later remote reconstruction and analysis, typically OMA. It is this requirement that is addressed and solved by the integrated SD-CS method because of the fact that CS alone is found to be prohibitively expensive for the processing of many thousands of camera images. Data reduction by a combination of SD decomposition and CS is applied to an industrial printed circuit board and reconstructed for OMA by $\ell_1$ optimisation. This procedure is demonstrated on industrial DIC data from a partially observed printed circuit board and further significant compression is achieved (beyond the SD reduction) and OMA is carried out successfully on CS-recovered data.

In summary, the basis-updating algorithm is a powerful tool for the adaptation of kernel functions to data collected by 3D-DIC displacement measurement systems. The algorithm is capable of finding a representative set of shape descriptors for displacement maps from an initial basis without any relation to the data. On the other hand, the integration of CS theory and SD method offers a new way to extract the core

information from the measured data. This post-processing technique not only improves the compression ratio but also provides the possibility of structural health monitoring.

## 8.2 Future studies

Although the proposed methods have demonstrated effectiveness in reducing the dimension of data acquired from 3D-DIC measurement and retaining the important information at the same time, there are still some unknown potential worthy of exploring for the proposed methods to be used in a wide range of applications. Therefore, a further study into the applications of the proposed methods could lead to a powerful development of DIC-based tools. In the following, two possible extensions to the existing study in this thesis might be recommended and should be beneficial for further research.

i. **Extension to online structural health monitoring (SHM)**: The demonstration of the proposed method is implemented either on the data acquired from numerical simulation or condition-controlled experiments. The operational modal analysis is done in a post-processing manner instead of direct way. There are a few challenges that must be handled before applying the method to online structural health monitoring, such as the processing speed of the proposed method should be optimised so that the delay of measurement and display of result could be minimised, and the decomposition or compression of the data should be automatically fulfilled instead of manual selecting or deciding the relevant parameters.

ii. **Extension to digital volume correlation (DVC) measurement:** The developed basis-updating algorithm and SD-CS method are currently only applied to 3D-DIC measurement. Nonetheless, it should be possible to extend the current methods to

DVC since basic concepts and algorithms are similar to regular DIC. DVC measurement requires an imaging system capable of acquiring volumetric images of a specimen. For this purpose, X-ray tomography (also called computed tomography (CT)), magnetic resonance imaging (MRI) are popular techniques used in medical imaging. However, problems related to image acquisition, image storage and computation in DVC require more understanding. Thus, further research needs to be carried out to fully consider possible issues in order to successfully extend the proposed methods to DVC.

For a wide range of practical problems in the world, the size of data is usually much larger than those demonstrated in this study, and the processing time and capacity might be much more limited due to harsh environment and condition. Future developments of this application should focus on improving its performance in challenging applications and adaptability for difficult problems.

# Appendices

# A. Basic Mathematical Definitions

### A.1 Gram-Schmidt orthonormalisation (GSO)

In mathematics, particularly linear algebra and numerical analysis, the Gram–Schmidt process [115] is a method for orthonormalising a set of vectors in an inner product space, most commonly the Euclidean space $\mathbb{R}^n$ equipped with the standard inner product. The inner product of two arbitrary functions $\mathbf{u}$ and $\mathbf{v}$ in a continuous domain $\Omega(\chi)$ is defined by,

$$\langle \boldsymbol{u}, \boldsymbol{v} \rangle = \int_{\Omega(\chi)} \mathbf{u}(\chi)\mathbf{v}(\chi)\, d\chi \tag{A-1}$$

and the orthogonality of the functions is confirmed when the inner product is zero.
In a discrete domain, the inner product of two arbitrary functions $\mathbf{u}$ and $\mathbf{v}$ can be represented by the discrete version as

$$\langle \mathbf{u}, \mathbf{v} \rangle = \sum_i \mathbf{u}(\chi_i)\mathbf{v}(\chi_i) d\chi_i \tag{A-2}$$

Before the introduction of GSO procedure, the projection operator is defined as

$$proj_{\mathbf{u}}(\mathbf{v}) = \frac{\langle \mathbf{v},\mathbf{u} \rangle}{\langle \mathbf{u},\mathbf{u} \rangle}\mathbf{u} \tag{A-3}$$

This operator projects the vector $\mathbf{v}$ orthogonally onto the line spanned by vector $\mathbf{u}$.

The GSO procedure for a set of kernel functions $\{\mathbf{q}_1, \mathbf{q}_2, \dots, \mathbf{q}_n\}$ in a discrete domain may be expressed as

$$\begin{cases} \mathbf{t}_1 = \mathbf{q}_1 \\ \mathbf{t}_k = \mathbf{q}_k - \sum_{j=1}^{k-1} proj_{\mathbf{t}_j}(\mathbf{q}_k), k = 2, \dots, n \\ \mathbf{r}_\mathrm{k} = \mathbf{t}_\mathrm{k} / \|\mathbf{t}_\mathrm{k}\|_2, k = 1, \dots, n \end{cases} \quad \text{(A-4)}$$

where $\{\mathbf{r}_1, \mathbf{r}_2, \dots, \mathbf{r}_n\}$ is an orthonormal set of kernel functions.

The method works by first choosing a kernel function as the starting direction, and sequentially updating others by removing components of previous kernel functions.

### A.2 The Norm of a Vector (or Matrix)

In linear algebra, a norm is a function that assigns a strictly positive length or size to each vector in a vector space except for the zero vector, which is assigned a length of zero. On the other hand, a matrix norm is a vector norm in a vector space whose elements are matrices of given dimensions.

#### A.2.1 $\ell_p$ vector norm

Let $p \geq 1$ be a real integer number. The $\ell_p$ norm of vector $\mathbf{x} = \{x_1 \quad \cdots \quad x_n\}$, where $n$ is a positive integer, is defined by

$$\|\mathbf{x}\|_p := \left(\sum_{i=1}^{n} |x_i|^p\right)^{1/p} \quad \text{(A-5)}$$

For p = 1 we get the Manhattan norm or Taxicab norm

$$\|\mathbf{x}\|_1 := \sum_{i=1}^{n} |x_i| \quad \text{(A-6)}$$

For p = 2 we get the Euclidean norm

$$\|\mathbf{x}\|_2 := (\sum_{i=1}^{n} x_i^2)^{1/2} \tag{A-7}$$

And as p approaches $\infty$ the p-norm approaches the infinity norm or maximum norm

$$\|\mathbf{x}\|_\infty := \max_i x_i \tag{A-8}$$

### A.2.2 $\ell_0$ vector norm

Strictly speaking, $\ell_0$ norm is not actually a norm. It is a cardinality function which has its definition in the form of $\ell_p$ norm, though many people call it a norm. In reality, most mathematicians and engineers use this definition of $\ell_0$ norm instead:

$$\|\mathbf{x}\|_0 := \#(i|x_i \neq 0) \tag{A-9}$$

where # represents the number, therefore, $\ell_0$ norm is the total number of non-zero elements in a vector.

### A.2.3 Frobenius matrix norm

Frobenius norm is an entrywise matrix norm, it is also called the Hilbert–Schmidt norm. Given a matrix $\mathbf{A} = \begin{bmatrix} a_{11} & \cdots & a_{1n} \\ \vdots & \ddots & \vdots \\ a_{m1} & \cdots & a_{mn} \end{bmatrix} \in \mathbb{R}^{m \times n}$, the Frobenius norm is defined by

$$\|\mathbf{A}\|_F = \sqrt{\sum_{i=1}^{m} \sum_{j=1}^{n} |a_{ij}|^2} \tag{A-10}$$

where $\|\cdot\|_F$ represents Frobenius norm.

# B. Verification of OMA methods

The simulated data for verification of OMA methods is produced by using the ABAQUS FE software. The FE model of a plate structure with fully-fixed boundary conditions displayed within ABAQUS interface is shown in Figure B-1. The parameters of the FE simulation are provided in Table B-1 and the three natural frequencies and mode shapes within the excitation range are presented in Figure B-2. For the verification, all three OMA methods, i.e. SSI, P-LSCF and Bayesian methods, used in the thesis are applied to the simulated out-of-plane displacement recordings correspond to the data points on the surface of the FE specimen. And from the comparison of the estimated result of each method in MATLAB with those calculated by ABAQUS, it can be confirmed that the MATLAB codes of SD decomposition and these OMA methods function properly for the identification of modal properties.

Table B-1. The parameters of FE simulation.

| | |
|---|---|
| Material | A36 Steel: Young's Modulus: 550GPa<br>Poisson's ratio: 0.26<br>Density: 7850 Kg/$m^3$ |
| Dimension | Width: 1 m Height: 0.5 m Thickness: 0.01 m |
| Section | Solid, Homogeneous |
| Element size | 0.01 m by 0.01 m by 0.01 m |
| Boundary condition | As shown in Figure B-1 (b) |
| Excitation | Excitation: Zero-mean Gaussian white noise (58 ~ 85 Hz) |
| Sampling frequency | 1000 Hz |
| Number of steps | 4000 (4 seconds) |
| Output | 5151 out-of-plane displacement recordings |

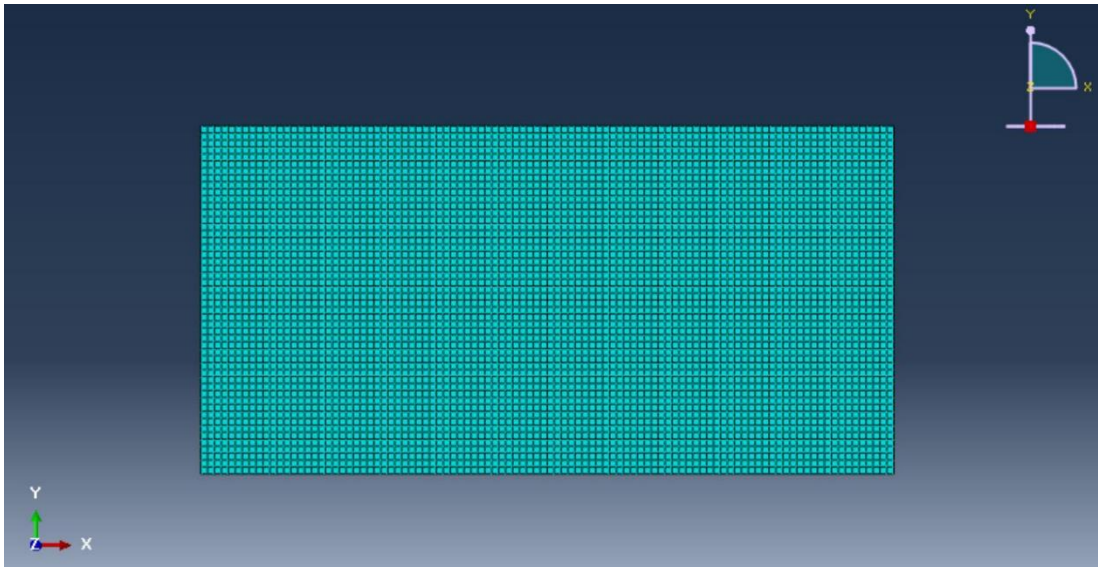

(a) FE mesh plot.

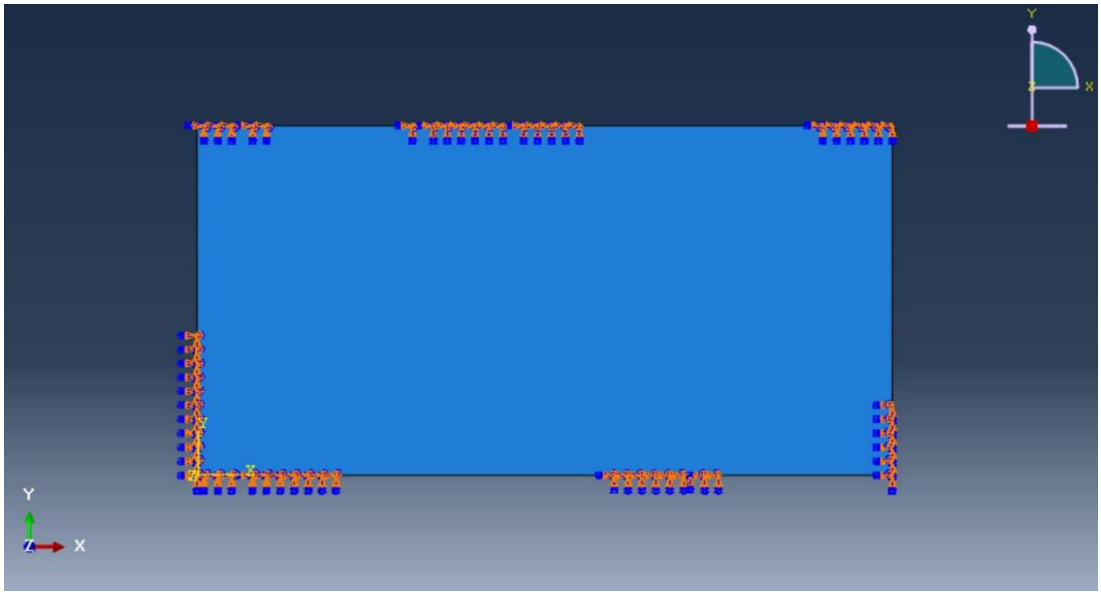

(b) FE model with all the fully-fixed boundary conditions.

Figure B-1. The simulated FE model displayed in ABAQUS interface.

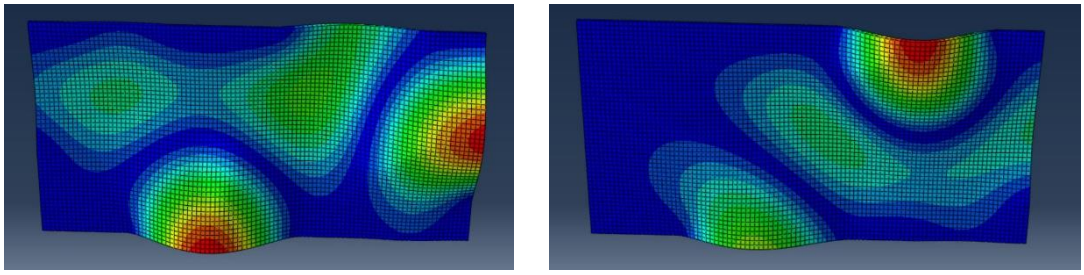

(a) 62.178 Hz (b) 73.265 Hz

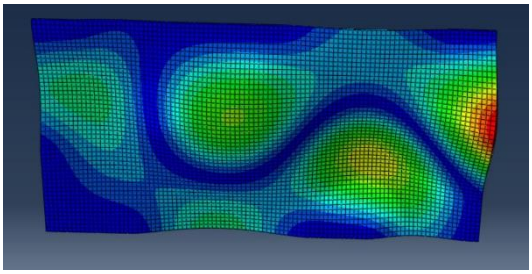

(c) 84.108 Hz

Figure B-2. The mode shapes within excitation range estimated by ABAQUS from the FE model.

The kernel functions for the SD decomposition of the displacement maps are generated by AGMD method as mentioned in Chapter 4, and there are in total 24 AGMDs as illustrated in Figure B-3. The corresponding SD signals are provided in Figure B-4 with the same ordering.

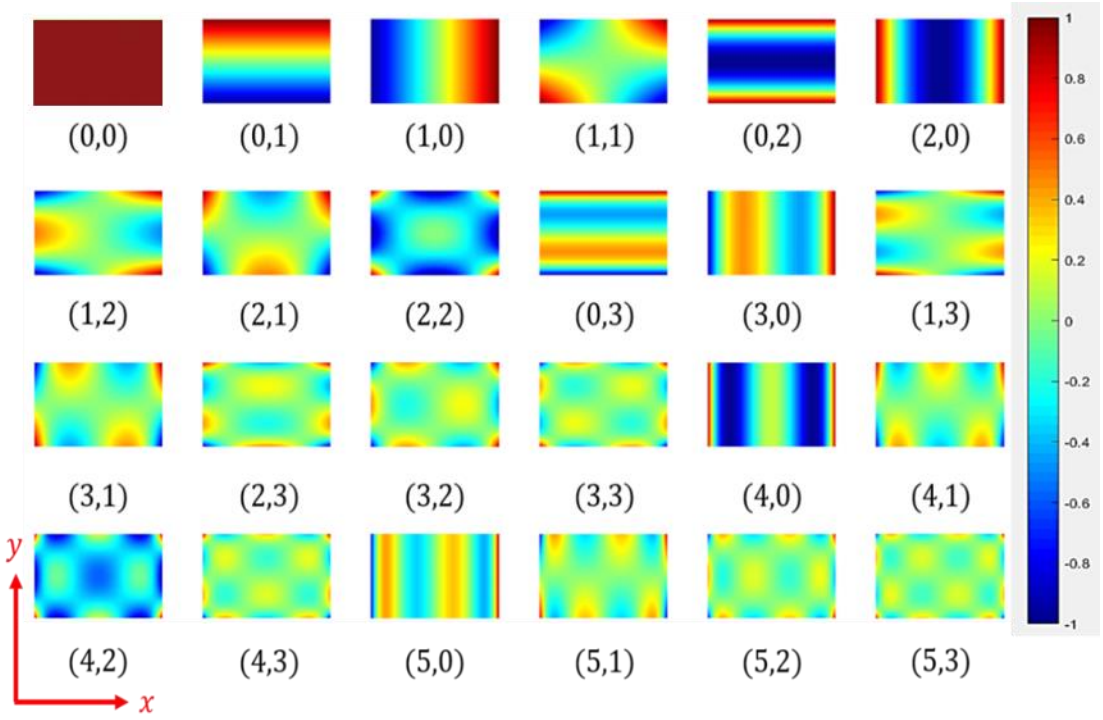


Figure B-3. The 24 scaled polynomials by AGMD with orders in x and y directions respectively.

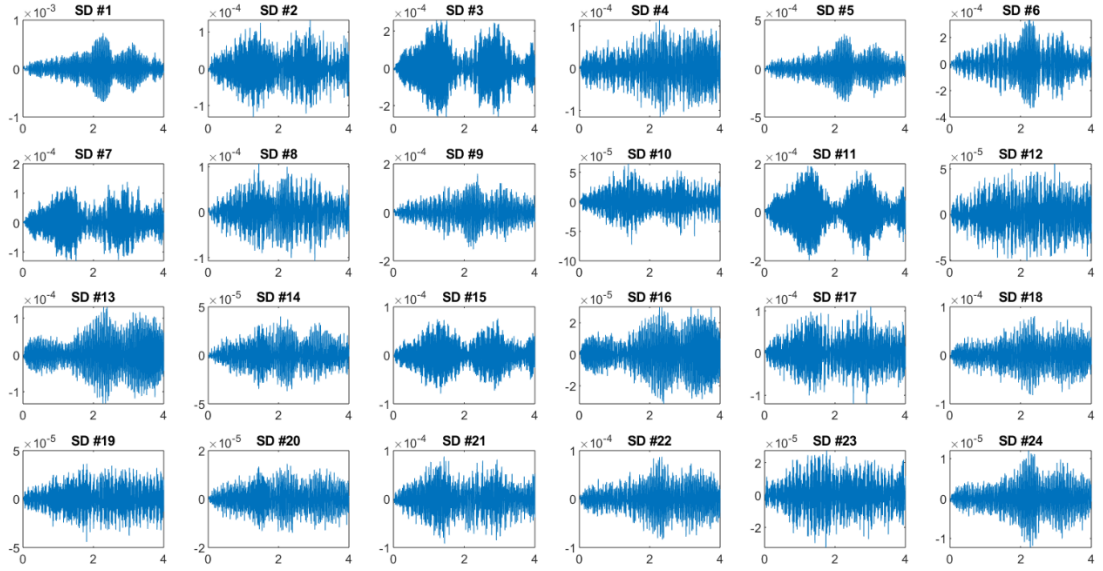


Figure B-4. The corresponding SD signals. (x axis – time in second, y axis – magnitude)

For a successful reconstruction of displacement from the basis and SD coefficients, the orthogonality among the kernel functions is of paramount importance. The orthogonality can be ensured as seen in Figure B-5, and the individual and average correlation coefficients of all instants are presented in Figure B-6.

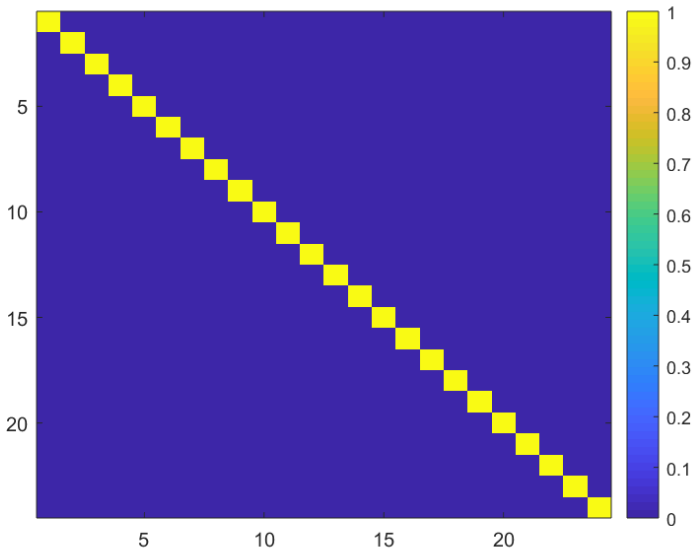


Figure B-5. The orthogonality map.

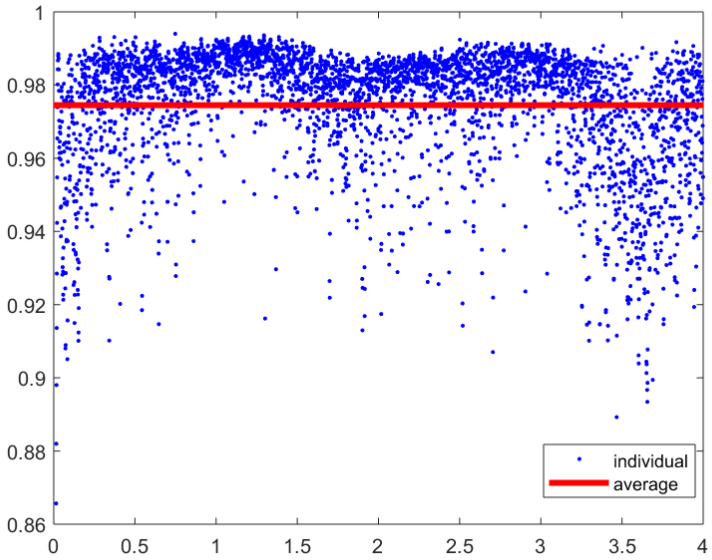


Figure B-6. The individual and average correlation coefficients between the original and reconstructed displacement maps of all instants. The average value is 0.9745. (x axis – time in second, y axis – correlation coefficient).

In Figure B-7, the stablisation diagram estimated by SSI method is shown, and the stable modes identified by removing the spurious ones can be seen in Figure B-8.

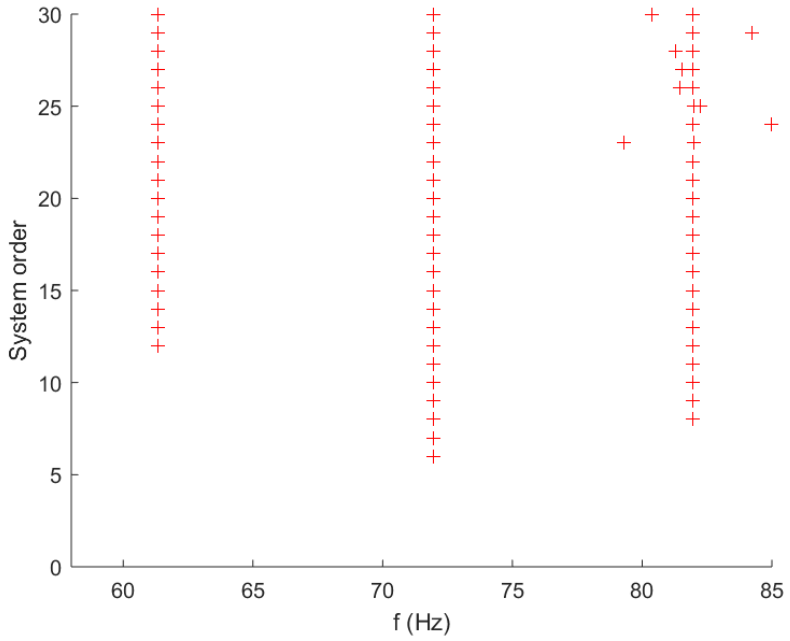


Figure B-7. The stabilisation diagram estimated by SSI method.

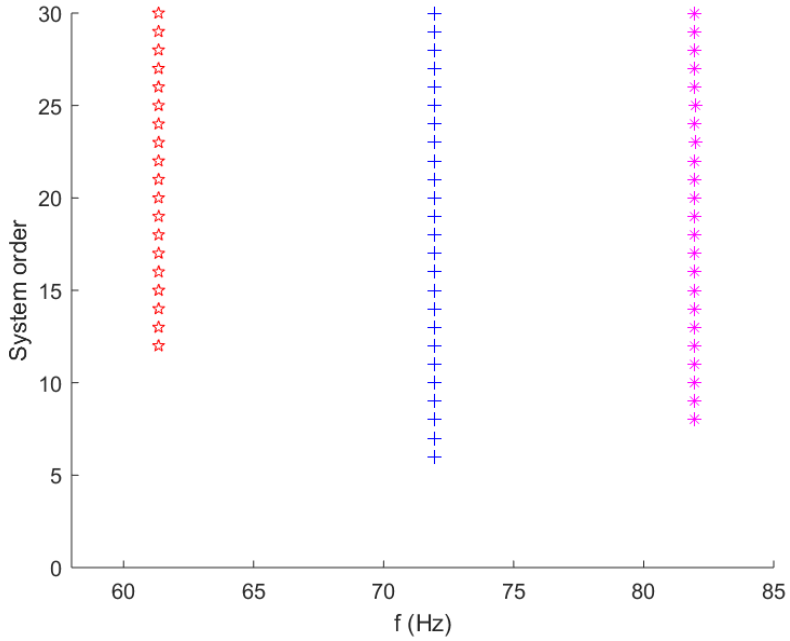


Figure B-8. The stable modes extracted from the stabilisation diagram estimated by SSI method.

In Figure B-9, the stablisation diagram estimated by P-LSCF method is presented, and the stable modes identified by removing the spurious ones are provided in Figure B-10.

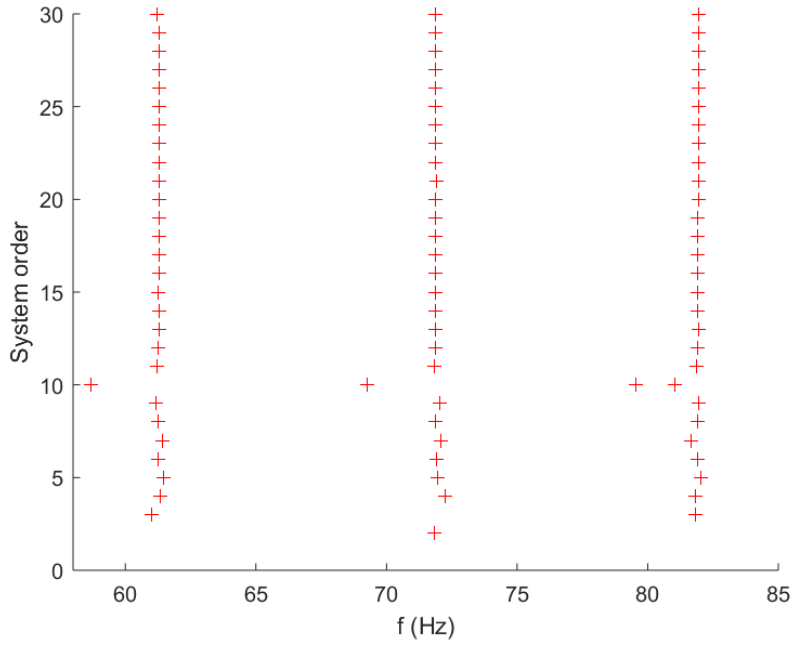


Figure B-9. The stabilisation diagram estimated by P-LSCF method.

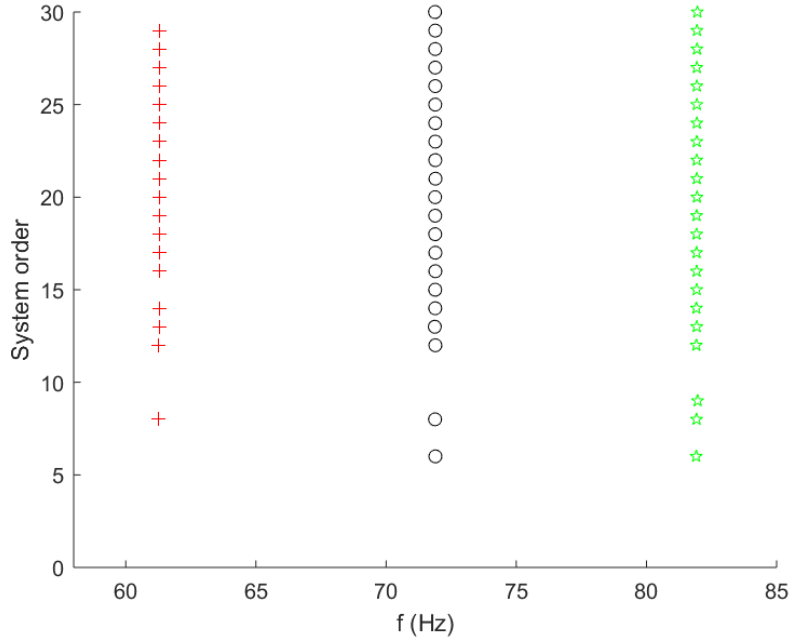


Figure B-10. The stable modes extracted from the stabilisation diagram estimated by P-LSCF method.

The frequency spectrum of the largest singular values estimated by FDD method for the selection of peaks in Bayesian method is provided in Figure B-11. The frequency results from SSI, P-LSCF and Bayesian methods are compared with those of FE model

from ABAQUS in table B-2 and the differences are presented in percentage.

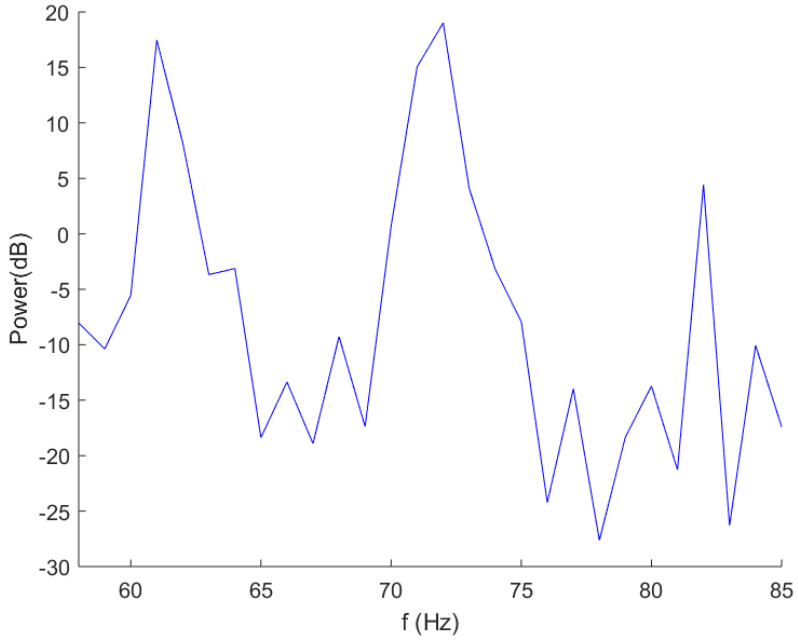


Figure B-11. The frequency spectrum of the largest singular values estimated by FDD method for the selection of peaks in Bayesian method.

Table B-2. The comparison of the frequency estimations from FE model in ABAQUS and each OMA method in MATLAB.

| Natural Frequency | f 1 | f 2 | f 3 |
|---|---|---|---|
| FE (Hz) | 62.178 | 73.265 | 84.108 |
| SSI (Hz) | 61.348 | 71.948 | 81.965 |
| Difference (%) | 1.335 | 1.798 | 2.548 |
| P-LSCF (Hz) | 61.292 | 71.887 | 81.943 |
| Difference (%) | 1.425 | 1.881 | 2.574 |
| Bayesian (Hz) | 61.342 | 71.869 | 81.898 |
| Difference (%) | 1.345 | 1.905 | 2.628 |

The MAC maps, which show the similarity of estimated mode shapes from each OMA method and those from FE model in ABAQUS, can be seen in Figure B-12. The

mode shape plots from FE model and OMA methods are provided in Figure B-13 for the verification of MAC maps. Therefore, from all the comparisons given in this chapter, it is verified that the OMA methods function correctly for the identification of result.

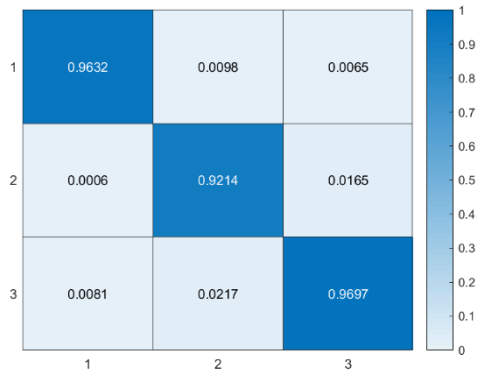


(a) SSI method.

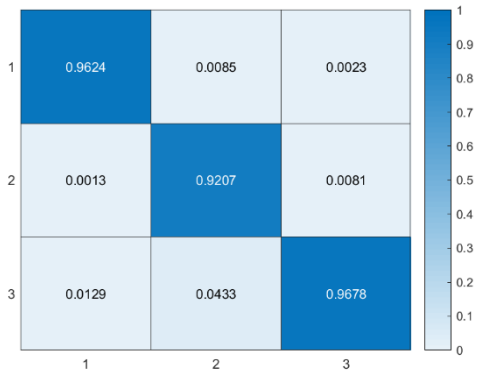


(b) P-LSCF method.

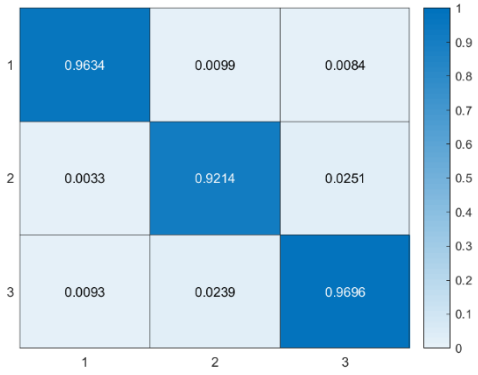


(c) Bayesian method.

Figure B-12. The MAC maps produced by each method. (x axis – mode shapes of each method, y axis – mode shapes of FE model)

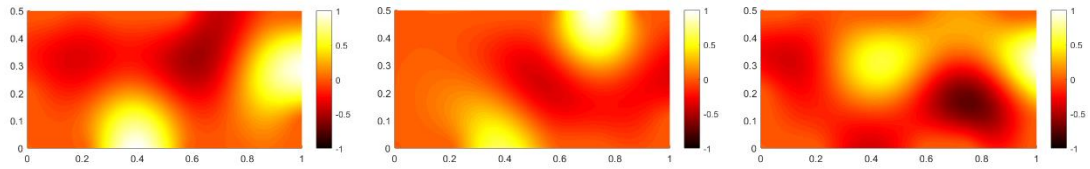

(a) 62.178 Hz (b) 73.265 Hz (c) 84.108 Hz

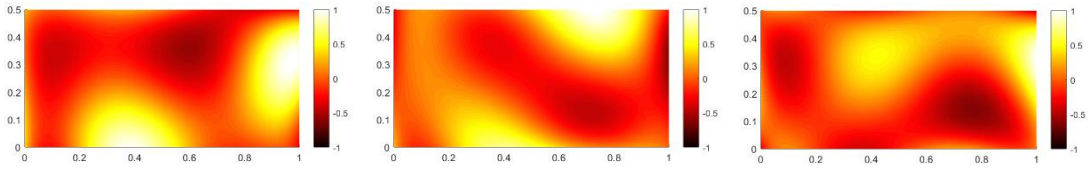

(d) 61.348 Hz (e) 71.948 Hz (f) 81.965 Hz

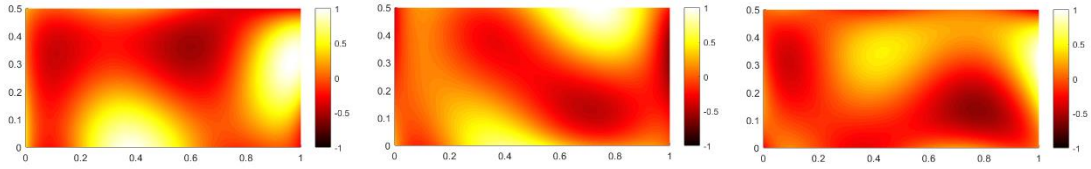

(g) 61.292 Hz (h) 71.887 Hz (i) 81.943 Hz

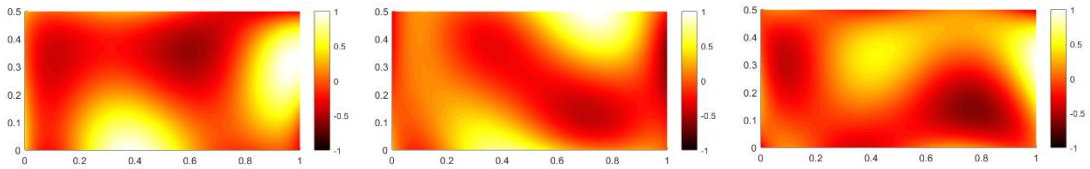

(j) 61.342 Hz (k) 71.869 Hz (l) 81.898 Hz

Figure B-13. The mode shapes displayed in MATLAB plot. (a)~(c): FE model. (d)~(f): SSI method. (g)~(i): P-LSCF method. (j)~(l): Bayesian method.

# C. Conference Paper C1

First page (please turn over) of

Y.-H. Chang, W. Wang, E.A. Patterson, J.-Y. Chang, J.E. Mottershead. “Output-only full-field modal testing,” X International Conference on Structural Dynamics. EURODYN. Procedia Engineering 199, pp. 423-428, 2017.

(Please turn over)

Available online at www.sciencedirect.com

ScienceDirect

Procedia Engineering 199 (2017) 423–428

Procedia Engineering

www.elsevier.com/locate/procedia

X International Conference on Structural Dynamics, EURODYN 2017

# Output-only full-field modal testing

Yen-Hao Chang[a,b], Weizhuo Wang[c], Eann A. Patterson[a], Jen-Yuan Chang[b], John E. Mottershead[a,d*]

[a] *Department of Mechanical, Aerospace and Materials Engineering, University of Liverpool, UK*
[b] *Department of Power Mechanical Engineering, National Tsing Hua University, Taiwan*
[c] *School of Engineering, Manchester Metropolitan University, UK*
[d] *Institute for Risk and Uncertainty, University of Liverpool, UK*

**Abstract**

Operational modal analysis has become the focus of much research attention in the last two decades. Instead of an artificial force, the ambient excitation is considered as white-noise input to the structure and modal properties are calculated only from measured responses. In terms of the measurement technique, full-field optical methods, for example: electronic speckle pattern interferometry and digital image correlation have become popular and there is now much interest in applying these methods in structural dynamics. In this case the generated data is a full displacement map of the object, therefore there is no necessity to select specific measurement locations in order to visualise the deformation. However, there are generally large volumes of data to be processed, which makes the computation expensive and time-consuming, especially for engineering structures with large surface areas. Thanks to image decomposition techniques, huge amounts of data can be compressed into tens of *shape descriptors* with acceptably small distortion. In this paper, operational modal analysis and full-field methods are combined together, and the analysis is done in the shape descriptor domain to reduce the required computation time. Simulated responses from a finite element model of a clamped plate (under random excitation) serve to illustrate the methodology. Several different operational modal analysis methods are applied to analyse the data, and results are provided for purposes of comparison.


Peer-review under responsibility of the organizing committee of EURODYN 2017.

*Keywords:* Operational modal analysis; Full-field measurement; Image decomposition.

* Corresponding author: John E. Mottershead, Department of Mechanical, Aerospace and Materials Engineering, University of Liverpool, Harrison-Hughes Building, The Quadrangle, Liverpool L69 3GH, UK.
E-mail address: j.e.mottershead@liv.ac.uk (J. E. Mottershead).

1877-7058 
Peer-review under responsibility of the organizing committee of EURODYN 2017.
10.1016/j.proeng.2017.09.137

# D. Journal Paper J1

First page (please turn over) of

Y.-H. Chang, W. Wang, T. Siebert, J.-Y. Chang, J. E. Mottershead. “Basis-updating for data compression of displacement maps from dynamic DIC measurements,” Mechanical Systems and Signal Processing 115, pp. 405–417, 2019.

(Please turn over)

Mechanical Systems and Signal Processing 115 (2019) 405–417

Contents lists available at ScienceDirect

Mechanical Systems and Signal Processing

journal homepage: www.elsevier.com/locate/ymssp

# Basis-updating for data compression of displacement maps from dynamic DIC measurements

Yen-Hao Chang [a,b], Weizhuo Wang [c], Thorsten Siebert [d], Jen-Yuan Chang [b], John E. Mottershead [a,*]

[a] Department of Mechanical, Aerospace and Materials Engineering, University of Liverpool, UK
[b] Department of Power Mechanical Engineering, National Tsing Hua University, Taiwan
[c] School of Engineering, Manchester Metropolitan University, UK
[d] Dantec Dynamics GmbH, Kaessbohrer Str. 18, D 89077 Ulm, Germany

ARTICLE INFO

*Article history:*
Received 22 March 2018
Received in revised form 16 May 2018
Accepted 28 May 2018
Available online 13 June 2018

*Keywords:*
Shape descriptor
Dictionary updating
K-SVD
Sparse representation
Kernel function
Operational modal analysis

ABSTRACT

The extraction of useful information and removal of redundant noise from data has become a major research topic in recent years. Data compression is necessary for all kinds of analysis, and the demand for efficient compression techniques has gained much attention. Digital image correlation is a camera-based measuring system, which has been widely applied in strain analysis because of the convenience of measuring displacement fields by simply selecting a region of interest. Currently, there is interest in applying such methods to engineering structures in dynamics. However, one of the major issues related to the integration of camera-based systems with dynamic measurement is the generation of huge amounts of data, typically extending to many thousands of data points, because of the requirements of high sampling rate, spatial resolution, and long duration of recording. In this paper a new algorithm is presented that addresses the need for efficiency in full-field data processing. By making use of the data itself and combining the concept of sparse representation with Gram-Schmidt orthogonalisation, the number of basis function used to represent the data can be reduced and a concise decomposition established. In both simulated and experimental cases, the compression ratios for data size and number of signals used in operational modal analysis are substantially diminished, thereby demonstrating the effectiveness of the proposed algorithm. A reduced number of new basis functions is determined for the representation of data under the condition that the reconstructed displacement map reproduces the raw measured data to within a chosen threshold on the coefficient of correlation.



## 1. Introduction

With the ever-growing size of data, the problems of processing and storage have greatly increased to such an extent that data cannot be processed by personal computers with limited computational capacities directly. The extraction of useful information and removal of redundant data has become a major research topic in recent years. Data compression is now seen to be a necessity for analysis, and the demand for efficient compression techniques has gained the attention of numerous

* Corresponding author at: Department of Mechanical, Aerospace and Materials Engineering, University of Liverpool, Harrison-Hughes Building, The Quadrangle, Liverpool L69 3GH, UK.
*E-mail address:* j.e.mottershead@liv.ac.uk (J.E. Mottershead).

https://doi.org/10.1016/j.ymssp.2018.05.058
0888-3270/

# E. Journal Paper J2

First page (please turn over) of

Y.-H. Chang, W. Wang, J.-Y. Chang, J. E. Mottershead. “Compressed sensing for OMA using full-field vibration images,” Mechanical Systems and Signal Processing 129, pp. 394-406, 2019.

(Please turn over)

Mechanical Systems and Signal Processing 129 (2019) 394–406

Contents lists available at ScienceDirect

Mechanical Systems and Signal Processing

journal homepage: www.elsevier.com/locate/ymssp

# Compressed sensing for OMA using full-field vibration images

Yen-Hao Chang [a,b], Weizhuo Wang [c], Jen-Yuan Chang [b], John E Mottershead [a,*]

[a] Department of Mechanical, Aerospace and Materials Engineering, University of Liverpool, UK
[b] Department of Power Mechanical Engineering, National Tsing Hua University, Taiwan
[c] School of Engineering, Manchester Metropolitan University, UK

ARTICLE INFO

*Article history:*
Received 21 January 2019
Received in revised form 4 April 2019
Accepted 16 April 2019
Available online 28 April 2019

*Keywords:*
Compressed sensing
Shape descriptor
Sparse representation
Structural health monitoring
Operational modal analysis

ABSTRACT

Optically-acquired data, typically from digital image correlation, is increasingly being used in the area of structural dynamics, particularly modal testing and damage identification. One of the problems with such data is its extremely large size. Single images regularly extend to tens or even hundreds of thousands of data points and many thousands of images may be required for a vibration test. Such data must be stored and transmitted efficiently for later remote reconstruction and analysis, typically operational modal analysis. It is this requirement that is addressed in the research presented in this paper. This research builds upon previous work whereby digitised optical data was projected onto an orthogonal basis with coefficients (shape descriptors) of either greater or lesser significance; those deemed to be insignificant, according to a chosen threshold being removed. Data reduction by a combination of shape-descriptor decomposition and compressed-sensing is applied to an industrial printed circuit board and reconstructed for operational modal analysis by $\ell_1$ optimisation.



## 1. Introduction.

In recent years the demand for online monitoring and remote inspection has brought about a huge surge of research activity in structural health monitoring (SHM). Applications range from the preservation of historical buildings [1] to the monitoring and maintenance of offshore wind turbines [2] with the purpose of minimising the costs of restoration, deterioration, machine down-time etc. Wireless sensor networks are increasingly prevalent. Hierarchical decentralized SHM as presented by Hackmann et al. [3] was said to be capable of only activating sensors in damaged regions and keeping others idle. Other than conventional accelerometer or strain gauge measurement, non-destructive acoustic [4] and non-contact vision-based [5,6] measuring methods are also being adopted. Yang et al. [7] proposed a high-fidelity simulation and visualisation method for full-field dynamic structural responses based on phase-based motion magnification (Wadhwa et al. [8]) as an alternative to finite element analysis. Along with the expanding application of video-based monitoring, image transmission or storage plays an important role in realising the implementation of state-of-art techniques in industry. Yang and Nagarajaiah [9] suggested that images gathered from measurement can be first compressed for transmission and afterwards recovered by using the compressed sensing (CS) technique developed by Donoho [10]. As explained in [9], the main factor in industrial adoption of SHM research is the efficient and reliable transfer and processing of data. A discussion on closing the

* Corresponding author.
*E-mail address:* j.e.mottershead@liverpool.ac.uk (J.E Mottershead).

https://doi.org/10.1016/j.ymssp.2019.04.031
0888-3270/

# Reference


[1] F. Ubertini, G. Comanducci, N. Cavalagli. “Vibration-based structural health monitoring of a historic belltower using output-only measurements and multivariate statistical analysis,” Structural Health Monitoring 15 (4), pp. 438–457, 2016.

[2] W. Weijtjens, T. Verbelen, G. De Sitter, C. Devriendt. “Foundation structural health monitoring of an offshore wind turbine—A full-scale case study,” Struct. Heal. Monit., 15, 389–402, 2015.

[3] G. Hackmann, W. Guo, G. Yan, Z. Sun, C. Lu, S. Dyke. “Cyber-physical codesign of distributed structural health monitoring with wireless sensor networks,” IEEE Trans. Parallel Distrib. Syst. 25 (1), pp. 63–72, 2014.

[4] M. Y. Bhuiyan, J. Bao, B. Poddar, V. Giurgiutiu. “Toward identifying crack-length-related resonances in acoustic emission waveforms for structural health monitoring applications.” Structural Health Monitoring, 2017.

[5] D. Feng, M. Q. Feng. “Experimental validation of cost-effective vision-based structural health monitoring.” Mechanical Systems and Signal Processing, 88, pp. 199-211, 2017.

[6] T. Khuc, F. N. Catbas, “Completely contactless structural health monitoring of real-life structures using cameras and computer vision,” Struct. Control Heal. Monit., 2016.

[7] Y. Yang, C. Dorn, T. Mancini, Z. Talken, G. Kenyon, C. Farrar, D. Mascareñas. “Spatiotemporal video-domain high-fidelity simulation and realistic visualization of full-field dynamic responses of structures by a combination of high-spatial-resolution modal model and video motion manipulations,” Struct Control Health

Monit., 2018.

[8] N. Wadhwa, M. Rubinstein, F. Durand, W. T. Freeman. “Phase-based video motion processing.” ACM Transactions on Graphics 32, 4, 80, 2013.

[9] Y. Yang, S. Nagarajaiah. “Robust data transmission and recovery of images by compressed sensing for structural health diagnosis,” Structural Control and Health Monitoring, 2016.

[10] D. Donoho. “Compressed sensing,” IEEE Trans. Inform. Theory 52 (4), pp.1289–1306, 2016.

[11] P. Cawley. “Structural health monitoring: Closing the gap between research and industrial deploymen,”. Int. J. Struct. Health Monit., 2018.

[12] J. P. Amezquita-Sanchez, H. Adeli. “Signal Processing Techniques for Vibration-Based Health Monitoring of Smart Structures,” Archives of Computational Methods in Engineering, pp. 1–15, 2014.

[13] W. H. Peters, W. F. Ranson. “Digital imaging techniques in experimental stress analysis.” Optical Engineering 21(3), pp. 427-431, 1982.

[14] M. A. Sutton, W. J. Wolters, W. H. Peters, W. F. Ranson, S. R. McNeill. “Determination of displacements using an improved digital correlation method,” Image and Vision Computing, Volume 1, Issue 3, pp. 133-139, 1983.

[15] W. H. Peters, W. F. Ranson, M. A. Sutton, T. C. Chu, J. Anderson. “Applications of Digital Correlation Methods to Rigid Body Mechanics,” Opt. Eng., 22 (6), 1983.

[16] H. Bruck, S. McNeill, M. Sutton, W. Peters. “Digital image correlation using Newton-Raphson method of partial differential correction,” Exp. Mech., 29, pp. 261–267, 1989.

[17] M. A. Sutton, J. Orteu, H. W. Schreier. “Image correlation for shape, motion and deformation measurements: basic concepts, theory and applications,” Springer, 2009.

[18] W. N. Sharpe. “Handbook of experimental solid mechanics,” Springer, chap. 18-20, 2008.

[19] T. J. Beberniss, D. A. Ehrhardt. “High-speed 3D digital image correlation vibration measurement: Recent advancements and noted limitations,” Mechanical Systems and Signal Processing, 86, pp. 35-48, 2017.

[20] P. Poozesh, A. Sarrafi, Z. Mao, P. Avitabile, C. Niezrecki. “Feasibility of extracting operating shapes using phase-based motion magnification technique and stereo-photogrammetry,” Journal of Sound and Vibration, 407, pp. 350-366, 2017.

[21] A.J. Molina-Viedma, L. Felipe-Sesé, E. López-Alba, F.A. Díaz. “3D shapes characterization using phase-based motion magnification in large structures using stereoscopic DIC,” Mechanical Systems and Signal Processing, 108, pp. 140-155, 2018.

[22] A.J. Molina-Viedma, L. Felipe-Sesé, E. López-Alba, F.A. Díaz. “High frequency mode shapes characterization using Digital Image Correlation and phase-based motion magnification,” Mechanical Systems and Signal Processing, 102, pp. 245-261, 2018.

[23] P. Poozesh, J. Baqersad, C. Niezrecki, P. Avitabile, E. Harvey, R. Yarala. “Large-area photogrammetry based testing of wind turbine blades.” Mechanical Systems and Signal Processing, 86, pp. 98-115, 2017.

[24] K. Patil, V. Srivastava, J. Baqersad. “A multi-view optical technique to obtain mode shapes of structures.” Measurement, 122, pp. 358-367, 2018.

[25] J. Javh, J. Slavič, M. Boltežar. “The subpixel resolution of optical-flow-based modal analysis,” Mechanical Systems and Signal Processing, 88, pp. 89-99, 2017.

[26] L. Yu, B. Pan. “Color Stereo-Digital Image Correlation Method Using a Single 3CCD Color Camera,” Experimental Mechanics, 51 (4), pp. 649–657, 2017.

[27] L. Yu, B. Pan. “Single-camera high-speed stereo-digital image correlation for full-

field vibration measurement," Mechanical Systems and Signal Processing 94, pp. 374-383, 2017.

[28] L. Yu, B. Pan. "Full-frame, high-speed 3D shape and deformation measurements using stereo-digital image correlation and a single color high-speed camera," Optics and Lasers in Engineering 95, pp. 17-25, 2017

[29] Y. Chi, L. Yu, B. Pan. "Low-cost, portable, robust and high-resolution single-camera stereo-DIC system and its application in hightemperature deformation measurements," Optics and Lasers in Engineering. 104, pp.141-148, 2018.

[30] B. Pan, L. Yu, Q. B. Zhang. "Review of single-camera stereo-digital image correlation techniques for full-field 3D shape and deformation measurement," Sci China Technol Sci, 2017.

[31] P. J. Sousa, F. Barros, P. J. Tavares, P. M. G. Moreira. "Displacement measurement and shape acquisition of an RC helicopter blade using digital image correlation," Procedia Structural Integrity, 5, pp. 1253-1259, 2017.

[32] R. Perez, G. Bartram, T. Berniss, R. Wiebe, S. M. Spottswood. "Calibration of aero-structural reduced order models using full-field experimental measurements," Mechanical Systems and Signal Processing, 86, pp. 49-65, 2017.

[33] M. Flores, D. Mollenhauer, V. Runatunga, T. Beberniss, D. Rapling, M. Pankow. "High-speed 3D digital image correlation of low-velocity impacts on composite plates," Composites Part B, 131, pp. 153-164, 2017.

[34] F. Hild, S. Roux. "Comparison of local and global approaches to digital image correlation," Exp. Mech. 52, 1503–1519, 2012.

[35] D. Wang, F. A. DiazDelaO, W. Wang, J. E. Mottershead. "Full-field digital image correlation with Kriging regression," Optics and Lasers in Engineering, 67, pp. 105–115, 2015.

[36] D. Wang, F. A. DiazDelaO, W. Wang, X. Lin, E. A. Patterson, J. E. Mottershead.

"Uncertainty quantification in DIC with kriging regression," Optics and Lasers in Engineering, 78, pp. 182 – 195, 2016.

[37] Y. L. Dong, B. Pan. "A Review of Speckle Pattern Fabrication and Assessment for Digital Image Correlation," Exp. Mech., 57, pp. 1161–1181, 2017.

[38] B. Pan, B. Wang. "A flexible and accurate digital volume correlation method applicable to high-resolution volumetric images," Meas. Sci. Technol. 28, 105007, 2017.

[39] B. Wang, B. Pan. "Incremental digital volume correlation method with nearest subvolume offset: an accurate and simple approach for large deformation measurement," Adv. Eng. Software, 116, pp. 80-88, 2018.

[40] B. Pan. "Thermal error analysis and compensation for digital image/volume correlation," Opt. Lasers Eng., 101, pp. 1–15, 2018.

[41] A. Buljac, C. Jailin, A. Mendoza, J. Neggers, T. Taillandier-Thomas, A. Bouterf, B. Smaniotto, F. Hild, and S. Roux. "Digital volume correlation: Review of progress and challenges," Experimental Mechanics, 58(5), pp. 661–708, 2018.

[42] B. Peeters, G. De Roeck. "Referenced-based stochastic subspace identification for output-only modal analysis," Mechanical Systems and Signal Processing 13(6), pp. 855-878, 1999.

[43] S. R. Ibrahim. "Random decrement technique for modal identification of structures," The AIAA Journal of Spacecraft and Rockets. 14(11), 1977.

[44] S. R. Ibrahim, E. C. Mikulcik. "A method for direct identification of vibration parameters from the free response," The Shock and Vibration Bulletin. 47(4), pp. 183–98, 1977.

[45] D. M. Siringoringo, Y. Fujino. "System identification of suspension bridge from ambient vibration response," Eng. Struct. 30 (2), pp. 462–477, 2008.

[46] F. Poncelet, G. Kerschen, J.-C. Golinval, D. Verhelst. "Output-only modal analysis

using blind source separation techniques," Mechanical Systems and Signal Processing, Volume 21, pp. 2335-2358, 2007.

[47] E. Reynders, J. Houbrechts, G. De Roeck. "Fully automated (operational) modal analysis," Mech Syst. Signal Process 29, pp.228–250, 2012.

[48] R. Brincker, P. Andersen, N.-J. Jacobsen. "Automated frequency domain decomposition for operational modal analysis," In Proceedings of the 25th International Modal Analysis Conference, Orlando, FL, February 2007.

[49] R. Brincker, L. Zhang, P. Andersen. "Modal identification from ambient responses using frequency domain decomposition," Proceedings of the IMAC 18, International Modal Analysis Conference, pp. 625-630, 2000.

[50] C. Devriendt, P. Guillaume. "The use of transmissibility measurements in output-only modal analysis," Mechanical Systems and Signal Processing 21 (7), pp. 2689–2696, 2007.

[51] W. J. Yan, W. X. Ren. "An enhanced power spectral density transmissibility (EPSDT) approach for operational modal analysis: theoretical and experimental investigation," Eng. Struct. 102, pp. 108–119, 2015.

[52] B. Peeters, H. Van Der Auweraer. "PolyMax: a revolution in operational modal analysis," Proceedings of the IOMAC, International Operational Modal Analysis Conference, Copenhagen, Denmark, 2005.

[53] S. K. Au. "Fast Bayesian FFT Method for Ambient Modal Identification with Separated Modes," J. Eng. Mech., 137(3), pp. 214-226, 2011.

[54] S. K. Au. "Fast Bayesian ambient modal identification in the frequency domain, Part I: Posterior most probable value," Mechanical Systems and Signal Processing, 26, pp. 60-75, 2012a.

[55] S. K. Au. "Fast Bayesian ambient modal identification in the frequency domain, Part II: Posterior uncertainty," Mechanical Systems and Signal Processing, 26, pp.

76-90, 2012b.

[56] G. Oliveira, F. Magalhaes, A. Cunha, E. Caetano. “Continuous dynamic monitoring of an onshore wind turbine,” Engineering Structures, 164, pp. 22-39, 2018.

[57] G.-W. Chen, P. Omenzetter, S. Beskhyroun. “Operational modal analysis of an eleven-span concrete bridge subjected to weak ambient excitations,” Engineering Structures, 151, pp. 839-860, 2017..

[58] A. De Vivo, C. Brutti, J. L. Leofanti. “Modal shape identification of large structures exposed to wing excitation by operational modal analysis technique,” Mechanical Systems and Signal Processing, 39, pp. 195-206, 2013.

[59] B. Chomette, J. L. Carrou. “Operational modal analysis applied to the concert harp,” Mechanical Systems and Signal Processing, 56-57, pp. 81-91, 2015.

[60] E. Reynders, K. Mayes, G. Lombaert, G. De Roeck. “Uncertainty quantification in operational modal analysis with stochastic subspace identification: validation and applications,” Mechanical Systems and Signal Processing, 66-67, pp. 13-30, 2016.

[61] Y.-C. Zhu, S.-K. Au. “Bayesian operational modal analysis with asynchronous data, part I: most probable value,” Mechanical Systems and Signal Processing, 98, pp. 652-666, 2018.

[62] Y.-C. Zhu, S.-K. Au. “Bayesian operational modal analysis with asynchronous data, part II: posterior uncertainty,” Mechanical Systems and Signal Processing, 98, pp. 920-935, 2018.

[63] Y.-C. Zhu, Y-L. Xie, S.-K. Au. “Bayesian operational modal analysis with asynchronous data, part 1: most probable value,” Engineering Structures, 165, pp. 50-62, 2018.

[64] S. Rizo-Patron, J. Sirohi. “Operational Modal Analysis of a Helicopter Rotor

Blade Using Digital Image Correlation," Experimental Mechcanics, 57, pp. 367-375, 2017.

[65] Y.-H. Chang, W. Wang, E. A. Patterson, J.-Y. Chang, and J. E. Mottershead. "Output-only full-field modal testing," X International Conference on Structural Dynamics, EURODYN. Procedia Engineering 199, pp. 423–428, 2017.

[66] H. Leclerc, J.-N. Périé, S. Roux, F. Hild. "Integrated digital image correlation for the identification of mechanical properties," Computer Vision/Computer Graphics Collaboration Techniques 5496, pp. 161–171, 2009.

[67] W. Wang, J. E. Mottershead, C. Mares. "Vibration mode shape recognition using image processing," Journal of Sound and Vibration 326 (3–5), pp. 909–938, 2009a.

[68] W. Wang, J. E. Mottershead, C. Mares. "Mode-shape recognition and finite element model updating using the Zernike moment descriptor," Mechanical Systems and Signal Processing 23 (7), pp. 2088–2112, 2009b..

[69] W. Wang, J. E. Mottershead, A. Ihle, T. Siebert, H. R. Schubach. "Finite element model updating from full-field vibration measurement using digital image correlation," Journal of Sound and Vibration 330 (8), pp. 1599–1620, 2011a..

[70] W. Wang, J. E. Mottershead, C. M. Sebastian, E. A. Patterson. "Shape features and finite element model updating from full-field strain data," Int. J. Solids Struct. 48 (11–12), pp. 1644–1657, 2011b..

[71] W. Wang, J. E. Mottershead, C. M. Sebastian. "Image analysis for full-field displacement/strain data: methods and applications," Appl Mech Mater, 70, pp. 39–44, 2011c.

[72] A. S. Patki, E. A. Patterson. "Decomposing strain maps using Fourier-Zernike shape descriptors," Exp. Mech., 52(8), pp. 1137-1149, 2012.

[73] M. K. Hu. "Visual pattern recognition by moment invariants," IRE Transactions on Information Theory IT-8, pp. 179–187, 1962.

[74] F. Zernike. “Beugungstheorie des Schneidenverfahrens und Seiner Verbesserten Form, der Phasenkontrastmethode,” Physica 1, 1934.

[75] R. Mukundan, S. H. Ong, P. A. Lee. “Image analysis by Tchebichef moments,” IEEE Transactions on Image Processing: A Publication of the IEEE Signal Processing Society 10 (9), pp. 1357–1364, 2001.

[76] P. T. Yap, R. Paramesran, S. H. Ong. “Image analysis by Krawtchouk moments,” IEEE Transactions on Image Processing 12(11), pp. 1367–1377, 2003.

[77] I. Daubechies. “Ten Lectures on Wavelets”, Society for Industrial and Applied Mathematics, 1992..

[78] W. Wang, J. E. Mottershead, T. Siebert, A. Pipino. “Frequency response functions of shape features from full-field vibration measurements using digital image correlation,” Mech. Sys. Sig. Proc., 28, pp. 333-347, 2012.

[79] M. Desbrun, M. Meyer, P. Alliez. “Intrinsic parameterizations of surface meshes,” Comput. Graph. Forum 21 (3), pp. 209–218, 2002.

[80] U. Pinkall, K. Polthier. “Computing discrete minimal surfaces and their conjugates,” Exp. Math. 2 (1), pp. 15–36, 1993.

[81] W. Wang, D. Wang, J. E. Mottershead, G. Lampeas, “Identification of Composite Delamination Using the Krawtchouk Moment Descriptor,” Key Engineering Materials, Vols. 569-570, pp. 33-40, 2013.

[82] R. L. Burguete, G. Lampeas, J. E. Mottershead, E. A. Patterson, A. Pipino, T. Siebert, W. Wang. “Analysis of displacement fields from a high speed impact using shape descriptors,” J. Strain Analysis, 49(4), pp. 212-223, 2014.

[83] E. Candès, J. Romberg, T. Tao. “Robust uncertainty principles: Exact signal reconstruction from highly incomplete frequency information,” IEEE Trans. Inform. Theory, vol. 52, no. 2, pp. 489–509, Feb. 2006.

[84] M. Lustig, D. L. Donoho, J. M. Santos, J. M. Pauly. “Compressed sensing MRI,”

IEEE Signal Process. Mag., 25, pp. 72–82, 2008.

[85] J. W. Sanders, H. Song, S. J. Frank, T. Bathala, A. M. Venkatesan, M.Anscher, C. Tang, T. L. Bruno, W. Wei, J. Ma. “Parallel imaging compressed sensing for accelerated imaging and improved signal-to-noise ratio in MRI-based postimplant dosimetry of prostate brachytherapy,” American Brachytherapy Society, 2018.

[86] J. H. Yoon, S. M. Lee, H.-J. Kang, E. Weiland, E. Raithel, Y. Son, B. Kiefer, J. M. Lee. “Clinical feasibility of 3-dimensional magnetic resonance cholangiopancreatography using compressed sensing: comparison of image quality and diagnostic performance,” Invest Radiol., 52, pp. 612–619, 2017.

[87] Z. Lai, X. Qu, Y. Liu, D. Guo, J. Ye, Z. Zhan, Z. Chen. “Image reconstruction of compressed sensing MRI using graph-based redundant wavelet transform,” Medical Image Analysis 27, pp. 93-104, 2016.

[88] S. Arridge, P. Beard, M. Betcke, B. Cox, N. Huynh, F. Lucka, O. Ogunlade, E. Zhang. “Accelerated high-resolution photoacoustic tomography via compressed sensing,” Phys. Med. Biol. 61, pp. 8908-8940, 2016.

[89] D. Gangopadhyay, E. G. Allstot, A. M. R. Dixon, K. Natarajan, S. Gupta, D. J. Allstot. “Compressed Sensing Analog Front-End for Bio-Sensor Applications,” IEEE journal of solid-state circuits, vol. 49. No. 2, pp. 426-438, 2014.

[90] D. Craven, B. McGinley, L. Kilmartin, M. Glavin, E. Jones. “Compressed sensing for bioelectric signals: a review,” Biomedical and Health Informatics, IEEE Journal of, vol. 19, no. 2, pp. 529–540, 2015.

[91] S. Felix, R. Bolzern, M. Battaglia. “A compressed sensing-based image reconstruction algorithm for solar flare x-ray observations,” The Astrophysical Journal, 849, 10, 2017.

[92] C. S. Oxvig, T. Arildsen, T. Larsen. “Structure assisted compressed sensing reconstruction of undersampled AFM images,” Ultramicroscopy, vol. 172, pp. 1–

9, Jan. 2017.

[93] J. P. Dumas, M. A. Lodhi, W. U. Bajwa, M. C. P. Rutgers. “A compressed sensing approach for resolution improvement in fiber-bundle based endomicroscopy,” Endoscopic Microscopy, 2018.

[94] F. Ning, F. Pan, C. Zhang, Y. Liu, X. Li, J. Wei. “A highly efficient compressed sensing algorithm for acoutstic imaging in low signal-to-noise ratio environments,” MSSP, 112, pp. 113-128, 2018.

[95] X. Yuan, R. Haimi-Cohen. “Image Compression Based on Compressive Sensing, End-to-End Comparison with JPEG,” 2017.

[96] L. C. Potter, E. Ertin, J. T. Parker, M. Cetin. “Sparsity and compressed sensing in radar imaging,” Proc. IEEE 98(6), pp. 1006–1020, 2010.

[97] Y. Yang, S. Nagarajaiah. “Output-only modal identification by compressed sensing: Non-uniform low-rate random sampling.” MSSP 56-57, pp. 15-34, 2015.

[98] S. Qin, J. Guo, C Zhu. “Sparse component analysis using time-frequency representations for operational modal analysis,” Sensors, 15, pp. 6497-6519, 2015.

[99] J.Y. Park, M.B. Wakin, A.C. Gilbert. “Modal analysis with compressive measurement,” IEEE Transactions on Signal Processing, 62(7), pp. 1655-1670, 2014.

[100] M. Rani, S. Dhok, R. Deshmukh. ‘‘A systematic review of compressive sensing: Concepts, implementations and applications,’’ IEEE Access, vol. 6, pp. 4875–4894, 2018.

[101] E. J. Candes, M. B. Wakin. “An introduction to compressive sampling,” IEEE Signal Proc. Mag., vol. 25, no. 2, pp. 21–30, Mar. 2008.

[102] Y. Niu, H. Wang, S. B. Park. “A general strategy of in-situ warpage characterization for solder attached packages with digital image correlation method,” Optics and Lasers in Engineering, Volume 93, pp. 9-18, 2017.

[103] A. W. Mello, A. Nicolas, M. D. Sangid. “Fatigue strain mapping via digital image correlation for Ni-based superalloys: the role of thermal activation on cube slip,” Materials Science & Engineering. Volume 695, pp. 332-341, 2017.

[104] R. Huňady, M. Hagara. “A new procedure of modal parameter estimation for high-speed digital image correlation,” Volume 93, pp. 66-79, 2017.

[105] P. Cheng, M. Sutton, H. Schreier, S. McNeill. “Full-field speckle pattern image correlation with B-Spline deformation function,” Experimental Mechanics, 42, pp. 344-352, 2002.

[106] Y. Sun, J. H. L. Pang, C. K. Wong, F. Su. “Finite element formulation for a digital image correlation method,” Applied Optics, 44, pp. 7357-7363, 2005.

[107] F. Magalhães, A. Cunha. “Explaining operational modal analysis with data from an arch bridge,” Mech. Syst. Signal Process. 25 (5), pp. 1431–1450, 2011.

[108] J.-N. Juang. “Applied System Identification,” Prentice Hall, Englewood Cliffs, NJ, USA, 1994.

[109] B. Shen, W. Hu, Y. Zhang, Y. Zhang. “Image inpainting via sparse representation,” in Proc. IEEE Int. Conf. Acoustics, Speech and Signal Processing, pp. 697–700, 2009.

[110] J. Yang, J. Wright, T. S. Huang, Y. Ma. “Image super-resolution via sparse representation,” TIP 19(11), pp. 2861–2873, 2010.

[111] M. Elad, M. Aharon. “Image denoising via sparse and redundant representations over learned dictionaries,” IEEE Transaction on Image Processing, 2006.

[112] M. Aharon, M. Elad, A. M. Bruckstein. “The K-SVD: an algorithm for designing of overcomplete dictionaries for sparse representation,” IEEE Transactions on Signal Processing 54, pp. 4311–4322, 2006.

[113] Y.-H. Chang, W. Wang, T. Siebert, J.-Y. Chang, J. E. Mottershead. “Basis-updating for data compression of displacement maps from dynamic DIC measurements,”

Mechanical Systems and Signal Processing 115, pp. 405–417, 2019.

[114] E. Candès, J. Romberg. "ℓ1 -MAGIC: Recovery of sparse signals via convex programming," California Inst. Technol., Pasadena, CA, Tech. Rep., Oct. 2005.

[115] W. Cheney, D. R. Kincaid. "Linear algebra: Theory and applications." pp. 544–550, 2009.